Eindhoven University of Technology

MASTER

Optical emission spectroscopy of an atmospheric pressure helium plasma jet

de Peuter, Marco C.

Award date:
2020

Link to publication

Disclaimer
This document contains a student thesis (bachelor's or master's), as authored by a student at Eindhoven University of Technology. Student theses are made available in the TU/e repository upon obtaining the required degree. The grade received is not published on the document as presented in the repository. The required complexity or quality of research of student theses may vary by program, and the required minimum study period may vary in duration.

General rights
Copyright and moral rights for the publications made accessible in the public portal are retained by the authors and/or other copyright owners and it is a condition of accessing publications that users recognise and abide by the legal requirements associated with these rights.

- Users may download and print one copy of any publication from the public portal for the purpose of private study or research.
- You may not further distribute the material or use it for any profit-making activity or commercial gain

Eindhoven University of Technology
Department of Applied Physics
Elementary Processes in Gas Discharges (EPG)

Master Thesis

Optical emission spectroscopy of an atmospheric pressure helium plasma jet

Author:
M.C. de Peuter

Supervisors:
dr. Dipl.-Ing. A. Sobota (TU/e)
dr.ir. W.F.L.M. Hoeben (TU/e)

2020

Abstract

Over the last decades, cold atmospheric pressure plasma jets have widely attracted interest for a possible usage in biomedical applications. One of the prerequisites for the viability of plasmas in biomedical applications is that the ionized jet gas temperature should be near room temperature and carry a low current while attaining high plasma stability and maintaining efficient reaction chemistry.

In this thesis a non-thermal atmospheric pressure helium plasma jet in air has been studied using optical emission spectroscopy (OES), a non-intrusive diagnostic method. The plasma is generated by applying a 30 kHz sinusoidal high voltage of 3.25 kV to 4.00 kV (peak-to-peak) to the helium feed gas, at volumetric flow rates of 600 sccm to 1200 sccm.

To conduct the OES measurements, firstly a spectrograph setup is constructed and calibrated. The experiments were executed in the High Voltage Laboratory of the Eindhoven University of Technology, an electromagnetic hazardous environment that can interfere with the equipment, which as a consequence could influence the measurements. To prevent EM interference, shielding is designed which allowed to control and acquire measurement data from the setup.

The influence of the plasma operating parameters on the population of the excited species in the plasma jet effluent are investigated. Emission intensities of the ionized gas plume are measured outside the plasma device, up to the first 10.5 mm in front of the capillary exit. The following excited species were identified in the plasma plume: the $OH(A^2\Sigma_+)$ radical at 309 nm, the $N_2(C^3\Pi_u)$ molecule at 337 nm, the N_2^+ at 391 nm ion, the atomic helium $He(3s^3S_1)$ at 706 nm and atomic oxygen $O(3p^5P_3)$ at 777 nm.

The results of the OES measurements are presented in two ways: emission intensity trends for each species along the plume and as intensity ratios relatively to He I emission. The atomic oxygen emission is observed to be the only one for which the intensity is reduced downstream of the helium plasma plume compared to the helium emission, despite the increase of air admixture along the helium channel.

Contents

Glossary of terms

For convenience here is a list of the abbreviations that are used the most in this work.

APPJs	Atmospheric pressure plasmas jets
DBD	Dielectric barrier discharge
EMC	Electromagnetic compatibility
FNS	First negative system
FWHM	Full width at half maximum
ICCD	Intensified charge-coupled device
MCP	Multi channel plate
OES	Optical emission spectroscopy
SPS	Second positive system

The figures in this work are adapted or created, inspired by the reference reported in the section.

Chapter 1

Preface

1.1 Plasma

The term *plasma* was used for the first time by Langmuir and Tonks in 1928 to describe the inner region in a quasi-neutral gas [1]. Plasmas are (partly) ionised gases and are a cocktail of photons, neutral, reactive and charged species, which exhibit a collective behaviour due to the coulomb forces. Plasmas are often called the fourth state of matter, next to solid, liquid and gaseous, although it does not include the same distinct phase transition like in the other aforementioned states, since the transition from a gas to a plasma occurs gradually with increasing thermal energy.

During the last century it was realized that most of the visible matter in the known universe exists as a plasma; our nearest star, the sun, is a plasma phenomenon. Known examples of naturally occurring plasmas on earth are lightning and the auroras near the poles. Nowadays, a wide variety of man-made plasmas are also present all around us. The progress in plasma research led to a wide range of plasma applications and in almost every industry there are plasma assisted production steps. For example, in manufacturing integrated circuits used by the electronics industry or in trying to accomplishing energy generation by thermonuclear fusion.

There are many methods of generating plasmas, and depending on the method, the plasma will be stable, will have a low or high temperature, will have variations in degree of ionization and so on [2]. A common process to create a plasma is an electric discharge in gases, according to the Townsend breakdown mechanism. An electric field is applied across an (ionized) gas which will accelerate the present free electrons to high enough energy to ionize other atoms by collision, which will create an avalanche. When the external field is applied for a sufficiently long time the electron avalanche will reach the anode, resulting in a breakdown of the gas. This breakdown will be accelerated by secondary electron emission at the cathode surface; the detachment of electrons due to the ions and photons impacting the cathode surface. One characteristic of this process is that the lighter electrons will much more efficiently acquire energy from the external field. This usually results in a higher electron temperature compared to the (heavy) ions, since the transfer of kinetic energy between the electrons and heavier particles is inefficient. Apart

from the external applied electric field, the breakdown also depends on the material of and the distance between the electrodes, and on the type and pressure of the gas. For high pressure the mean free path of the species will become very small and for large distances between the electrodes the secondary electron creation is less likely to occur. In this case (*i.e.* for large pd) the discharge will follow a streamer mechanism, creating more localized electron avalanches. The external electric field leads to a separation of the locally created charges, which locally results in an additionally high electric field. This causes more ionization in this heigh-field region resulting in a propagating structure, the streamer. If the streamer reaches the opposite electrode, a spark occurs. When the power supply is enough to sustain this ionized channel between the cathode and anode, an arc discharge is formed.

To prevent a discharge from arcing, a dielectric material can be placed inside the discharge gap, or can be used to cover at least one of the electrodes. During the discharge, charge will accumulate at the insulating layer's surface resulting in an electric field which will counter the externally applied field, causing the streamer to stop growing. To ignite a new discharge, the polarity on the electrodes needs to be reversed. This type of discharge is a dielectric barrier discharge (DBD), which can be used to generate a non-thermal plasma under atmospheric pressure. Because arcing is prevented no high currents will flow.

1.1.1 Atmospheric pressure plasma jets

In the development of plasma sources it can be desirable to work in a remote-mode. This means that there is a distance between the zone of plasma production and the post-discharge region, the treatment zone. Atmospheric pressure plasmas jets (APPJs) can be used to generate such remote plasmas. To prevent the discharge of becoming thermal a DBD (in various designs) can be used and the voltage can be applied in short nanosecond pulses, square (µs) pulses or AC in the kHz range.

APPJs are used in a wide range of environmental, industrial and bio-medical applications, such as air pollution and waste water cleaning, material and surface treatment, and wound healing and sterilization. Due to electron temperatures of a few eV the plasma jets are able to create reactive and charged species. The fact that they can be operated close to room temperature at atmospheric pressure without the risk for temperature sensitive targets (since the heavy species remain at low temperatures), makes them a promising tool for biomedical applications. The positive influence of APPJs in biomedicine stems from the presence of reactive nitrogen and oxygen species generated in these plasma jets.

1.2 This work

The main goal of this work is to acquire insight in the influence of the plasma operation parameters, like the applied voltage and the volumetric flow rate of the feed gas, on the chemical environment in the treatment zone of such a plasma jet. Which is of importance

in understanding and optimizing the mechanisms of the plasma interaction with biological cells.

To study the plasma jet effluent, optical emission spectroscopy is used as the diagnostic tool. This is a non-intrusive in situ method, which can achieve high spatial and temporal resolution, to identify radicals and active atomic or molecular species and therefore gives insight in the plasma chemical processes. By observing the spectral lines of the OH radical, the excited nitrogen molecule and ion, the atomic helium and the atomic oxygen, which were accessible, insight is gained regarding complex reaction pathways in non-thermal plasmas for the production of relevant species. These particles initiate further plasma chemical processes, such as the formation of hydrogen peroxide radicals (H_2O_2), ozone (O_3) and reactive nitrogen oxides (N_xO_y), that play a role in bacterial inactivation for plasma-medicine or decontamination in agriculture [3, 4].

To accomplish this, a spectrograph was built in collaboration with the Electrical Energy System group of the Electrical Engineering faculty and the experimental work is therefore executed in the High Voltage Laboratory, which is unfortunately an electromagnetic hazardous environment that can interfere with the equipment, therefore extra measures must be taken.

Project goals:

- *Building an optical emission spectrograph setup which is electromagnetically compatible with its working environment.*
- *Investigate the influence of the plasma operation parameters on the active species in the effluent of the jet, by means of optical emission spectroscopy.*

1.2.1 Outline

The structure of this thesis is as follows; at first a theoretical overview of the essential involved physics and underlying techniques to build the setup are presented in **Chapter 2**, to substantiate the design choices during this work and to interpret the spectroscopic measurements. In **Chapter 3** the constructed diagnostic spectrograph setup is introduced, after which the experimental setup as well as the measurement procedure are described. Then, in **Chapter 4** the results of the spectroscopic measurements of the active species for the various plasma parameters are presented and discussed. Ultimately, it concludes in **Chapter 5** with a summary of the experimental findings and an outlook for future research.

Chapter 2

Theory

This chapter will briefly cover the theory and concepts required to understand the physics in this work. The aim of this chapter is to provide the reader with a basic notion of optical emission spectroscopy (the diagnostic tool in this work) and how experiments can be performed in an electromagnetic environment which can influence or damage the equipment.

2.1 The non-thermal atmospheric pressure plasma jet

For this research an atmospheric pressure helium plasma jet is used. This plasma jet operates, as the name suggests, at atmospheric pressure and has a low gas temperature. A plasma can be generated from a neutral gas by externally adding energy to it, *i.e.* by applying an electric field across the gas, in order to accelerate the free electrons present there. The energy from the applied electric field transfers much more efficiently to the light electrons than to the relatively heavy ions. Because the temperature of a particle in a plasma is defined as the average energy of its distribution (assuming it is Maxwellian), the electron temperature in gas discharges is therefore usually higher than the ion temperature. Due to the mass difference between electrons and the heavier particles (ions and neutrals), the kinetic energy transfer is relatively inefficient [2]. However, this distribution of energy into the ionized gas depends greatly on the pressure. At atmospheric pressure, the collision frequency between particles is very high, resulting in a significant energy transfer from the electrons to the heavy species. When the temperature of the heavy species becomes equal to the temperature of the electrons the plasma is categorized as thermal. Due to the increase in collision frequency the mean free path of the particles is relatively small when compared to low pressure plasmas. As a result a higher external field is needed to generate the plasma, which can be described by the streamer mechanism. The high external field leads to high localized charge densities, which are separated by the external field. This electric field created by the localized charge density, induces new electron avalanches and so on. This initiates a propagation of the ionization location, called the ionization front. The total discharge belonging to this ionization front is the ionization wave. To prevent the plasma from

becoming thermal, two things can be done. Firstly, is to apply the energy with pulsed voltages to reduce the interaction time of the discharge. Secondly, a dielectric barrier can be used in between the electrodes which will limit the current transfer.

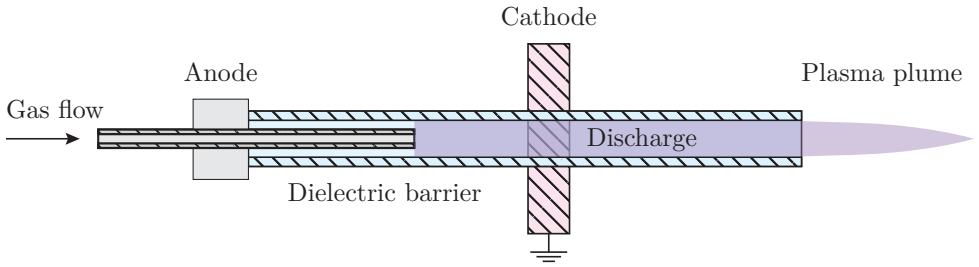

Figure 2.1: Schematic overview of the DBD plasma jet configuration.

There are various DBD plasma jet configurations in which carrier gasses, *e.g.* helium or argon, can be used to drive the discharge [5–7]. In this work a helium plasma jet in coaxial configuration is used, see figure 2.1, with its powered electrode inside a dielectric capillary and a grounded ring-shaped electrode downstream from the anode around the dielectric. To ignite the discharge an AC sine wave of several kilovolts is applied at the anode. The ionization wave initiates from the anode to the cathode. As the inner material is a dielectric, charge accumulates at the surface. When the accumulated charge is enough to shield the applied electric field, the ionization wave starts to propagate past the cathode, further down the capillary. At the end of the capillary the ionization wave continues propagating into the ambient air, creating a plasma plume. These ionization waves exhibit very repeatable behaviour in space and time and are also referred to as 'plasma bullets'. However, the term bullets, suggests maybe falsely, a volume of collected particles as travelling plasma. Therefore, the term guided streamer is more appropriate, indicating the propagating ionization waves are like streamers but without the stochastic behaviour. This reproducibility is generally ascribed to a memory effect, in which the electrons for the next discharge are remnants of the previous one.

2.2 Optical emission spectroscopy

Electromagnetic waves extend over a wide wavelength range. The visible range, which can be seen by the human eye, is only a very small part ranging from 380 nm to 780 nm. Radiation in this spectral range originates from atomic and molecular electronic transitions and just by looking at the color of a plasma, information on the plasma can be acquired. The color of the plasma is characterized by the heavy particles, *i.e.* neutrals and ions, and typically a neon plasma is colored red, nitrogen plasmas are orange, helium are pink and hydrogen are purple. Plasma emission spectroscopy is one of the most well-established diagnostic tools to spectrally resolve the electromagnetic radiation emitted by the plasma. Optical emission spectroscopy (OES) is a non-intrusive technique, which means it can provide information on the excited species present in the

discharge without perturbing the plasma, and insight on the molecular and atomic dynamics, *i.e.* chemical reactions in the plasma, can be obtained. The emission from a plasma can be grouped into two categories: radiation from decelerated charges (Bremsstrahlung) and radiation from emitting atoms and molecules. Only the latter will be described here. The following literature [8–14] has been used to describe the concepts in this section.

2.2.1 Line profiles of spectral lines

The underlying process of this radiation is based on energy transitions of the atoms, molecules and ions. The transition from a lower energy state (E_l) to an upper state (E_u) can be caused, for instance, by absorption of a photon or by electron impact. Thereafter, this excited particle can spontaneously decay from this upper state to a lower energy level while emitting a photon. The photon has a wavelength of λ_0 corresponding to a discrete energy step, $\lambda_0 = hc/(E_u - E_l)$ (with Planck constant h and speed of light c), see figure 2.2. Beside an energy distribution in electronic states, like atoms, molecules also contain vibrational and rotational energy states (due to motion in its internal structure). Not every radiative transmission, which could be predicted based on the energy levels, is actually observed in the spectra. This originates from the fact that besides energy conservation, the conservation of angular moment and certain symmetry rules must also be obeyed. Since each species has a definite set of allowed transitions, the emission spectra can be used to identify the particle.

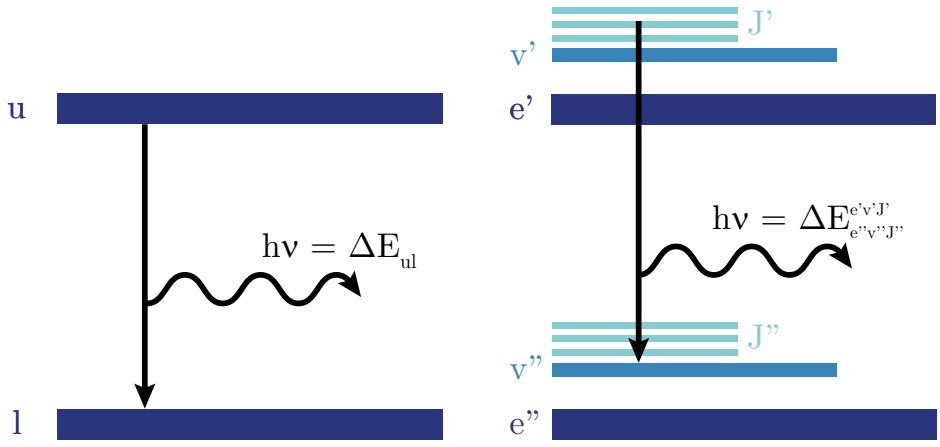

(a) Atomic transitions **(b)** Molecular transitions

Figure 2.2: Atomic and molecular species posses well defined electronic energy states. Besides the electronic states, the energy states of molecules consist of well defined vibrational and rotational states, with decreasing energy distances.

Next to its wavelength position λ_0 a spectral line is defined by its profile. The lines are not infinitely thin (see figure 2.3) and the profile shape and width (Full Width Half Maximum) contains information about the plasma properties. The intensity of the line

depends on the population density of the excited level (which is strongly affected by the electron, ion and particle temperatures/densities).

This line shape function I can be expressed in wavelength λ, frequency ν or angular frequency ω. The FWHM in terms of wavelength is defined as $\delta\lambda = |\lambda_1 - \lambda_2|$ with $\frac{1}{2}I(\lambda_0) = I(\lambda_1) = I(\lambda_2)$. Although the relative FWHM (2.1) are the same in all three units-schemes, converting the profile from wavelength units into angular frequency (λ is usually the experimental unit and ω is preferred in theoretical calculations) a wavelength factor should taken into account. From $\lambda = c/\nu$ and $\omega = 2\pi\nu$ follows (2.2).

$$\left|\frac{\delta\lambda}{\lambda}\right| = \left|\frac{\delta\nu}{\nu}\right| = \left|\frac{\delta\omega}{\omega}\right| \tag{2.1}$$

$$\delta\lambda = \frac{\lambda^2}{2\pi c}\delta\omega \tag{2.2}$$

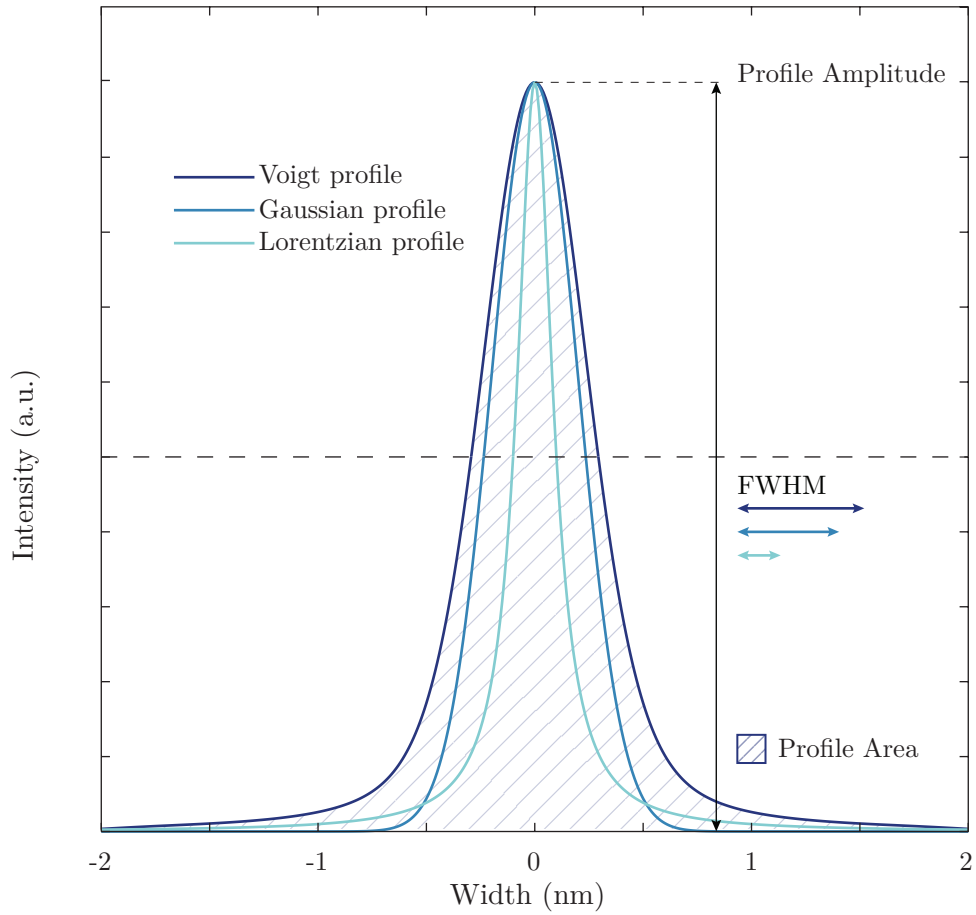

Figure 2.3: Voigt, Gaussian and Lorentzian spectral line profiles. The respective FWHMs with equal profile amplitude are indicated by the arrows.

The width and shape of a spectral line results from a number of different broadening mechanisms. A line can be broadened by the instrument used to record the spectrum,

mechanisms related to the plasma or due to intrinsic physical causes. Each mechanism has a corresponding profile, *i.e.* a Gaussian or Lorentzian profile, equation (2.3) and (2.4), respectively. The observed spectral line is a result of a superposition by convolution of these mechanisms, with a FWHM which is larger than the individual contributions. Usually, the line profile is a convolution of both profiles resulting in a Voigt shape profile defined by equation (2.5). The Voigt profile is flatter in the center and broader in the wings of the line compared to the corresponding Lorentz and Gaussian profiles [15]. The derivations of these profile functions expressed in the FWHM parameters w_G and w_L are described in appendix E.

$$G(x) = \frac{A_{rea}}{w_G \sqrt{\frac{\pi}{4\ln 2}}} e^{-\frac{4\ln(2)(x-x_c)^2}{w_G^2}} \tag{2.3}$$

$$L(x) = \frac{2 \cdot A_{rea}}{\pi} \frac{w_L}{4(x-x_c)^2 + w_L^2} \tag{2.4}$$

$$V(x) = A \frac{2\ln 2}{\pi^{3/2}} \frac{w_L}{w_G^2} \int_{-\infty}^{\infty} \frac{e^{-\xi^2}}{\left(\sqrt{\ln 2}\frac{w_L}{w_G}\right)^2 + \left(\sqrt{4\ln 2}\frac{(x-x_c)}{w_G} - \xi\right)^2} \, \mathrm{d}\xi \tag{2.5}$$

The convolution of two Gaussian profiles results in a Gaussian profile, likewise the contributions of two Lorentzian profiles will result in a Lorentzian profile. Therefore the contribution of w_G and w_L components in the Voigt profile are given by (2.6).

$$w_G = \sqrt{\sum_i w_{G_i}^2} \quad \text{and} \quad w_L = \sum_k w_{L_k} \tag{2.6}$$

Line broadening mechanisms

From these broadening parameters valuable plasma quantities can be deduced, *e.g.* electron density or plasma temperature. However, to realize this, competing line broadening mechanisms (*i.e.* mechanisms with the same profile) must be considered and their contributions should be estimated and subtracted.

Depending on the interest in a specific feature of the spectral line, *i.e.* wavelength position, FWHM or peak intensity, special attention must be paid. Due to self-absorption in the plasma volume, the intensity at the center wavelength can be significantly lower resulting in a incorrect measurement of the FWHM, as well as for the choice to use the peak area or peak height when measuring the relative intensity, if adjacent lines significantly overlap.

In the scope of this work, whereby the intensity of spectral lines is measured, the broadening of the line is of importance due to overlap of closely spaced lines to correctly obtain the profile area.

Natural broadening is caused by the finite lifetime of excited states. It follows from the Heisenberg's energy-time uncertainty principle $\Delta E \cdot \Delta\tau \geq \frac{h}{4\pi}$. Without external influences, the lifetime $\Delta\tau_u$ of an energy state u is determined by the sum of all possible transition probabilities from this state to all lower lying levels l (given by $\Delta\tau_u^{spont} = 1/A_u = 1/\sum_l A_{ul}$). From the uncertainty in the energy transition a broadening in the spectral wavelength λ_0 follows:

$$\Delta\lambda_{natural} = \frac{A_u\lambda_0^2}{2\pi c} \tag{2.7}$$

This broadening is usually negligible (in the order of 10^{-4} nm [16]).

Inelastic collisions with other atoms or molecules will also contribute to the total transition probability $A_u = 1/\Delta\tau_u^{spont} + \sigma_i p\sqrt{8/(\pi\mu k_b T)}$ (with σ_i as the inelastic cross-section, p the partial pressure of the other particle and μ the reduced mass). These collisions are called quenching collisions because they shorten the lifetime and therefore reduce the population of energy level u. The broadening related to these lifetimes have a Lorentzian profile.

Collisional broadening is due to interactions between the radiating particles and other particles in the plasma. These interactions will cause perturbations in the energy levels related to the emission line. Resonance and van der Waals broadening are related to interactions with ambient neutral particles, and Stark broadening is caused by charged particles. These so called pressure broadening mechanisms result in an approximately Lorentzian profile.

Resonance broadening can only occur between identical species (self-broadening), if either the upper or the lower energy level of the emitted line is a resonance transition, *i.e.* one of the two levels has a dipole transition to the ground state. The interaction between the perturber and radiator can be approximated by a dipole-dipole potential $V(r) \approx -\frac{C_3}{r^3} - \frac{C_6}{r^6} - ...$ [17]. This leads to a broadening given by (2.8), with n_g the density of ground state particles in [m^{-3}] and $f_r(g \to u, l)$ the oscillator strength between the ground state and upper or lower energy level. With g_u and g_u, l are the statistical weights of resonance state. The resonance wavelength λ_r and λ_0 are in [nm].

$$\Delta\lambda_{resonance} \approx 9 \times 10^{-34}\sqrt{\frac{g_g}{g_{u,l}}} f_r(g \to u, l)\lambda_0^2\lambda_r n_g \tag{2.8}$$

Van der waals broadening is characterized by shorter range forces than those with charged particles. When the neutral particles do not share a resonant transition the first order term (C_3) will disappear resulting in an interaction potential influenced by van der Waals force. The C_6 term may be expressed as: $C_6 = e^2 a_0^2 \overline{\alpha}\overline{R^2}$, with elementary charge e, a_0 the Bohr radius, $\overline{\alpha}$ the atomic polarizability of the neutral perturber and $\overline{R^2} = \overline{R_u^2} - \overline{R_l^2}$ the difference of the squared radius of the emitting particle upper and lower levels. From this an estimation for the van der Waals broadening is given by equation (2.9), the wavelengths are in [nm] units, T_g in [K], the reduced mass μ in [a.m.u]

and the particle density is given in [m^{-3}]. In this work the gas composition in the plasma consists primarily of helium atoms [18]. Therefore, the atomic polarizability of the neutral perturber is $2 \times 10^{-25}\,cm^{-3}$ [19] and n_g is the density derived from the ideal gas law. Resulting in a van der Waals broadening in the order of 10^{-2} nm comparable with [20]).

$$\Delta\lambda_{vdWaals} = 8.18 \times 10^{-25}\lambda_0^2 \left(\overline{\alpha}\overline{R^2}\right)^{2/5} \left(\frac{T_g}{\mu}\right)^{3/10} n_g \tag{2.9}$$

Stark broadening is caused by the coulomb interactions between charged particles present in the plasma and the radiating species, with the major contribution due to high velocity electrons. Due to long-range Coulomb interaction a general solution is impossible, and because the electric field generated by the slow ions is "static" during the emission of a radiating particle it is therefore often neglected. The line shape can be approximated by a Lorentzian profile, with the Stark broadening width given by (2.10), Z_p and Z are the charge of the perturbing and emitting particles, respectively in units of e, m the emitting particle mass [kg], n_u and n_l the principle quantum number of the upper and lower state, respectively and the pertuber particle density n_p is given in m^{-3}.

$$\Delta\lambda_{Stark} = \frac{6Z_p\hbar\lambda_0^2}{\pi cZm}\left(n_u^2 - n_l^2\right) n_p^{2/3} \tag{2.10}$$

The Stark broadening is in the order of 10^{-3} nm [20, 21]. This broadening will increase with electron density and will become significant at $n_e > 10^{18}\,cm^{-3}$ [22]. However, those electron densities are not expected for the type of atmospheric helium jets used in this work [23, 24].

Doppler broadening is due to thermal motion of the emitting particles relative to the observer. Due to the velocity component in respect to the observer the emitting wavelength appears to be Doppler-shifted. Assuming the velocity distribution of the emitting particles is Maxwellian (characterized by a temperature T_g), will result in a Gaussian (profile) wavelength distribution. The FWHM of this profile, the Doppler broadening, is given by (2.11) with A_m the mass of the radiating particle (in atomic mass units). With the temperature ≈300 K estimated from [18] the broadening will be in the order of 10^{-3} nm to 10^{-4} nm.

$$\Delta\lambda_{Doppler} = 7.16 \times 10^{-7}\lambda_0\sqrt{T_g/A_m} \tag{2.11}$$

Instrumental broadening is independent of the plasma properties and is introduced by the optical system to record the spectrum. The apparatus profile is determined by the spectrometers parameters, like the focal length, type of grating, entrance and exit slits. In the spectral measurements in this work an entrance slit of 50 µm was used resulting in an instrumental broadening in the order of 10^{-1} nm, with a Gaussian profile. Obtaining the instrumental broadening is described in appendix C.

2.3 Spectrograph

The light emitted by the plasma is collected by a spectroscopic system, the spectrograph, which has the ability to separate the light, and forms a spectrally dispersed image of the object in the exit plane. A spectrograph typically consists of collecting optics, a narrow aperture, imaging mirrors, a dispersive element and a detector in the exit plane [25].

2.3.1 Spectrometer

One of the main components is the spectrometer. In this work the spectrometer is a Czerny-Turner configuration (see figure C.1), which consists of the entrance slit, a collimating and focussing mirror (the imaging mirrors used to reduce aberrations) and a grating (the dispersive element). The physical size of the grating together with the focal length of the spectrometer defines the aperture, and hereby the amount of light that passes through, influencing the spectral resolution. A larger entrance slit will increase the light throughput and results in a higher intensity image; however, with less spectral resolution. To disperse the light a collimated (parallel) beam on the grating is required. Therefore, the light from the entrance slit will first reflect on a collimator, towards the grating.

Grating

The grating surface can be pictured as a large set of small grooves with a small spacing, d, between the grooves. Each groove will diffract the light, and the combined effect results in interference (constructive/destructive). Dependent on the incident angle α (seen from the grating normal), the light with wavelength λ, will only reflect under the angle β. This relationship is described by the grating equation (2.12), in which m is the diffraction order.

$$m\lambda = d(\sin\alpha + \sin\beta) \tag{2.12}$$

The grating is characterized by the grooves per millimeter G and the blaze angle (the highest reflection efficiency of the grating). The primary purpose of the grating is to disperse light spatially by wavelength. The light disperses according to the angular dispersion equation (2.13). As the groove frequency increases (the spacing between the grooves decreases) the angular dispersion increases, resulting in an increase of angular separation between the wavelengths given for order m.

$$\frac{\mathrm{d}\beta}{\mathrm{d}\lambda} = \frac{mG \cdot 10^{-6}}{\cos\beta} \tag{2.13}$$

By rotating the grating, the wavelength focused in the exit slit can be selected. However, the biggest issue when using a reflecting grating is that successive spectra overlap due to the multiple order behaviour. This superposition of spectroscopic data must be prevented with filters, since the detector cannot normally distinguish between

light of different wavelengths incident on it. Measurements in air up to ≈380 nm can be conducted without filters, because wavelengths below ≈190 nm are absorbed.

2.3.2 ICCD Camera

The detector is placed in the exit slit, generally a photomultiplier (PMT) or, like in this work, an intensified charge-coupled device (ICCD) camera. The camera is coupled to an image intensifier which enables measuring very weak light sources as well as short light pulses. The intensifier has three main parts: the photo-cathode, a multi channel plate (MCP) and a phosphor screen. The incoming photon on the photo-cathode releases an electron, this electron is accelerated to the MCP by a control voltage. In the MCP the electrons are accelerated and amplified to an electron avalanche, based on an adjustable gain voltage. Finally, the phosphor screen converts the multiplied electrons back into photons, which are coupled to the CCD by a lens or fibre optics. The intensifier makes fast operating of the camera possible. By reversing the control voltage on the photo-cathode the shutter of the camera can be opened or closed.

Noise

Unfortunately, in the detection phase noise is introduced which will reduce the quality of the acquired image. The total noise is build from shot noise, dark signal and readout noise [26]. Shot noise is unavoidable and exists because the emitted light arrives in discrete "packets", in terms of photons. The photons are emitted at random times, and the detection of the number of photons are independent of each other. At high intensity this variation is very small to detect, but for low brightness, when only a handful of photons arrive at the detector, this fluctuations will be significant. It is expected that every electron arriving at the CCD originated from the observed object. However, even with the shutter closed, some electrons are still accumulated. This dark signal arises from thermally generated electrons in the CCD sensor, this undesirable signal can be minimized by cooling the CCD. The read-out noise is added during analog-digital conversion and shifting of the electrons in the pixels on the CCD. This effect on the image can be reduced by slower or fewer readouts (acquiring multiple events before readout), by binning of the pixels, and background subtraction of the image.

2.3.3 Optics

The last part of the spectrograph consists of the collecting optics to focus the emitted light on the entrance slit, this can be done with an optic fibre and with lenses. The material, shape and orientation of the lens has an influence on the effectiveness and can be more convenient to work with. Standard glass lenses will become opaque towards lower wavelengths, therefore quartz lenses are the better choice when the region of interest is in the ultraviolet area (<380 nm). The lenses will introduce some degree of distortion of the image when focussing on the entrance slit, and an out of focus image will result in a loss of signal strength (see figure 2.4). The goal is to distribute the refractive power

across both surfaces of each lens to reduce aberrations. The correct way to orientate the lenses is with the curvature towards each other. If you orient the planar surface towards the collimated beam, no refraction occurs there and the angles on the other surface have to be greater, which induces more aberration.

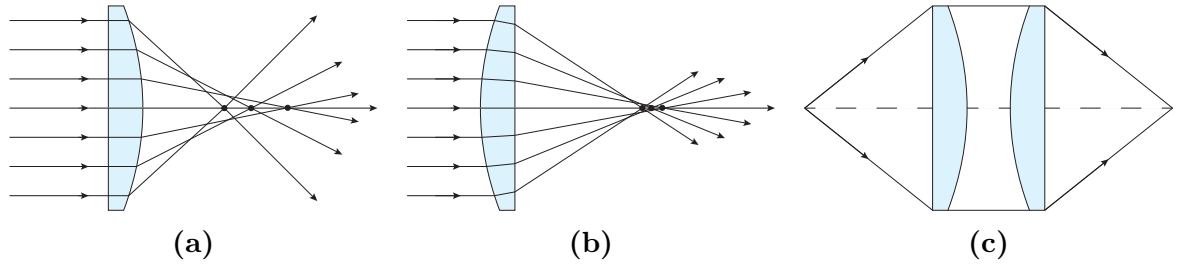

Figure 2.4: Illustration on lens orientation influences the imaging, (c) shows the correct orientation of two plano-convex lenses to minimize the spherical aberration.

2.4 Electromagnetic Compatibility

In this work the experiment will be conducted in a heavily electromagnetically disturbed environment. Although the mutual interference between electronic devices is as old as electromagnetism itself, there is not always awareness of the impact it can have on the results and will often only be noticed when there is nuisance encountered in operation. The following literature has been used to explain the theory in this section [27–29].

Electromagnetic compatibility has two main aspects; the ability of an electronic device to function properly in its electromagnetic environment and to not be a source of intolerable interference signal. There are three elements in an EMC problem, the noise source (aggressor), the interference coupling path and the susceptible receptor (victim). When the receiver is close to the source (close field is up until approximately one-sixth of a wavelength of the field), electric and magnetic field coupling are considered separately, but in the far field this is considered as combined electromagnetic radiation. The interfering mechanisms through radiation or by conducting both cause unwanted currents in the device. For example a wire, like a power supply lead, running through a noisy environment may pick up noise if no shielding is applied and will conduct this into another circuit. Due to increasing densities in circuits this causes not only malfunctions between devices, but also on a chip level.

To combat interference problems it is good to know what is small/big, close or far away. An important quantity is the wavelength of the noise signal. A system is small if the dominant dimensions in it are small (a tenth of the wavelength or smaller) compared to the wavelength. In such a system variations in the signal are quasi-stationary and can be described with normal network theory (without the need to solve Maxwell's equations to describe the behaviour of an electric circuit). For higher frequency the wavelength will decrease and a system will be no longer considered small.

Although there are many methods to reduce interference, such as shielding, grounding, filtering, isolation and more, they often should already be considered in the design phase on the circuit level of the equipment. In this work we utilize more or less off-the-shelf equipment to do the experiment. Therefore, shielding is the best way to acquire measurements without environmental noise whilst protecting the setup from damage.

2.4.1 Shielding

Metal plates or plastic covered in a conductive coating are used as enclosure material for shielding. The enclosure can be used to prevent escape of electromagnetic fields if it surrounds the noise source. It can also be used to keep the electromagnetic radiation out of specific areas, to provide protection to susceptible equipment. In the environment of this work the disruptive phenomena are also the ones to be studied; therefore, they are left undisturbed and is it more practical to shield the equipment. Because, in this work, the aggressors are mostly in the far-field (further away than a sixth of the wavelength), the shield-effectiveness shall only be described for this case.

The shield-effectiveness is a measure of how well an enclosure attenuates electromagnetic fields, described by the amplitude ratio of the field inside and outside the wall. The effectiveness of the enclosure to attenuate the electromagnetic fields depends on two factors; one is the shield material and the other is the apertures and seams in the shield. The analysis of the shielding material effectiveness can be approached in two ways; in the circuit theory the incoming fields will induce currents in the conducting material and those currents will generate opposing fields to cancel the original fields. In the field theory approach, the total shielding effectiveness is described as the absorption and reflection loss of the EM-field, which occurs at air-metal and metal-air interface transitions (see figure 2.5).

The intensity of the wave in the shield follows an exponential decrease ($\propto e^{-t/\delta}$) over the material thickness and is dependent on the skin-depth δ. This skin-depth results from the fact that the field will induce an alternating current of which the majority of the charge will flow near the surface at the skin of the conductor (contrary to direct current, in which the current density is almost homogeneous inside a conductor). This induced current produces heat in the material by ohmic losses, which results in the absorption of the wave. Depending on the frequency of the incident field and shield material, the skin depth can vary from a few millimeters till a hundredth of a millimeter (for frequency ranging $\sim$ Hz - MHz). Therefore, at low frequencies the contribution of absorption damping to the shield-effectiveness will be diminished (unless thick material is used) and instead the shielding will be dominated by the (multiple) reflection damping at the interfaces. The reflection damping at the interface is related to the characteristic impedance between the two media, therefore, plane wave reflection damping is mainly dependent on the material type. Because some materials are better in absorption but worse in reflection than others, the choice of shield material depends on the noise frequency. In practice it is the case that a mechanically strong enough metal that can serve as a housing is also suitable for providing sufficient damping for fields. However, it is not realistic to have a complete solid

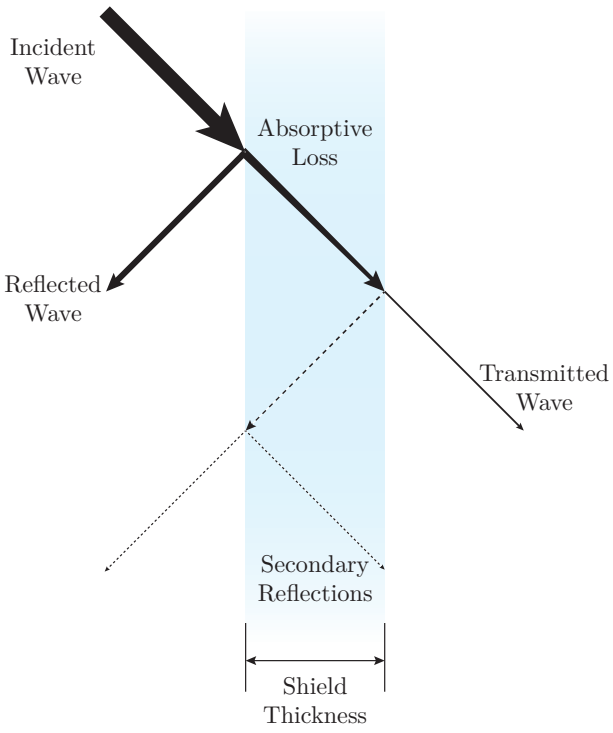

Figure 2.5: Schematic illustration of reflection, absorption and transmission of an incident EM wave at both interfaces of the shield medium.

enclosure without any openings or seams. Therefore, special attention has to be paid to openings regarding to the shielding effectiveness of enclosures.

Shield enclosure design and apertures

Openings in the enclosure are necessary to send measurement and/or control signals, to have cooling, to have power for the equipment inside and more. These apertures can have, if the construction design is wrong, a great impact on the shield effectiveness. From the circuit theory approach it can be visualized (see figure 2.6) that the leakage from a shield depends on the maximum dimension of an aperture rather than the area. To cancel the incoming field, the induced shield currents must be able to flow as undisturbed as possible. As you can see in figure 2.6c, the effect of a narrow slot on the current path is almost the same as for a much larger opening like in 2.6b, and as a consequence both have the same leakage.

High frequency electromagnetic wave can propagate through an aperture/waveguide without any loss, think, for example, of light shining through a pipe. However, there is a critical wavelength λ_c above which no electromagnetic energy can propagate and will be damped a short distance into the pipe. This critical wavelength is dependent on the propagation mode of the field in the pipe. You can see an aperture in the enclosure more or less as a very short pipe, which defines the cross section upper limit of the hole because the

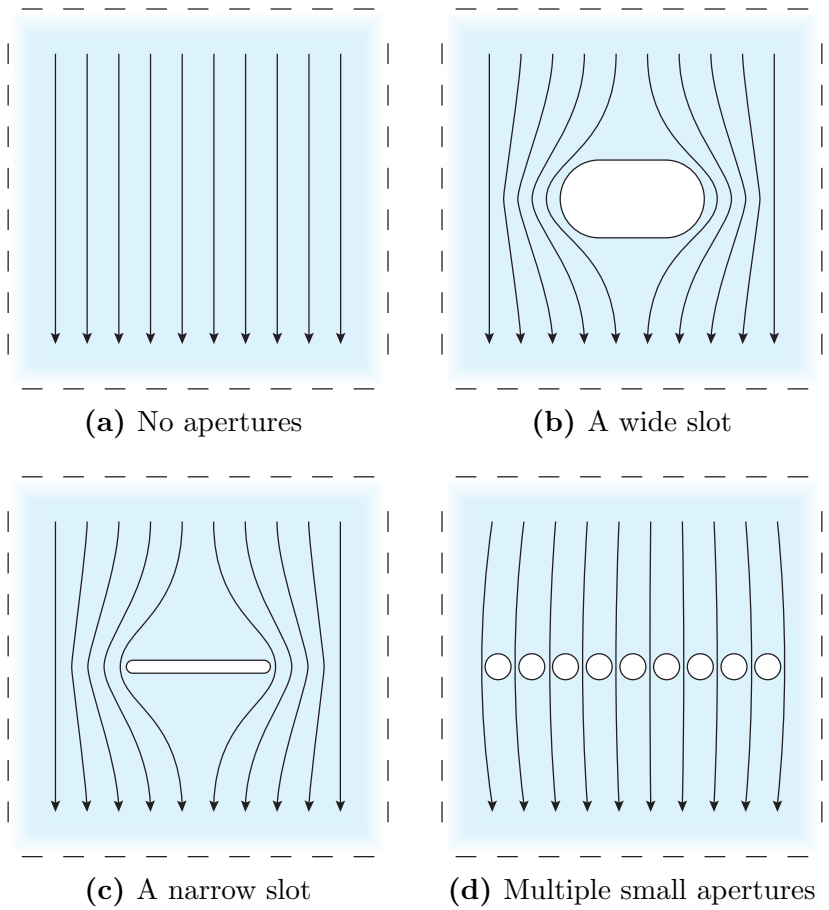

(a) No apertures **(b)** A wide slot

(c) A narrow slot **(d)** Multiple small apertures

Figure 2.6: Visualization of the induced shield current paths influenced by the shield apertures.

critical wavelength is (depending on the shape) approximately twice the largest dimension of the aperture. Because of this the aperture should be smaller than the wavelength of the field that needs to be damped. For additional attenuation it is good practice to extend the opening (both ways) to form a waveguide below cutoff, see figure 2.7.

In the construction of a shielded enclosure seams can occur at welds in the material without proper galvanic contacts, but also appear naturally at covers and doors of the shield enclosure. A seam can be seen as a narrow slot, which can therefore cause a major leakage problem. To seal the enclosure electromagnetically properly, conductive casket or finger-stock needs to used which will provide electrical continuity across joints when compressed. See figure 2.8 for some examples of how to seal enclosures.

Finally, it is of little use to have a shielded enclosure for radiation and then allow electromagnetic energy to pass this barrier by alternative paths such as cable penetrations. Therefore, cables should always be shielded and/or filtered with fully connection to the enclosure.

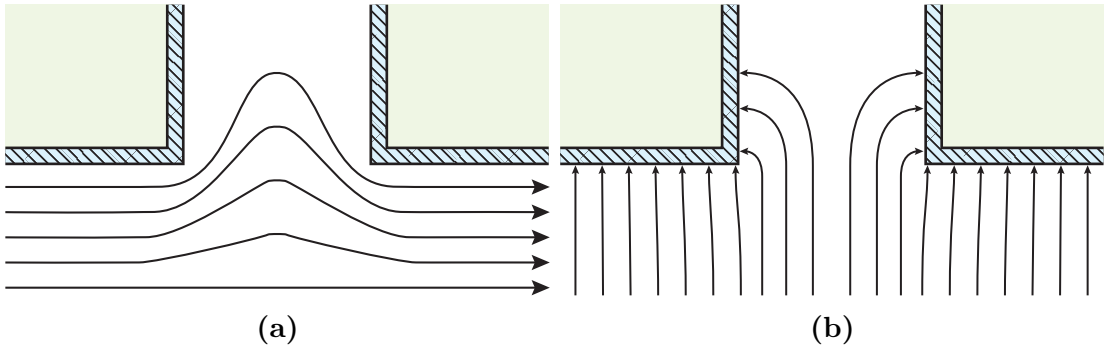

Figure 2.7: Illustration of the effect on (a) magnetic, (b) electric field lines, due the aperture extension in an enclosure to form a waveguide.

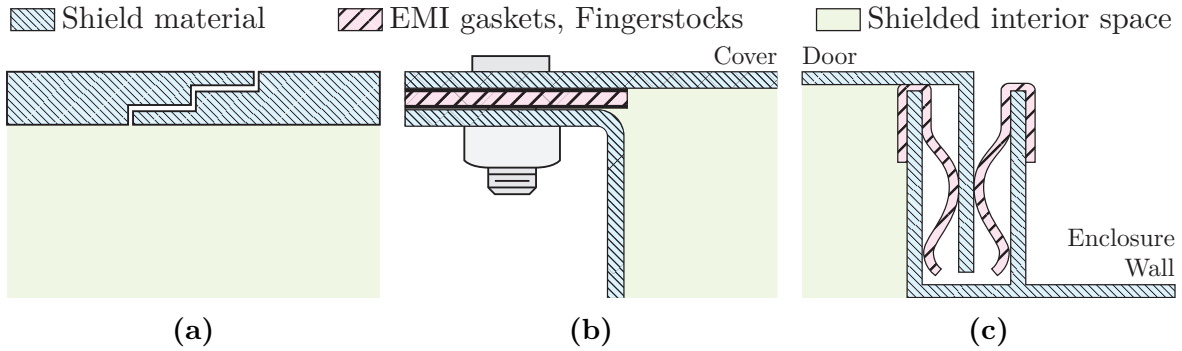

Figure 2.8: Examples to protect the interior shielded space from seams leakage. (a) Overlap of material is better if applied staircased. (b) External bolting of mechanical joints prevents leakage. (c) Construction all around the opening in an enclosure to allow good galvanic contact of the door.

Chapter 3

Experimental Setup and Procedures

This chapter presents an overview of the experimental setup and procedures and is divided into four parts. Firstly, the design and construction of the spectrograph setup, the diagnostic tool of this work, is described (figure 3.1 shows the full scale of the instruments). Secondly, the experimental setup and the design of the used atmospheric pressure plasma jet is given. Thirdly, the plasma operating parameters in this work, like applied voltage and volumetric gas flow, as well as the measuring procedure that is used for investigating the spectral regions are discussed. Finally, it will be clarified how the raw acquired images were processed to obtain the measurement data.

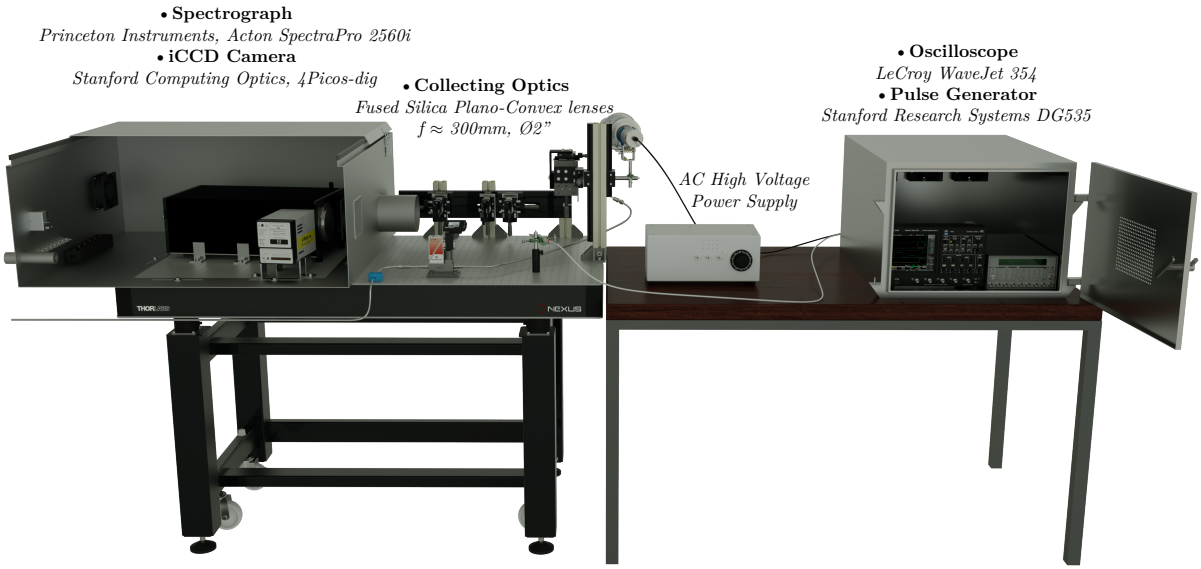

Figure 3.1: Illustration of the complete constructed setup which is used to perform the experiments in this work.

3.1 Constructing the spectrograph setup

The two main components of the spectrograph are a Princeton Instruments Acton SP2560i spectrometer and the Stanford Computer Optics 4Picos-dig ICCD camera. For the specifications of those instruments see appendix A.1. The fully constructed spectrograph results in a broad sensitive wavelength range from 200 nm to 800 nm with a minimum shutter time of 200 ps. An optical emission diagnostic tool, capable of operating in an electromagnetically hazardous environment (Eindhoven University of Technology - High Voltage Laboratory).

3.1.1 Camera & spectrometer connection

In order to acquire sharp images, the CCD of the camera needs to be correctly positioned in the spectrometer exit focal plane. To achieve this, a new c-mount housing for the side panel of the spectrometer had to be designed and constructed. Furthermore, due to the connection mechanism of the camera (which is a screw with a rather large pinch), the focal plane and CCD were not parallel to each other when the c-mount clamp screw was tightened. This resulted in a broadening of the spectral lines in the regions off center of the acquired images. This was resolved by inserting a c-mount spacer between the camera and mounting flange. Figure 3.2 shows the new situation to connect the camera to the spectrometer. For the technical drawings of the adapter plate, mounting flange and spacer see appendix B.1. After this, the CCD was positioned parallel and in focus range, now the focus mirror of the spectrometer needs to be positioned. The adjustment to the focusing mirror is explained in more detail in section C.1.

3.1.2 Design construction: EMC precautions

To make the spectrograph electromagnetic compatible an EMC cabinet is constructed. The EMC cabinet is designed; to benefit from its breadboard base, to be flexible so it can be used in future experiments, but above all, to protect the equipment for EM interference. The design follows from some certain guidelines resulting from experiences in the high voltage lab and the EMC theory as described in section 2.4.

The electrical components of the spectrograph are placed in an EMC cabinet made out of 3 mm thick aluminium sheets with a lid on top, see for an illustration figure 3.3. To prevent EM leakage due to the lid, a clip-on nickel over foam gaskets is used around the edge, which will ensure the galvanic contact. The power for the equipment inside is supplied by an IEC inlet filter connected to the cabinet. To prevent heating of the interior of the cabinet during operation, fans are placed for air flow. These apertures are shielded with fan covers of stainless steel wire mesh. The signals from and to the camera, *i.e.* the trigger signal from the pulse generator and the camera gating to the oscilloscope, enter the cabinet via a BNC feedthrough which is tightly connected to the cabinet. Unfortunately, the usage of a few wave guides cannot be avoided in the design. Firstly, a connection with the computer needs to be established in order to control the spectrometer and camera settings, the motorized entrance slit width and filter wheel, but

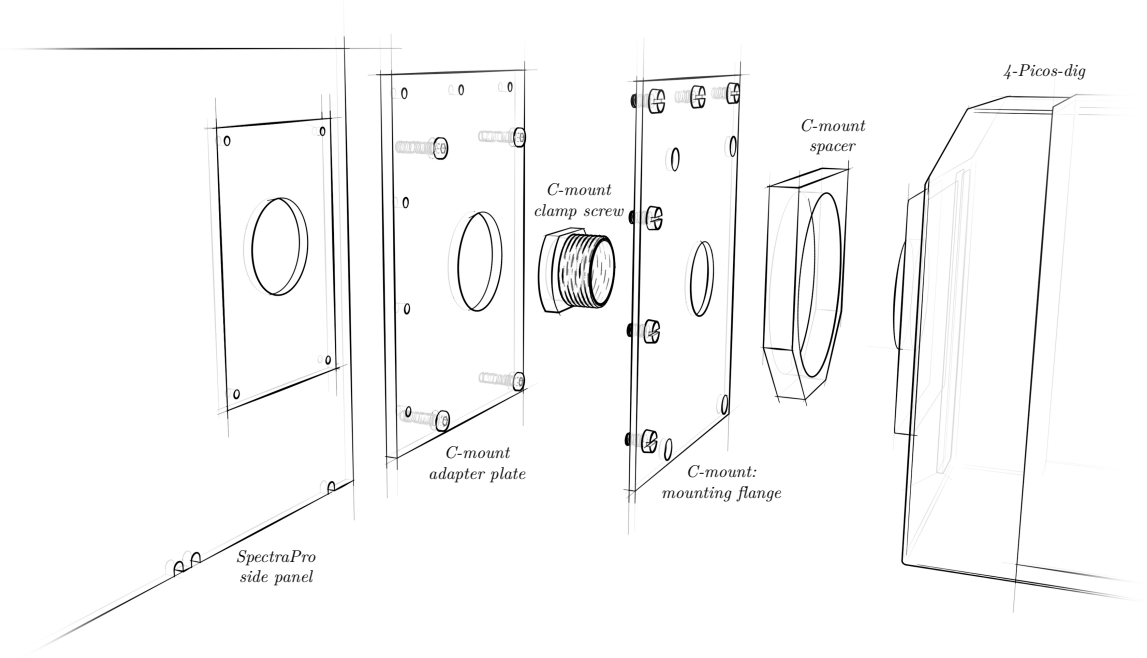

Figure 3.2: Illustration of the camera spectrometer housing connection.

also to retrieve the measurement data. An optic fibre is used to facilitate this connection, after entering the shielded enclosure it will be converted to USB port connection. In addition, there are two more wave guides to allow the spectral emission of the observed object to enter the spectrometer. A small one for an optic fibre, but special attention in the design is paid to the wave guide which provides the direct light focusing on the spectrometer entrance. It had to be ensured that the aperture diameter was wide enough to allow the light to be focussed with the maximum acceptance angle (see the following section 3.1.3). Finally, the cabinet, equipment and breadboard are connected to the same ground potential.

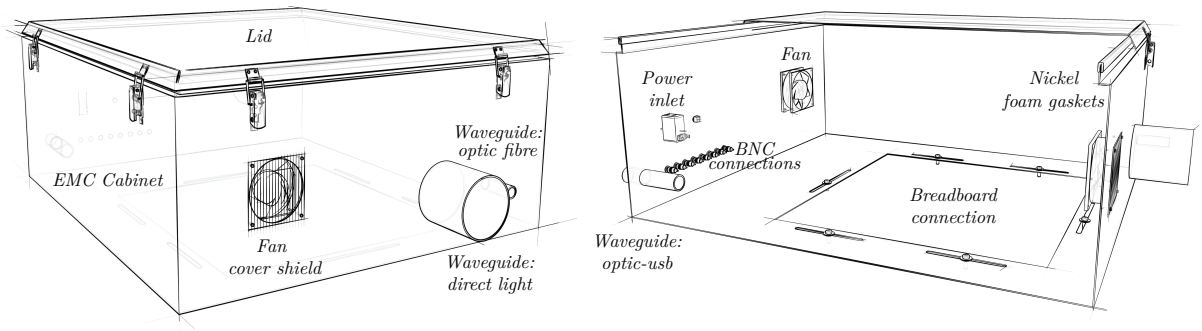

Figure 3.3: Drawing of the constructed EMC cabinet.

3.1.3 Collecting the light emission

The spectrometer has two entrance slits, which will both be used to expand the possibilities of the spectrograph for different purposes. The side entrance is coupled with an optic fibre. A fibre has the advantage of being able to transport emission of objects from a distance to the spectrograph; however, it comes at the expense of losing spatial resolution. The front entrance is directly lighted by the object emission. This light is focused with lenses forming a direct path from the object. A direct light path has the advantage that the spatial resolution is retained which benefits this research, whereby the local emissions of active species are examined.

To transfer the object image to the entrance slit, is has been decided to build the optical collecting system with two plano-convex lenses. A two lens system has the advantage of easing the focusing procedure without the need to vary the object-image distance, and when orientated correctly (curved inwards as been illustrated in figure 2.4c) it will decrease the spherical aberration compared to one stronger biconvex lens. However, a disadvantage is a weaker light signal, due to the increase of reflections at each lens interface.

To obtain maximum resolution and signal strength the light should enter under the widest possible angle which is acceptable for the spectrometer. This acceptance angle or f-number of the spectrometer is determined by the focus length and the area of the collecting mirror/grating. Optimal performance is achieved when the f-number of the coupling optics is matched with the spectrometer f-number, resulting in complete exposure of the internal optical parts without introduction of stray light inside the spectrometer. Considering the cabinet's waveguide dimension and the acceptance angle, two uncoated quartz lenses (⌀2 inch and $f \approx 300\,\text{mm}$) are used for the collective optic system. However, because the gratings differ in dimension, a diaphragm is also positioned between the two lenses to create a slight under fill for the largest grating. Nonetheless, this is not a problem because a diaphragm will also prevent the light from propagating throughout the regions of the lens where the spherical aberrations are introduced the most.

3.1.4 The control and post-processing software

Apart from the necessity to get the hardware working with accompanying software for the spectrograph as well as for the camera (which was not trivial for the Stanford Computer Optics camera, see appendix A.2 for a detailed intallation manual), two software applications have also been developed, the interfaces are displayed in figure 3.4.

Firstly, the wish arised for a semi-automated setup from the need to keep track of a lot of measurement data at possibly various delay times. For this purpose the application Run Experiments was written, see for the documentation appendix D.1. Run Experiments allows the user to automatically generate measurements including a log and settings file.

Secondly, Image Processor was developed for the need to translate those raw measurement images into wavelength and intensity values, but also to do this in a visual and intuitive manner. The documentation on this Image Processor application can be found in appendix D.2.

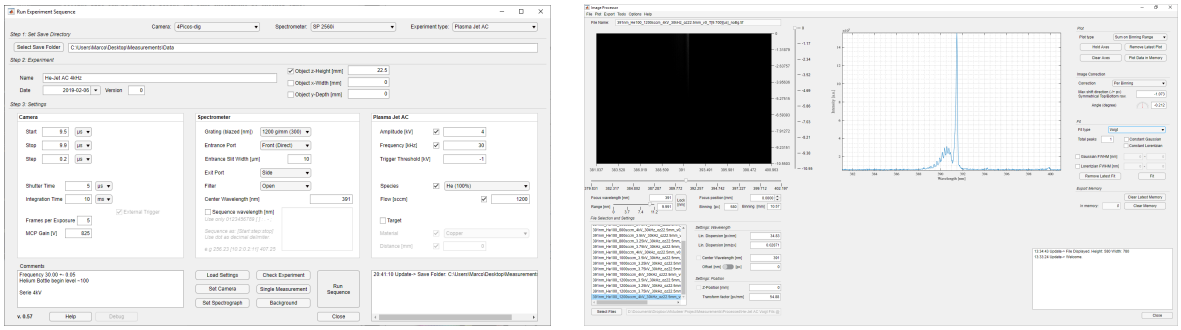

(a) **(b)**

Figure 3.4: Interface of the MatLab applications which are developed. **(a)** Run Experiments, for automating the measurements acquisition. **(b)** Image Processor, to post-process the raw measurement images.

3.1.5 Calibration of the diagnostic tool

Now that the construction of the spectrograph is complete, the acquiring of the raw spectral measurements can almost begin. First, as described before, the spectrograph should be focused and some specification numbers for post-processing need to be acquired. The proceedings for positioning of the focus mirror, correction of the camera angle orientation ($-0.21°$), determination of the linear dispersion for various wavelength (ranging from 34.18 px/nm to 40.32 px/nm), the spatial resolution (54.88 µm/px) of the observed object, the broadening of the spectral lines and spectral sensitivity are described in detail in appendix C.

3.2 Measurement system and plasma source

In this study discharges generated with a plasma jet at atmospheric pressure are examined by means of optical emission spectroscopy. The experimental setup and plasma source will be described in this section and are schematically illustrated in figure 3.5.

There are various jet designs which can generate plasma bullets, in this work a coaxial geometry is used. The plasma jet is operated in a vertical orientation with effluent of jet pointed downwards. It is connected to an AC power supply operating at 30 kHz. The powered electrode is made of stainless steel and also serves as the gas inlet. It has an inner diameter of 0.8 mm and an outer diameter of 1.6 mm and is centered in the middle of a pyrex capillary. The capillary has an inner diameter of 2.4 mm and an outer diameter of 4 mm, with a 3 mm thick metal ring attached on the outside, positioned 20 mm from the exit, which serves as the grounded electrode. The vertical gap between the electrodes is 5 mm.

The volumetric flow rate of the He feed gas (purity of 99.999%) for the discharge is regulated by a mass flow controller (Bronkhorst EL-Flow Select F-201CV-2k0-RAD-22-V). The feed gas flows consecutively from the gas bottle through a stainless pipe towards the powered electrode (separated with a small piece of plastic tube for electrical isolation)

into the ambient air. Electrical measurements were obtained by connecting a high-voltage probe (Northstar PVM-5) to the powered electrode to measure voltage that is fed into the plasma and by placing a current probe (Agilent N2863B) over a 1 kΩ resistor to measure the current flow through the grounded electrode. The voltage probe output signal was fed to the pulse delay generator (Stanford Research System DG535), and from here a trigger signal (-Trig) was send to the ICCD camera, after which the camera sends an response signal (-Int). All the electrical signals from the probes, pulse generator and camera were connected to the oscilloscope (LeCroy WaveJet Touch 354).

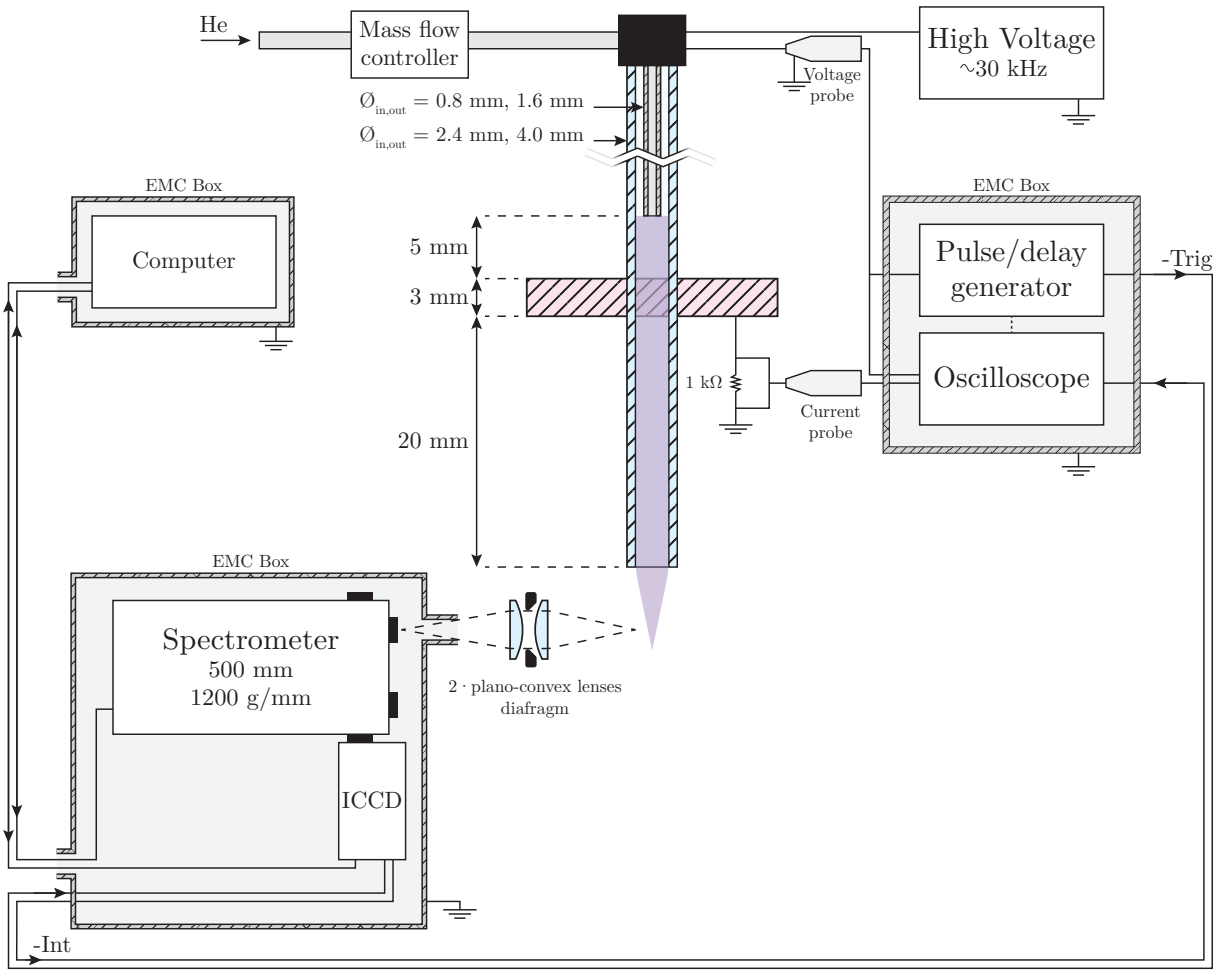

Figure 3.5: Schematic overview of the measurement setup, consisting of the control and measuring electronics and plasma jet. The spectrograph is focused on the vertically downward effluent of the jet.

The jet is placed on a *xyz*-direction linear translation stage to facilitate the precise positioning of the region of interest, along the longitudinal axis of the jet, in the focus of the spectrograph. The emission of the jet is focused on the spectrograph by the direct path optical collecting system (two plano-convex lenses and a diaphragm). The final

component is a computer that controls/acquires the data from the spectrograph, which is also, like the rest of the equipment, protected in an EMC cabinet.

3.3 Experiment settings and measuring procedure

The effect of the plasma jet operation parameters, the applied voltage and volumetric feed gas flow, on the active species in the plasma plume is investigated. Prior to the measurements the plasma is operated for at least 15 minutes to ensure stability of the plasma formation.

The plasma is generated by applying a sinusoidal high voltage at 30 kHz on the helium flow. The applied voltages were in the range from 3.25 kV to 4.00 kV, measured peak-to-peak, to ensure the plasma operates in so called low-power mode as described in literature [30]. In this mode, one ionization wave is generated per period, during the positive half cycle. An increase of the input power should favor the growth of the plume and more emission of light.

The volumetric gas flow rates are between 600 sccm and 1200 sccm. In this flow rate region the Reynolds number has a maximum value of 90; therefore, a laminar flow in the capillary can be expected [31]. However, since the jet is flowing from the capillary exit into the open air, a non-laminar behaviour can appear caused by the shear forces at the interface of the two gas flows with different velocities, which influences the effluent of the jet [32, 33]. In previous work with a comparable plasma source geometry the increase of visible plume length saturated at higher flow rates and for a feed gas flow of 1250 sccm the visible plume length ends around 1.2 cm [18]. Therefore, considering the spatial resolution of the setup, the effluent can be measured for each wavelength interest region without the need of translating the plasma jet configuration in vertical direction during this work.

The electrical characteristics are displayed in the bottom part of figure 3.6. Varying the volumetric gas flow had no noticeable influence on the observed electrical characteristics.

The time base for acquiring the measurements was dependent on the applied voltage. The pulse/delay generator supplied a trigger signal $-t_T$ for 5 µs to the camera when the applied power was at -1 kV with decreasing voltage (see figure 3.6). The internal clock of the camera started the moment t_T was low again. The internal camera delay time, t_D, was set to 9.7 µs. This means that the camera waited t_D before opening the shutter and acquiring an image. The time that the shutter is opened, t_s, *i.e.* how long the camera accumulate for each trigger, was set to 5 µs.

The delay time depends on which part of the jet is measured, since the discharge bullet travels downwards there is no emission at the same time for all positions. The delay increases as the bullet moves further down the jet. The shutter time was set empirically to acquire all the emitted light from the ionization wave. The choice for this voltage level as trigger moment follows from the fact that the steep slope in applied voltage resulted in a good timing and varying the t_D (to "catch" the discharge) and increasing t_s, can be done without exceeding the trigger signal of next period. See table 3.1 for the plasma operation parameters and global spectrograph settings.

Figure 3.7 shows the 5 wavelength regions where spectral measurements are carried out

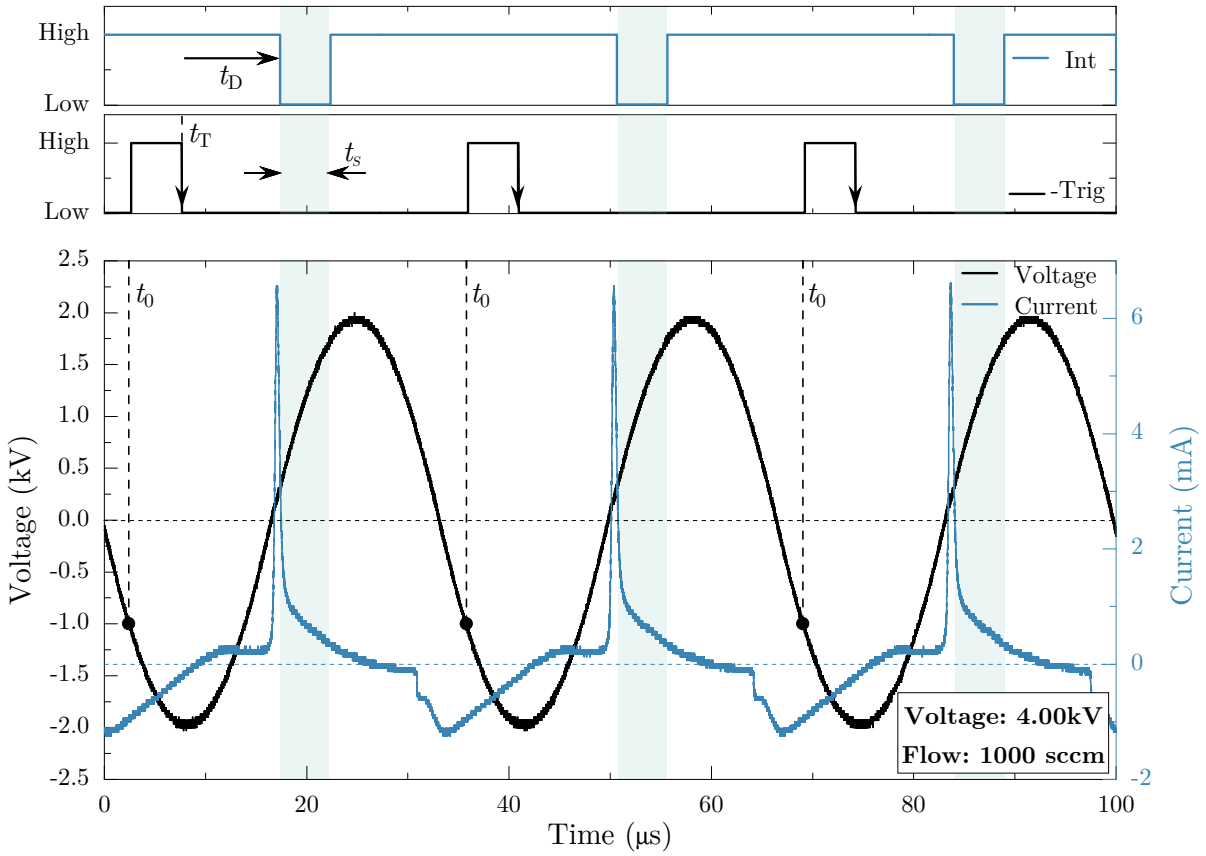

Figure 3.6: The current measured at the grounded electrode during plasma operation when applying the voltage. The time base of the experiment originated from the downward moment of the trigger signal t_T. After some delay time t_D, the shutter of the camera opens during of the shutter time t_s (the shaded area) and accumulates photons. The Int en -Trig signal levels are displayed in time to the discharge and are from the Camera and pulse/delay generator as indicated in figure 3.5.

on the effluent of the jet. Considering that the sensitivity of the spectrograph differs over this broad region (see appendix C.6) and the emission differs in each region, integration times need to be altered for each measurement region to obtain a clear signal of the peak of interest. The integration time is for how long the camera accumulates images for one frame, *i.e.* before the CCD is read out. An appropriate integration time must be chosen this way, without overexposure of the measurement region in the high intensity area (mainly close at the exit of the capillary) but still achieving the signal as well as possible at the end of the effluent. For an integration time of 1 s a frame contains the emission of 33×10^4 plasma bullets. This accumulating of multiple bullets into a single frame is only possible in the low-power mode, in which each discharge event happens at the same moment in the applied voltage period. Finally, multiple frames are stacked together and form one exposure, *i.e.* a raw measurement image. To reduce the noise in

Table 3.1: Overview of the various plasma parameters and settings of the equipment software that apply to each region of interest.

Plasma	He gas flow	600 sccm, 800 sccm, 1000 sccm and 1200 sccm
	Applied voltage	sinusoidal signal at 30 kHz
	(peak to peak)	3.25 kV, 3.50 kV, 3.75 kV and 4.00 kV
Spectrograph	Grating	1200 g/mm
	Entrance slit width	50 µm
Camera	Delay	9.7 µs
	Shutter time	5 µs
	Frames per exposure	5

acquired measurements it is better to accumulate with a longer integration time and less frames per exposure, because with each frame readout noise will be introduced. See table 3.2 for the spectrograph settings in each region. For regions 4 and 5 a cut-off below 590 nm filter is used to exclude higher orders of spectral light, and the MCP gain is set to 1000 V to amplify the signal.

Because the camera was operated in trigger mode, the first picture came (partially) from the buffer. Therefore, before taking a measurement when settings or operation parameters were changed, a dummy measurements was executed to clean the buffer.

Directly after a measurement is acquired, a background image is taken which will be subtracted from the measurement in the post-processing. A background/dark signal measurement is temperature dependent, and it is the representation of the spectral environment without the plasma. To acquire the background measurement an exposure is taken without a change of settings, only the light from the plasma is blocked. The blockade is located between the plasma source and the first lens which the light normally first encountered.

Table 3.2: Overview of the spectrograph settings for each interest regions.

Interest		**Spectrograph**		**Camera**	
		Center λ [nm]	Filter	MCP gain [V]	Integration time [ms]
Region 1	OH	309	✗	825	500
Region 2	N_2	337	✗	825	100
Region 3	N_2^+	391	✗	825	10
Region 4	He	706	✓	1000	1000
Region 5	O	777	✓	1000	20000

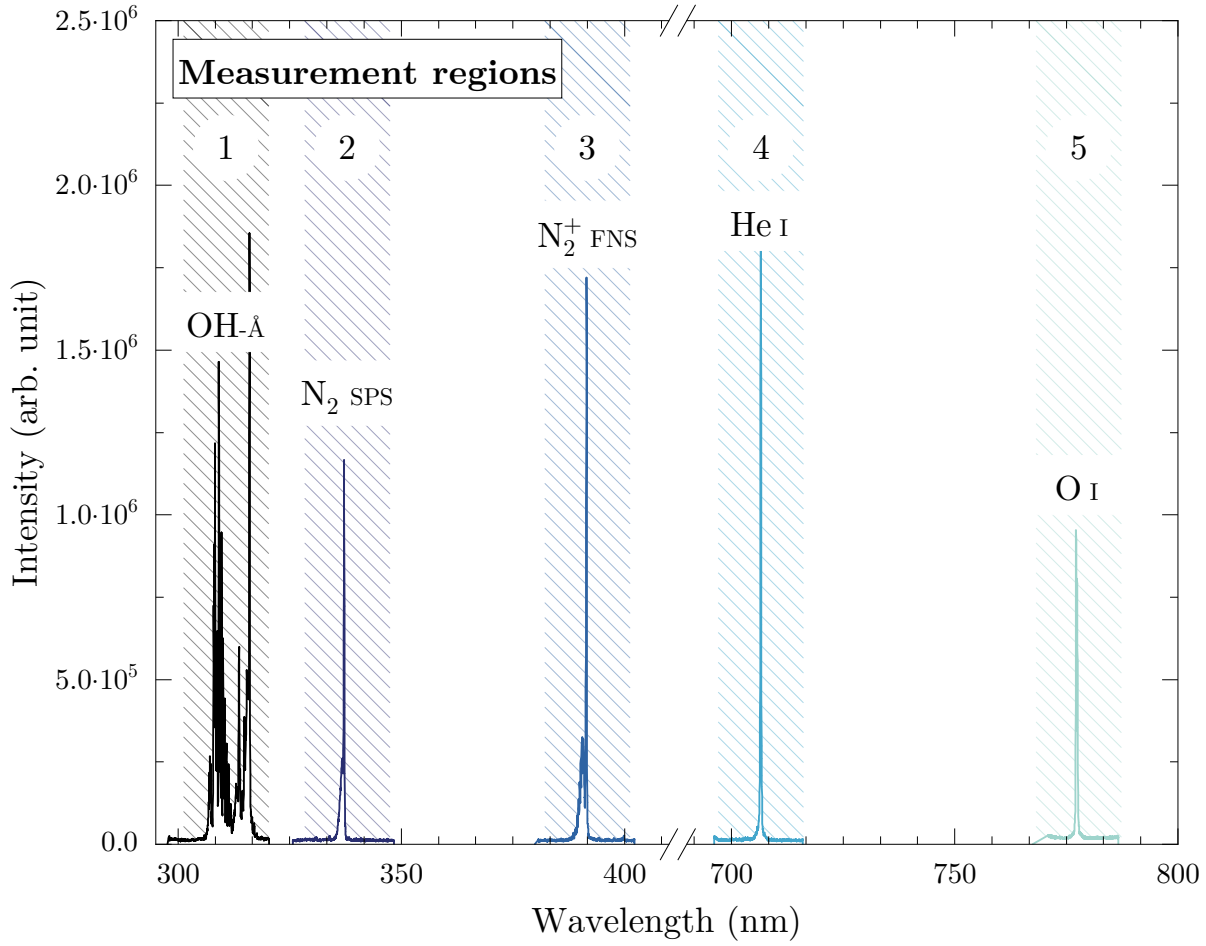

Figure 3.7: The regions where measurements are carried out, with the species of interest annotated. The emission spectra displayed in this graph originate from the first 2 mm of effluent of the plasma jet, operating at He flow rate of 800 sccm and applied voltage of 4.00 kV, and are acquired with the experiment settings from table 3.2.

3.4 Data analysis

The first step to translate the spatially and spectrally resolved raw measurement images (with dimensions of 780 px width and 580 px height) to useful measurement data, was to subtract the dark background images, for each region of interest there is a different background image. After which the intensity values were binned every 27 pixel rows. This results in positional steps along the effluent of the plasma jet of ≈0.49 mm (given the spatial resolution of 54.88 µm/px, see C.4). The x-dimension pixels are corrected for the camera angle orientation (−0.21°, see C.2) per binned row group and are translated into wavelength values using the linear dispersion values (which vary for each region from 34.18 px/nm to 40.32 px/nm, see C.3). The spectra, intensity as function of the wavelength for each position, of the raw measurements are now procured.

Next, the intensity, which is proportional to the number of emitters, and position of the peaks need to be determined. For interference-free lines, the peak height and peak area will give about the same result for intensity analysis. The peak height will generate better results when a line overlaps with other lines, on the other hand, if there are changes due to spectral interference along the spatial axis, *i.e.* a change in line profile, or when the line has self-absorption, the peak area should be used [34]. Therefore, the integral intensity of the line was used as a function coefficient of the fitting profile. The measurements are fitted using the Pseudo-Voigt and Voigt profiles (described in appendix E) with a non-linear least squares method. This non-linear regression analysis results in a fit with a confidence band, and for the function coefficients, *i.e.* the fitting variables such as the area, position and shape of the profile, a confidence interval will be calculated. An example of a resulted fit is shown in figure 3.8.

If the coefficients are bounded and/or one or more of the estimates are at their bounds, those values are regarded as fixed and will not a have confidence interval. This confidence interval is given in an upper and lower value, depending on the confidence level. When the confidence intervals are derived from a large residual degree of freedom ($\gtrapprox 30$), it can be assumed that the z-table of standard normal distribution can be used [35]. As a result the standard deviation follows from the confidence band according to (3.1), and standard propagation of uncertainties can be used to calculate the confidence band in the intensity ratios.

$$\text{Upper/Lower } 95\% = \overline{x} \pm (S \cdot 1.96) \tag{3.1}$$

In this entire work the confidence band with a confidence level of 0.95 is used as uncertainty in the results.

Finally, the emission intensity for each excited molecular and atomic species is normalized (for all flow rates and applied power variation), the resulted intensities along the effluent are shown in the figures of the next chapter.

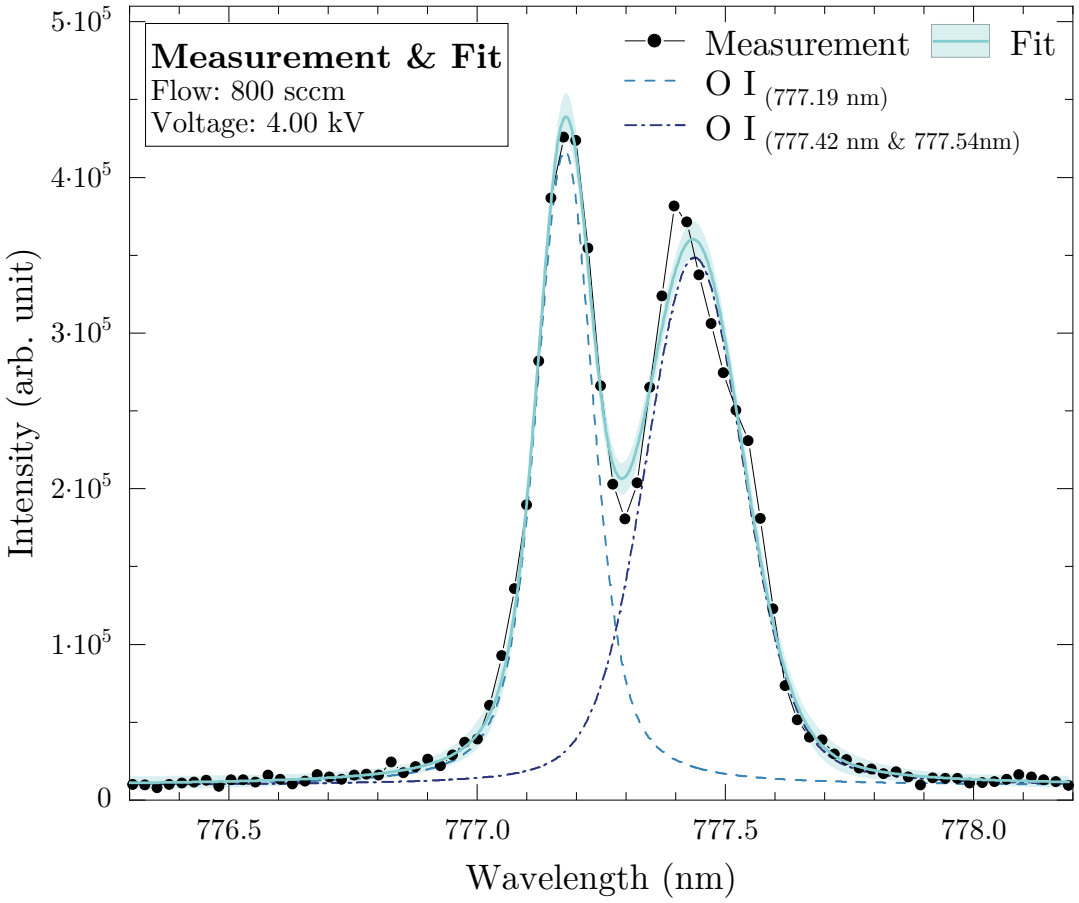

Figure 3.8: Example of a fit of the binned intensity data, including confidence band and deconvolution of the profile. The data is fitted with a two peak Voigt-profile using the Image Processor.

Chapter 4

Results and Discussion

This chapter will present the obtained results for various applied voltages and gas flow rates, as specified in the previous chapter.

4.1 Introduction and plasma plume length

The plasma plume length created by the jet depends mainly on two parameters, the helium gas flow and the applied voltage between the electrodes. Just like for most other plasma jets the plume is electrically driven and independent of the gas flow direction [36]. However, the gas flow ensures an atmosphere in the capillary in which the breakdown requires a lower voltage and allows to form a discharge which could not form in the same conditions without the flow. Outside the capillary the gas flow will form a helium gas channel through the surrounding air, within which the ionization front can propagate. The gas flow determines the gas mixing and therefore influences the gas composition along the effluent [18], which will change the ionization coefficients in the effluent.

The volumetric speed of the gas ($\approx 10\,\mathrm{m\,s^{-1}}$) is several orders of magnitude lower than the propagation velocity of the ionization front (typically in the order of $10^5\,\mathrm{m\,s^{-1}}$). Therefore, in evaluating the discharge processes the gas composition will be considered as static. The energy dissipated in the discharge is an important parameter, as this is the energy that excites and ionizes the particles in the discharge. For higher amplitudes of the applied voltage the ionization wave propagates faster and further than for lower voltages. From previous work the dissipated power ranges from 0.16 W to 0.21 W for operates at 3.25 kV to 4.00 kV (discharge energy per bullet 5.3 µJ and 7 µJ, respectively) [30].

From literature it is known that the plasma jet length increases with the helium flow rate as long it is laminar (a turbulent fast mixing gas decreases the length of the plume). The increase in plume length for higher gas flow rate used in this work could clearly be seen to the naked eye, and is observed with an ICCD in previous experiments on the same plasma source geometry. However, this is not directly apparent from the spectra results displayed in the next section due to the weak dispersed light at the end of the plume. Therefore, to show that the plume length increases for higher flow rates, all the measured spectra (region 1 till 5) for a given gas flow are combined. This light emission of the plume

is then cumulated along the plume length and normalized at the total measured intensity, see figure 4.1. This accumulated intensity profile along the plume shows that the end of the ionization front is further away from the capillary exit for higher flow rates, with 99 % of the total light intensity taken as the end of the plume. Furthermore, it shows that for the higher flow rates the plume is still extending further away than shown in the figure, since the cumulated intensity has not yet reached a plateau at the end of the measured plume length.

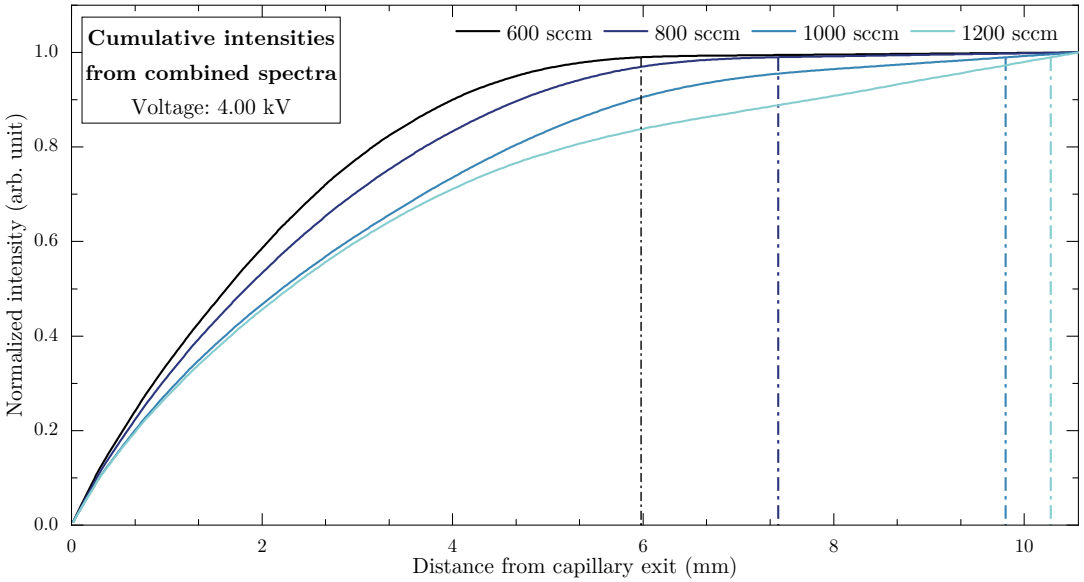

Figure 4.1: The normalized cumulative intensities from the combined spectra as function of the distance from the capillary exit, for various volumetric gas flow rates. The vertical lines are drawn at 99 % of the total intensity, indicating the estimated end of the plasma plume.

As mentioned before, varying the volumetric gas flow rate had no noticeable influence on the observed electrical characteristics during plasma operation. Because generally the displacement current is determined in absence of the gas flow; therefore, the current coupled to the plasma is independent of the gas flow rate. Since the length of the plume is dependent on the flow rate, this indicates that the energy is mainly inserted in the discharge inside the capillary, while the ionization front loses this energy during propagation outside the nozzle. This means that for the same input power, with higher flow rates, the energy dissipated per plasma plume length is lower. The energy losses in the plasma are due to two main mechanism: elastic collisions between electrons and heavy particles, which will result in heating of the gas, and inelastic electron collisions. Depending on the energy of the inelastic collision, the heavy particles will be excited and ionized or the reaction will cause the dissociation of molecules. The excitation and ionization lead to light emission. In the next section the influence of the plasma operating parameters on the excited molecular and atomic species, produced in the discharge along the jet effluent, will be discussed.

4.2 Spectroscopic measurements

Since the plasma jet propagates along a helium channel in the ambient air, oxygen and nitrogen species diffuse into the flow. The observed lines in the measurement regions were identified using [37, 38] for the atomic lines and [39] for the molecular bands.

The examined emission line intensities in the measurement regions 1 to 5: originate from the OH radical at 309.15 nm from $OH(A^2\Sigma_+\text{-}X^2\Pi)(0\rightarrow0)$ in the Ångström system, the nitrogen molecule at 337.18 nm from $N_2(C^3\Pi_u\text{-}B^3\Pi_g)(0\rightarrow0)$ in the second positive system, the nitrogen ion at 391.49 nm from $N_2^+(B^2\Sigma_u^+\text{-}X^2\Sigma_g^+)(0\rightarrow0)$ in the first negative system, the atomic helium at 706.54 nm from $He(3s^3S_1 \rightarrow 2p^3P_{1,2}^o)$ and atomic oxygen at 777.17 nm from $O(3p^5P_3 \rightarrow 3s^5S_2^o)$, respectively.

4.2.1 Optical emission intensities

The emission intensities of the particles along the plasma effluent for all the operating conditions are displayed in figures 4.2 to 4.6. The emission intensities in each figure (composed out of four graphs corresponding to the four different gas flow rates) are normalized. Position 0 mm is the beginning of the plume, starting at the exit of the capillary.

To include all the electron impact electronic-vibrational excitation reactions of the water-nitrogen-oxygen-helium mixture in the discharge scheme will be excessive. Because for the greater part states of particles are short-lived with respect to the involved observed transitions and population collision, only states sufficiently stable are considered. A summary of the relevant production pathways which are common in DBD plasmas at atmospheric pressure, to populate the involved energy states, is listed in table 4.1 at the end of this section.

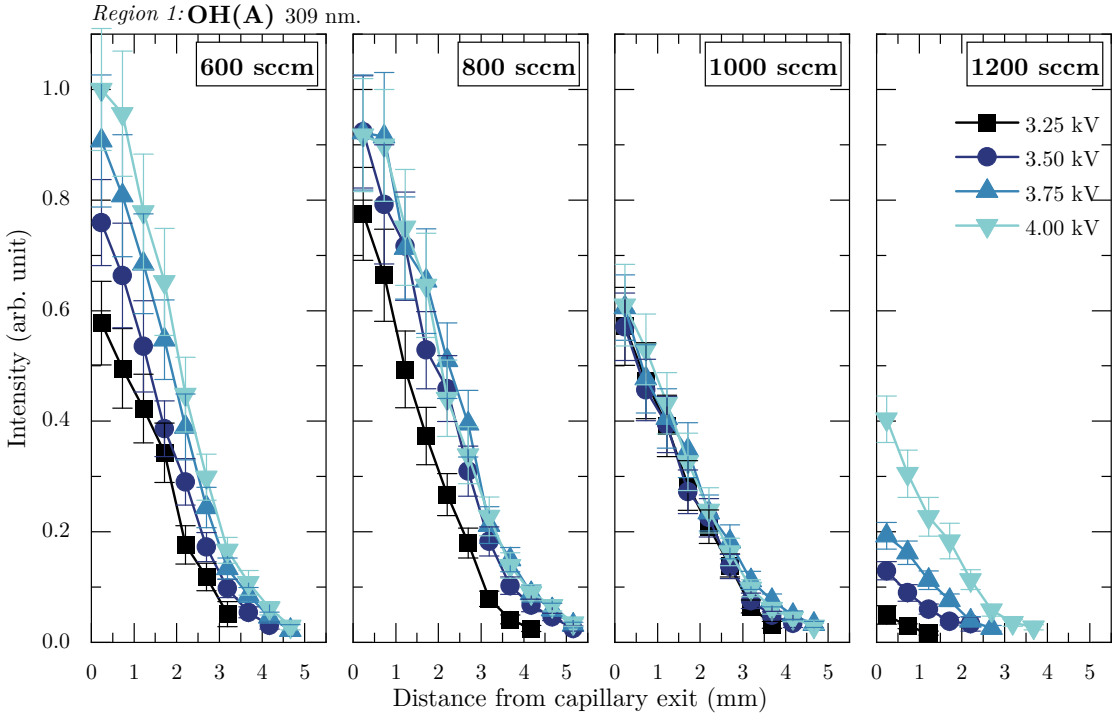

Figure 4.2: Intensities of the 309.15 nm emission line from the OH $(A^2\Sigma_+\text{-}X^2\Pi)(0\rightarrow0)$ transition, for all plasma operating parameters.

Figure 4.2 shows the OH emission line of the Ångström system, corresponding to the transition from the upper level $A^2\Sigma_+$ to the lower level $X^2\Pi$. With the increase of supplied energy the emission is observed to be higher for each flow rate, with the highest intensities at the lowest flow rate. For all operating parameters the emission intensities decrease monotonically along the plume length. Notable is that the intensity for the lowest and highest gas flow rate is the most influenced by the supplied power.

The hydroxyl radial OH is formed from the dissociation of water molecules, which can be introduced in the jet from the surrounding air or as impurity in the feed gas (*e.g.* water adsorbed on the inner surface of the helium line and the pyrex capillary). The fact that the emission is present directly from the nozzle exit indicates that there is likely water vapor in the helium flow in the capillary. The lower OH emission for higher gas flow rates suggests that the majority of water originates from the ambient air. Higher gas flow rates have less admixture of ambient air into the helium channel; therefore, a lower level of entrained air means less water vapor in the plume, which results in a lower OH production.

There are various mechanisms to produce the hydroxyl radical in atmospheric pressure plasmas. The formation of OH(A) comes through a direct dissociative electron excitation of water (R1) or dissociative attachment (R2) of the water molecules, with a threshold energy of 9.1 eV. Excitation of the OH(X) ground state, which is about 4 eV, can be electronic induced (R3) or produced by metastable reactions. The metastable $N_2(A)$

molecule has an internal energy of approximately 6.17 eV, although that is not enough energy to produce OH(A) from H_2O directly, it can produce OH(A) from the ground state (R4). However, due to large energy excess of the helium metastable state ($2s^3S_1$) (19.8 eV) in comparison with the ionization energy of water (12.6 eV), the metastable reaction with H_2O will lead to the ionization of the water molecule rather than to the production of OH.

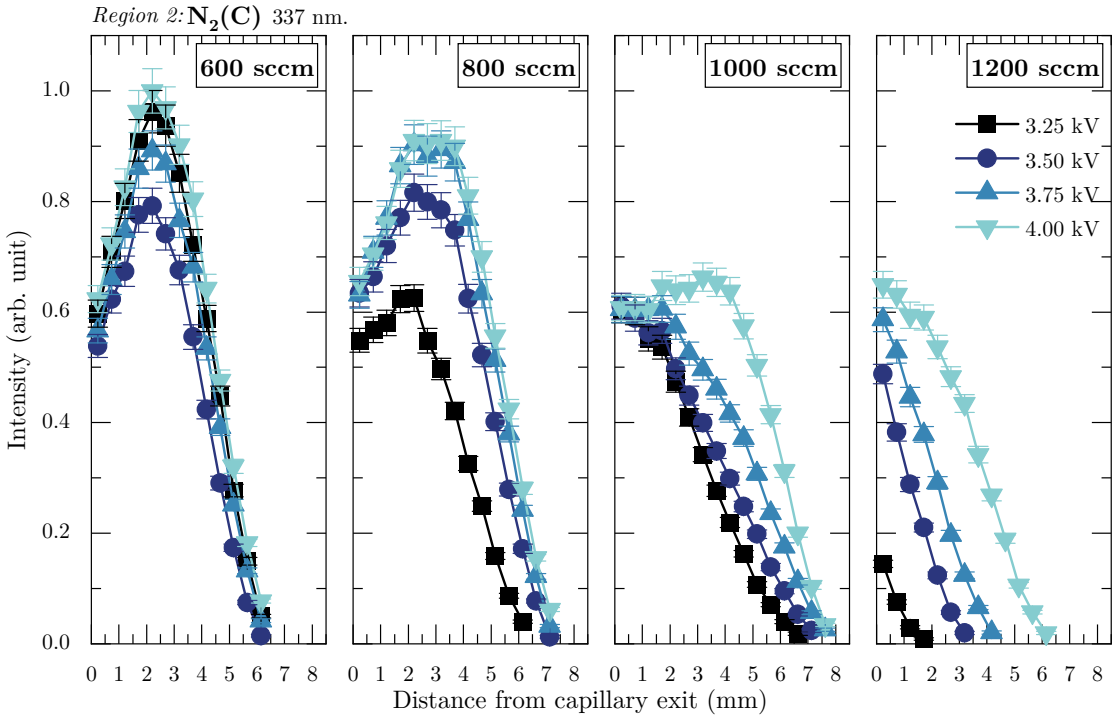

Figure 4.3: Intensities of the 337.18 nm emission line from the N_2 ($C^3\Pi_u$-$B^3\Pi_g$)(0→0) transition, for all plasma operating parameters.

The emission intensity for the 337 nm nitrogen SPS spectral line is shown in figure 4.3. At the capillary exit the emission intensity is almost identical for all operating parameters and at the lowest flow rate, the applied power appears to have no effect on the emission, contrary to the higher flow rates. The emission intensity profile behaves differently compared to the other observed species. For all plasma operating regimes, except for low voltages at high flow rate, the emission intensities from nitrogen have the same level at the exit of the capillary. The maximum emission is not directly at the capillary exit but a few millimeters in front of the nozzle, after which the light emission decreases monotonically at larger distances in a similar way as found for other species. It can be observed that the optimum in optical emission is displaced further away from the nozzle exit at higher gas flow rates. This optimum is caused by an optimum in both nitrogen density and plasma state (electron density and temperature). As for higher flow rates, *i.e.* longer plume lengthes, a given level of air admixture into the plume, caused by the diffusion of ambient nitrogen into the effluent, is further away from the nozzle.

However, since the excitation of nitrogen becomes less likely with increasing distance from the nozzle, an optimum will be reached and despite a still increasing nitrogen density the emission will decrease for larger distances.

The $N_2(C)$ excited molecular state can be populated by a number of processes, it can be created by electron-impact excitation directly from the electronic ground state (R7) with a threshold energy of 11.03 eV or by stepwise excitation trough the vibrationally excited $N_2(A)$ state (R8). It can also be produced by nitrogen reactions with excited helium atoms or via energy pooling from the metastable $N_2(A)$ state (R9), the later becomes more dominant further along the plume as the electron temperature drops. To be certain on the main production pathways time resolved OES and modelling should be carried out.

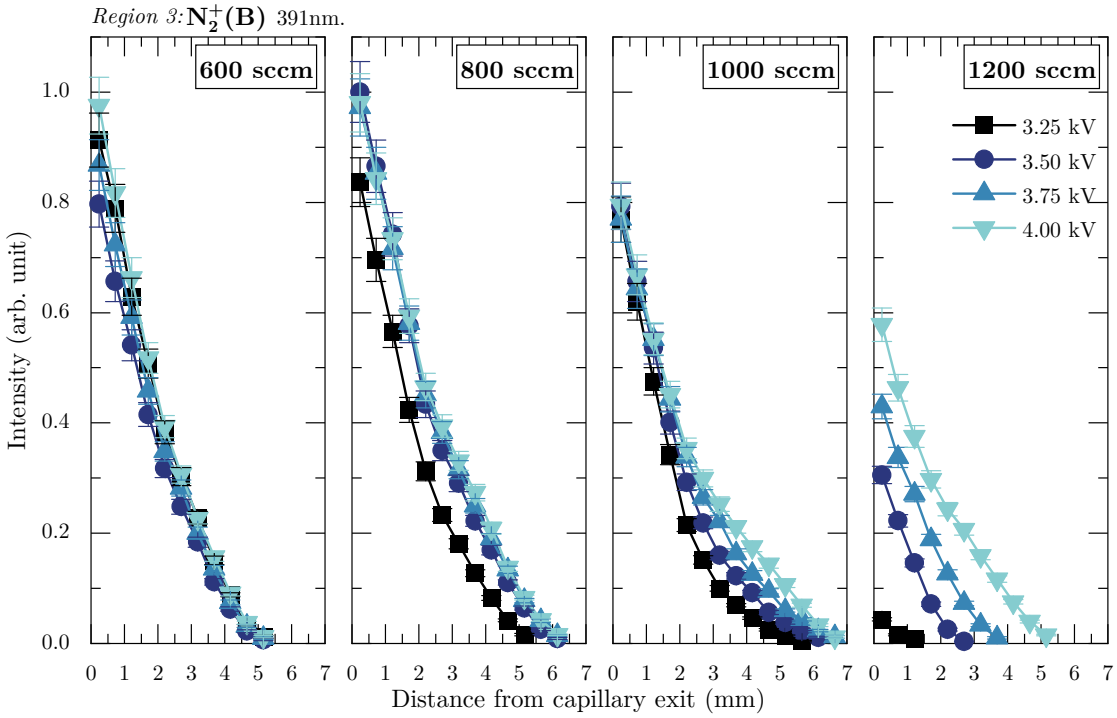

Figure 4.4: Intensities of the 391.49 nm emission line from the N_2^+ ($B^2\Sigma_u^+$-$X^2\Sigma_g^+$)(0→0) transition, for all plasma operating parameters.

Figure 4.4 shows the 391 nm emission intensities from the FNS of the nitrogen ion. The maximum light emission is located at the beginning of the plume, probably caused by an optimum of the ionization of the N_2 molecules already present in this part of the helium jet. This process is driven by direct impact collisions with energetic electrons and by Penning reactions with helium atoms in the excited or metastable state. The profile decreases monotonically further along the plasma plume. The influence of the applied voltage on the emission is noticed for the highest gas flow rate and further downstream in the plasma plume at 1000 sccm.

The $N_2^+(B^2\Sigma_u^+)$ has a high energy level of 18.74 eV and can be produced by electron

impact ionization from the N_2 ground state or metastable state (R11) and (R12). However, when the electron temperature is not high enough, a stepwise production will occur by first producing the ground state ion $N_2^+(X)$ (15.6 eV) and subsequent excitation of this ion to its excited state via (R13). Helium has an important role in the creation of nitrogen ions, due to charge exchange of the ionized helium (R17) followed by direct electron excitation. Or via Penning ionization (R16) with the helium metastable ($2s^3S_1$) formed in (R6) with an energy of 19.8 eV. Therefore, despite that the density of nitrogen is the lowest at the start of the effluent, the Penning effect and charge transfer from helium ions is most pronounced here, resulting in the highest emission.

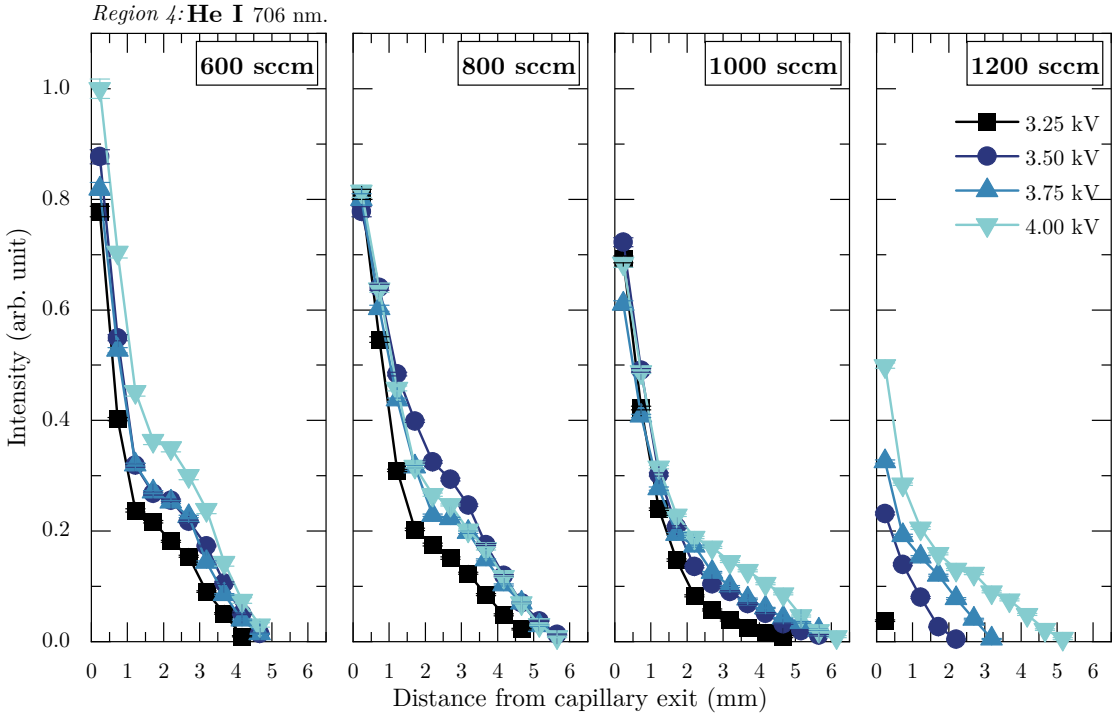

Figure 4.5: Intensities of the 706.54 nm emission line from the He ($3s^3S_1 \rightarrow 2p^3P^o_{1,2}$) transition, for all plasma operating parameters.

The helium line at 706 nm corresponds to a transition from the upper level $3s^3S_1$ to the lower level $2p^3P^o_{1,2}$, the intensity profiles along the plume are shown in figure 4.5. For each gas flow rate the maximum emission intensity is located at the start of the plume and a higher applied power has a positive effect on the light emission. In the ideal case the creation of the discharge in the capillary is independent of the gas flow speed. However, as can been seen at the interface between the end of the capillary and the beginning of the plasma plume, the highest intensity is at the lowest gas flow rate, the jet with the shortest plume, and decreases for faster gas flows. This shows that the discharge at the exit of the capillary is influenced by the rest of the ionized effluent outside the capillary. As the plasma plume propagates into the open air, the helium emission intensity decreases rapidly in the first few millimeters, which may indicate a fast decrease in the electron

temperature. This is due to the collisions with the molecules present in air, which are diffused into the helium channel. These molecules can easily obtain energy from the electrons, because of the low threshold energy for their rotational and vibrational states.

The helium emission intensities for plasma operating conditions of 800 sccm and 3.50 kV are observed not to follow the same trend, i.e. higher applied voltages leading to more emission, as for the other gas flow rates. These measurements were obtained a couple of months later than the other measurements. A change in weather could result in a change in ambient air composition, especially its humidity content. This can cause variations in the plasma properties and possibly lead to this observation as the measurements were not carried out in a controlled atmosphere.

The excited helium state $3s^3S_1$ can be produced through several processes. It can be populated by direct electron excitation from the ground level (R5), step-excitation collisions between excited (metastable) helium atoms and low energy electrons or cascade transitions from upper helium energy levels. However, with an energy level of 22.7 eV this line is dependent on high-energy electrons and indicates the presence of them in the plasma jet.

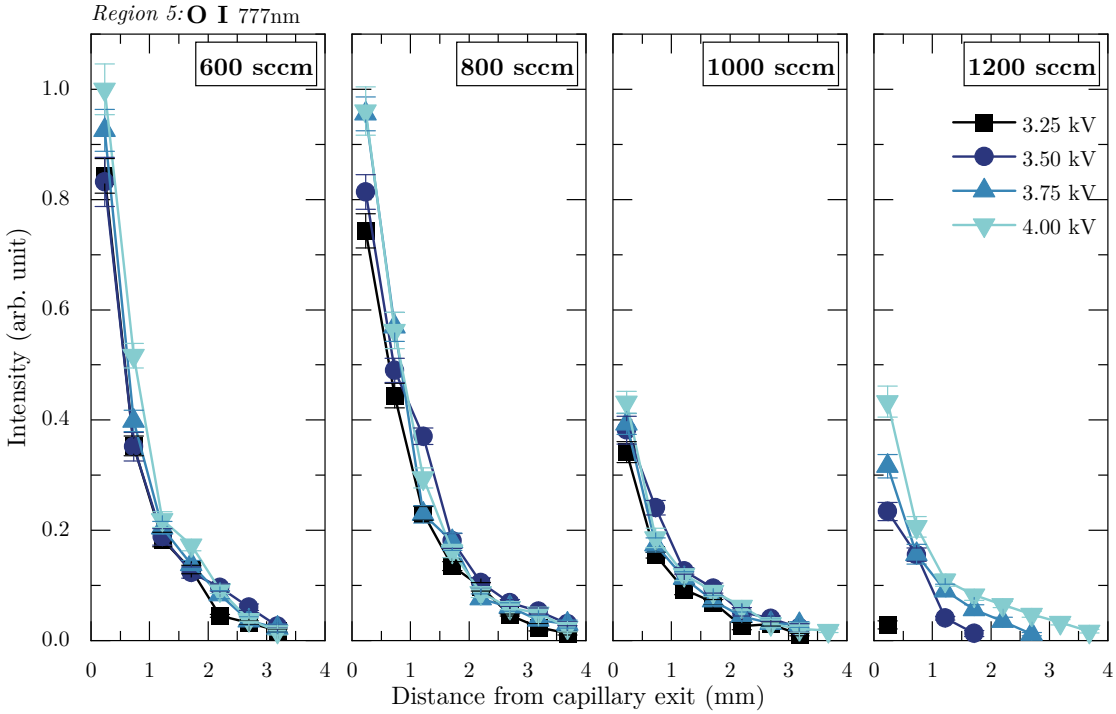

Figure 4.6: Intensities of the 777.17 nm emission line from the O ($3p^5P_3 \rightarrow 3s^5S^o_2$) transition, for all plasma operating parameters.

Figure 4.6 shows the emission intensities of the atomic oxygen line at 777 nm, corresponding to a transition from the upper level $3p^5P_3$ to the lower level $3s^5S^o_2$. The highest emission intensity is at the start of the plasma plume and propagating downstream the excited O state emission is observed to drop. Apart from the highest

gas flow rate, the applied voltage seems to be have negligible influence on the light emission. Noticeable is that the maximum emission for the two lowest flow rates and for the two highest flow rates start at comparable intensities and have the same trend in emission further along the effluent.

The atomic $O(3p^5P_3)$ state is produced from dissociative electron excitation of molecular oxygen that diffuses into the effluent, (R18) and (R19). Or it can be generated through Penning dissociation from excited nitrogen molecules and excited helium atoms, (R10) and (R20). However, the intensities do not show a similar trend as in the $N_2(C)$ emission; therefore, it is unlikely that (R10) is of importance to the oxygen production here.

Table 4.1: Production pathways: excitation, ionisation and dissociation processes by electron-impact and heavy particle collisions.

	Process	**Reference**
(R1)	$H_2O + e^- \rightarrow OH(Y) + H + e^-; Y = X^2\Pi, A^2\Sigma^+$	[40]
(R2)	$H_2O + e^- \rightarrow OH(Y) + H^-; Y = X^2\Pi, A^2\Sigma^+$	[40]
(R3)	$OH(X^2\Pi) + e^- \rightarrow OH(A^2\Sigma^+) + e^-$	[40]
(R4)	$N_2(A^3\Sigma_u^+, v) + OH(X^2\Pi) \rightarrow OH(A^2\Sigma^+) + N_2(X^1\Sigma_g^+)$	[41]
(R5)	$He + e^- \rightarrow He^*(3s^3S_1) + e^-$	[42]
(R6)	$He + e^- \rightarrow He^*(2s^3S_1) + e^-$	[42]
(R7)	$N_2(X^1\Sigma_g^+, v) + e^- \rightarrow N_2(Y, v') + e^-; Y = A^3\Sigma_u^+, C^3\Pi_u$	[43]
(R8)	$N_2(A^3\Sigma_u^+, v) + e^- \rightarrow N_2(C^3\Pi_u, v') + e^-$	[43]
(R9)	$N_2(A^3\Sigma_u^+, v = 0, 1) + N_2(A^3\Sigma_u^+, v = 0, 1) \rightarrow N_2(C^3\Pi_u, v') + N_2(X^1\Sigma_g^+, v'')$	[44]
(R10)	$N_2(C^3\Pi_u, v) + O_2(X^3\Sigma_g^+, v, 0) \rightarrow N_2(X^1\Sigma_g^+, v = 0) + O(^3P) + O(^1S)$	[45]
(R11)	$N_2(X^1\Sigma_g^+, v) + e^- \rightarrow N_2^+(Y, v') + 2e^-;\ Y = X^2\Sigma_g^+, B^2\Sigma_u^+\ ;$	[46]
(R12)	$N_2(A^3\Sigma_u^+, v) + e^- \rightarrow N_2^+(X^2\Sigma_u^+) + 2e^-$	[46]
(R13)	$N_2^+(X^2\Sigma_g^+, v) + e^- \rightarrow N_2^+(B^2\Sigma_u^+) + e^-$	[47]
(R14)	$N_2^+(X^2\Sigma_g^+, v) + N_2(A^3\Sigma_u^+, v) \rightarrow N_2^+(B^2\Sigma_u^+) + N_2(X^1\Sigma_g^+, v)$	[48]
(R15)	$N_2^+(B^2\Sigma_u^+) + e^- \rightarrow N_2(C^3\Pi_u)$	[49]
(R16)	$He^*(2s^3S_1) + N_2(X^1\Sigma_g^+, v) \rightarrow N_2^+(B^2\Sigma_u^+) + He + e^-$	[42]
(R17)	$He^+ + N_2(X^1\Sigma_g^+, v) \rightarrow N_2^+(Y) + He; Y = X^2\Sigma_g^+, B^2\Sigma_u^+$	[50]
(R18)	$O_2(X^3\Sigma_g^-, v) + e^- \rightarrow O_2^{-*} \rightarrow O^-(^2P) + O(3^P)$	[51]
(R19)	$O_2(X^3\Sigma_g^-, v) + e^- \rightarrow O_2^{-*} \rightarrow 2O(3^P) + e^-$	[51]
(R20)	$He^* + O_2 \rightarrow He + O(3p^5P_3) + O$	[52]

4.2.2 Relative emission intensities

The emission intensities are seen to decrease for all considered excited species away from the nozzle exit. This may be related to the decrease in the electron temperature. In order to get more insight from these intensity developments along the plume length, the emissions are compared against the helium emission and the $N_2^+(B)/N_2(C)$ is examined. The relative emission intensities are displayed in figures 4.7 to 4.11.

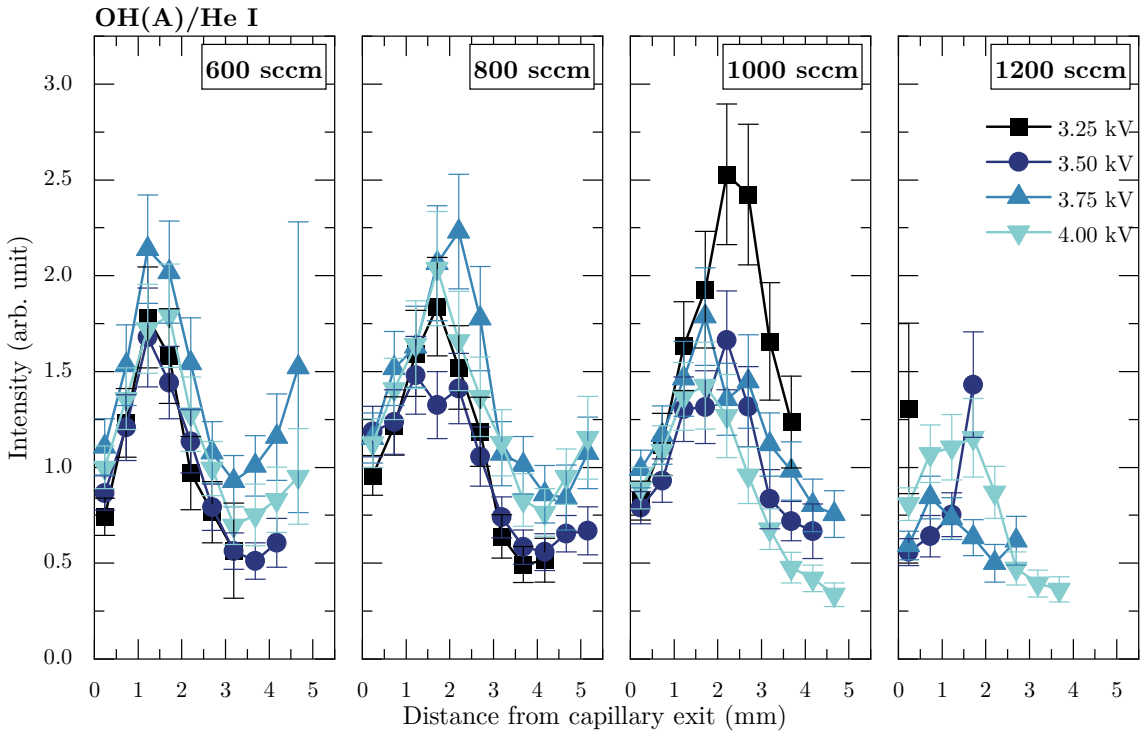

Figure 4.7: Ratio between the normalized emission line intensities of OH(A) and He I.

The relative emission from OH(A)/He featured in figure 4.7 shows an increase for the hydroxyl radical in the first few millimeters, after which it decreases. This maximum can be caused by the sharp decrease in helium emission in the first part of the plasma plume, due to the interaction of electrons with the air molecules.

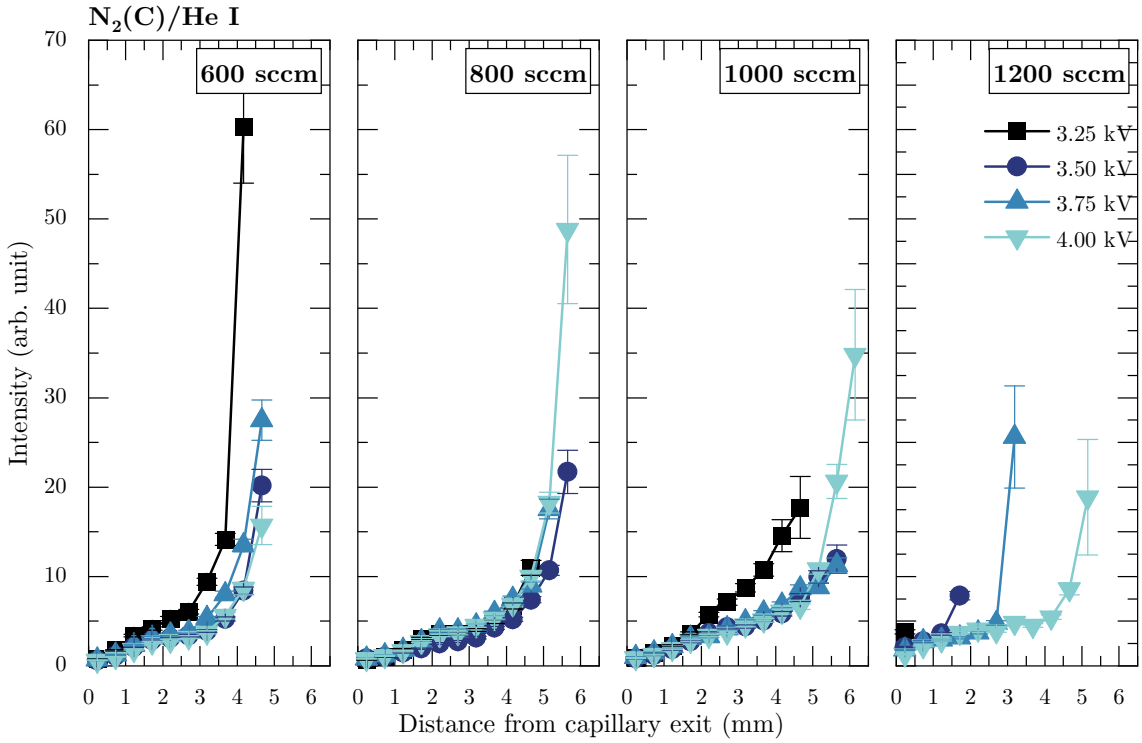

Figure 4.8: Ratio between the normalized emission line intensities of $N_2(C)$ and He I.

Figure 4.8 shows the emission ratio of $N_2(C)$/He. For all operating parameters a continuously rise in ratio at an increasing distance from the nozzle can be observed, with extreme values in the ratio further away from the nozzle exit, as the helium emission decreases towards zero. This trend is probably caused by the increase of nitrogen density further along the plasma plume and by the fact that the upper helium $3s^3S_1$ state depends on highly energetic electrons, whose density is likely to be lower. The $N_2(C)$ can be produced from $N_2(X)$ via electron excitation and by pooling reactions of the metastable $N_2(A)$. Therefore, $N_2(C)$ is probably produced by electron driven reactions close to the nozzle and by pooling reactions further along the plume.

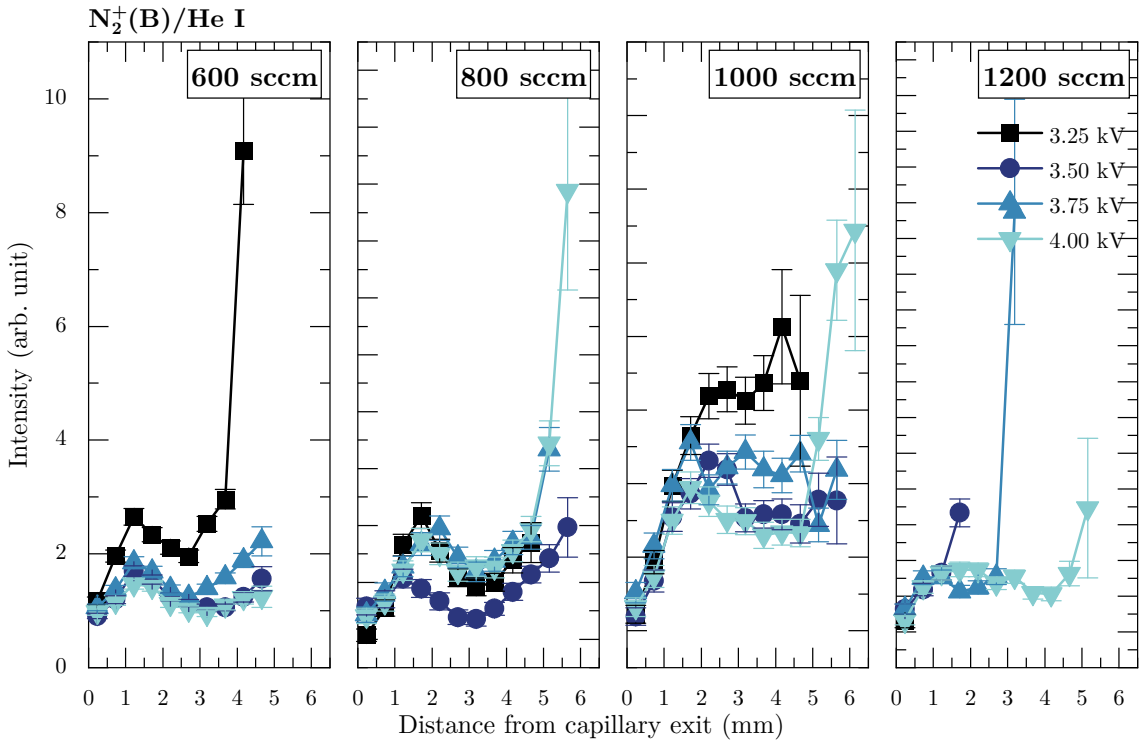

Figure 4.9: Ratio between the normalized emission line intensities of N_2^+(B) and He I.

The relative intensity for N_2^+(B)/He in figure 4.9 shows an increase in the first millimeters in front of the nozzle with subsequently a small drop, but overall this ratio is relatively stable. An exception to this is observed at the end of the plume, where the ratio spikes to extreme values, caused by the helium emission intensity that approaches zero. This behavior is probably due to the changes in the importance of Penning reactions and direct electron impact collisions in the ionization of nitrogen.

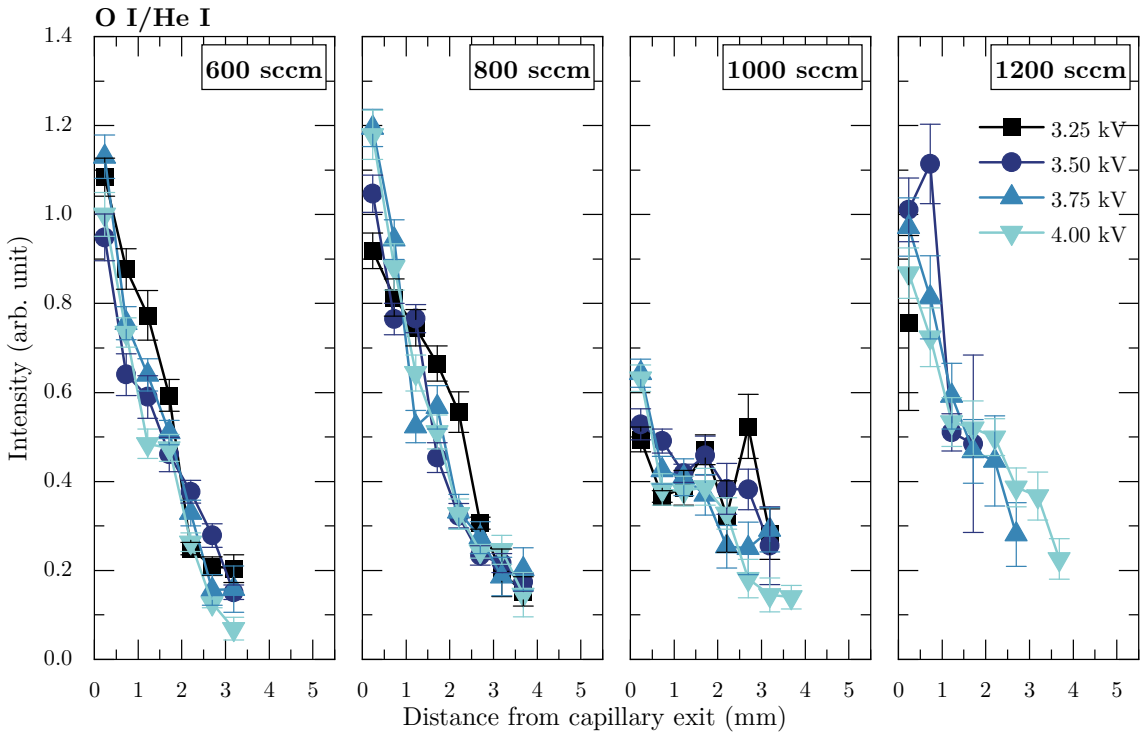

Figure 4.10: Ratio between the normalized emission line intensities of O I and He I.

In figure 4.10, the intensity ratio trends between the atomic oxygen and helium emission lines are observed to drop more or less monotonically along the effluent of the plasma jet for all operating conditions, except at a flow rate of 1000 sccm which is very different, caused by the low emission intensities of atomic O. The input power seems to have little impact on the evolution of the ratio trends, which could be an indication that the processes leading to the excitation of He, mainly direct electron impact, are also the same causing the excitation of O.

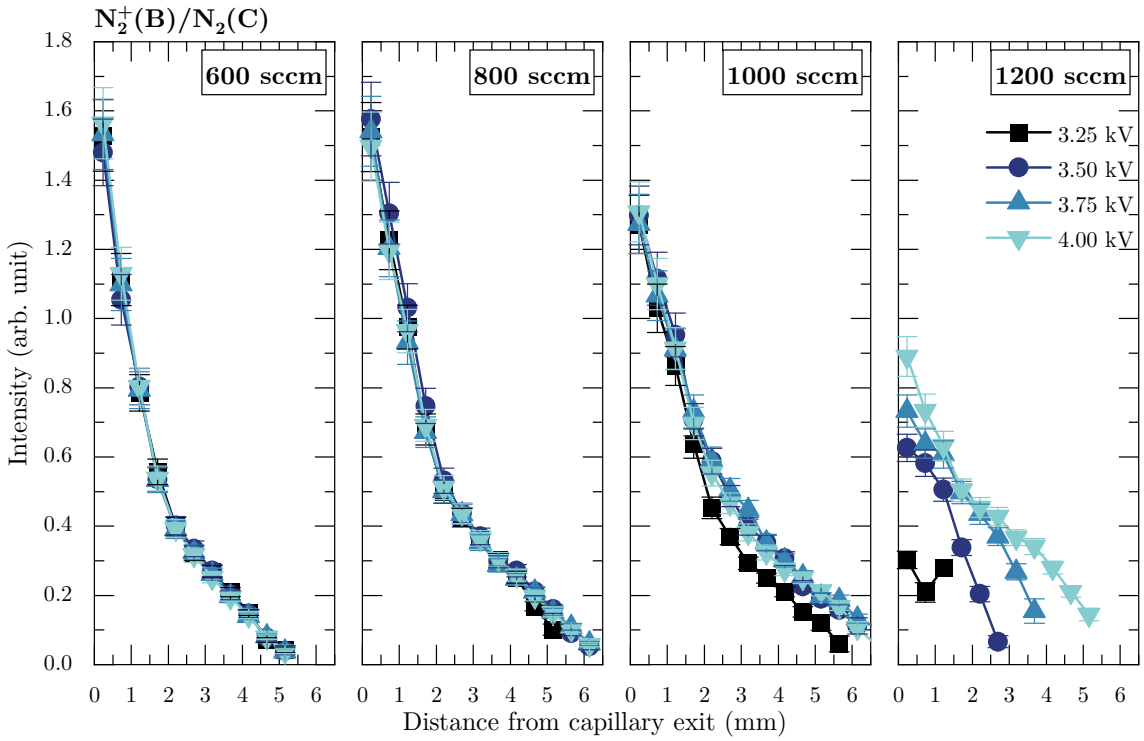

Figure 4.11: Ratio between the normalized emission line intensities of $N_2^+(B)$ and $N_2(C)$.

From the $N_2^+(B)/N_2(C)$ emission ratio, in figure 4.11, an increase of $N_2(C)$ emission is observed downwards in the effluent. Moreover, as the maximum optical emission of the nitrogen molecules was not at the start of the plasma jet, this ratio starts with a value exceeding unity.

This downward trend can possible be appointed to the lower excitation energy of the $N_2(C)$ nitrogen particles. Taking only the direct excitation by electron impact as population path, the nitrogen ions and nitrogen neutrals are excited by different parts of the electron energy distribution function, with the higher energy electrons less present. The $N_2(C)$ state is also produced by pooling reactions and excitation of low-energy electrons which is possible further down the plasma plume. However, this is not true for the population of $N_2^+(B)$, which depends on the highly energetic atomic helium metastable, and as the density of those metastable decrease drastically along the plasma plume so does the density of N_2^+.

Chapter 5

Conclusion and Outlook

The objective of this project was twofold, in the first place to construct an operational working spectrograph setup which could operate in an electromagnetic disruptive environment. Secondly, to examine the influence of the plasma operating parameters on the excited species in the plasma jet effluent. The feed gas flow rate and applied voltage are varied to obtain a better understanding of the dynamics in the plasma jet.

The spectrograph setup was successfully constructed, it has been aligned and calibrated. Two software programs were developed, one to perform measurements with the spectrograph and the other to process the acquired measurement images into spectral data.

The exited species were identified in the plasma plume by OES. Emission at 309 nm of the OH($A^2\Sigma_+$-$X^2\Pi$) system provides evidence for the production of reactive OH radicals in the jet by dissociation of H_2O molecules. Atomic oxygen is observed at 777 nm, produced in the plasma due to O_2 dissociation. The atomic helium ($3s^3S_1$-$2p^3P^o_{1,2}$) line was detected at 706 nm originating from the helium feed gas. Furthermore, the spectrum is dominated by emission lines of excited nitrogen molecules from the second positive system ($C^3\Pi_u$-$B^3\Pi_g$) and from the first negative system of N_2^+, of which the SPS band head at 337 nm and FNS band head at 391 nm is studied in this work.

The evolution of the emission intensity provides information on the production of the active species in the jet, influenced by the operating conditions. The energy required for the propagation of the ionization front is supplied by the high voltage supply. By increasing the applied voltage, the energy deposited in the gas increases, and this raises the electron production rate by ionizing the helium atoms inside the dielectric capillary. As a consequence, the jet propagates further downstream before being quenched by the ambient air, which is diffused into the helium channel. For higher flow rates a given air admixture in the helium channel will be further away from the capillary exit. In the mixing layer between the air and the jet, the interaction between the metastable helium particles and the nitrogen and oxygen molecules promote the generation of electrons and ions during avalanches in front of the ionization wave. This is due to the lower ionization potential of N_2 and O_2 (15.6 eV and 12.1 eV, respectively) compared to helium (24.6 eV). With an increase of the applied voltage, at a fixed helium feed gas flow rate, the species

density downwards along the plasma plume was increased. The overall higher emission intensities of the species for the lowest gas flow rate reflects the higher dissipated energy per plasma plume length, as the total power injected in the plasma was independent of the gas flow rate.

Although the emission intensity and plume length change for the various gas flow rates and applied voltages the relative emission intensities between the different species stay approximately the same in the plasma jet. From the ratio between the He and the other species it can be seen that the emission ratio between N_2^+/He and OH/He are more or less constant along the plume; therefore, no change in production or destruction paths is expected along the plasma jet. However, when the discharge leaves the capillary and starts to propagate in the gas mixing layer, the N_2 SPS emission becomes dominant, and the oxygen emission intensity is observed to drop.

During this work several things were found that could be improved, with the insights gained during this project, for future experiments in this plasma jet topic.

- The holder that keeps the plasma jet in place can be improved. From the start of this work till the end, improvements were carried out to keep the jet in place in front of the optical axis. A new proposed design is shown in figure 5.1, which will ensure a fixed position of the electrodes and providing easier vertical alignment with the entrance slit of the spectrograph. In additions, screens can be used to reduce the influence of the surrounding air flow.

- To remove the dead air space in the capillary, a change of the plasma jet design should be done. By letting the gas flow around the powered electrode, in the capillary, instead of through the electrode.

- To improve the working range and overall performance of the spectrograph setup, the influence of the MCP gain voltage on the measured intensity should be determined. To allow comparing irradiances of different spectral ranges, by mean of a transfer function. The ICCD camera cooling can be improved, to reduce the signal noise. Next to the already present air cooling, cooling with an peltier element on the ICCD chip can be applied. Space has been left for this purpose in the EMC cabinet.

- When building a spectrograph, or any devices with an optical path, it is preferred to build the whole optical setup, including spectrograph and camera, on a plateau. A higher level of the optical axis results in more freedom, to place the to be studied objects. This was something which was not taken into account when designing the EMC cabinet and its optical aperture.

- Improvement in the Image Processor application could be developed. The fitting procedure could be expanded with a few options. The possibility to set different offset along the wavelength range. Improvement in the peak detection mechanism in the spectra, by using 1st or 2nd derivatives of the intensity profile.

- Since in this work the emission intensities of the active species are spatially measured for various plasma conditions, the next step for better understanding the plasma

kinetics involving nitrogen and oxygen molecules entering the helium channel, is to conduct time resolved measurements. This can be supplemented with modelling, e.g. Bolsig+ combined with data on electron density and temperature along the plasma plume. The evolution of the optical emission will provide more specific information on the production paths of the active species. With a broader or more delayed light emission over time, compared to the supplied current peak, a more in-depth insight could be gained into the dominant excitation processes as well as the decay and destruction paths.

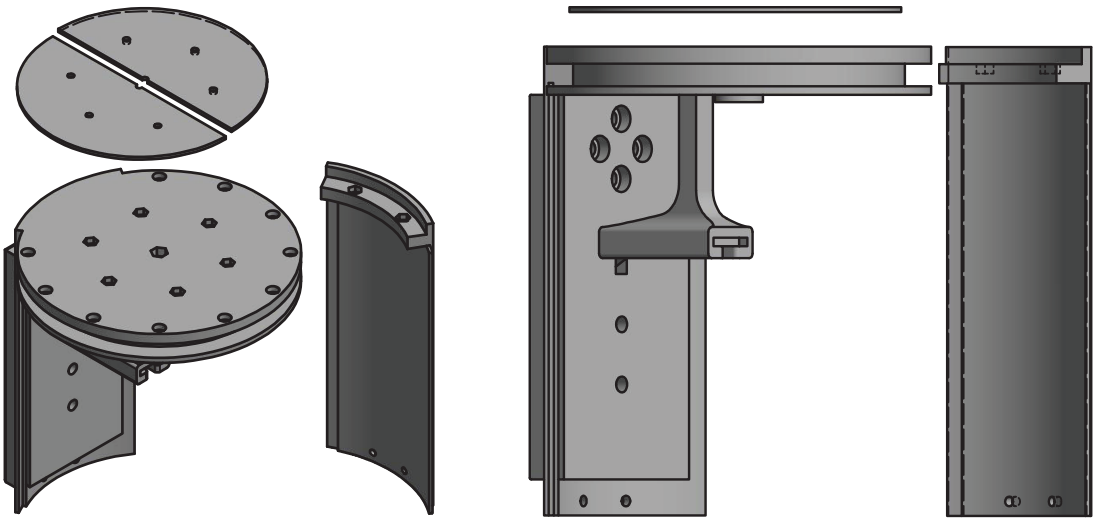

Figure 5.1: Schematic illustration of the improved jet holder.

Bibliography

[1] I. Langmuir, "Oscillations in Ionized Gases," *Proceedings of the National Academy of Sciences*, **vol. 14**, (no. 8), pp. 627–637, 1928. ISSN: 0027-8424. DOI: 10.1073/pnas.14.8.627

[2] M. A. Lieberman and A. J. Lichtenberg, *Principles of Plasma Discharges and Materials Processing*, 2nd ed. Wiley, 2005. ISBN: 0471720011. DOI: 10.1002/0471724254

[3] D. Dobrynin, G. Fridman, G. Friedman, and A. Fridman, "Physical and biological mechanisms of direct plasma interaction with living tissue," *New Journal of Physics*, **vol. 11**, (no. 11), p. 115020, 2009. ISSN: 1367-2630. DOI: 10.1088/1367-2630/11/11/115020

[4] P. Bourke, D. Ziuzina, L. Han, P. Cullen, and B. Gilmore, "Microbiological interactions with cold plasma," *Journal of Applied Microbiology*, **vol. 123**, (no. 2), pp. 308–324, 2017. ISSN: 13645072. DOI: 10.1111/jam.13429

[5] J. Benedikt, V. Raballand, A. Yanguas-Gil, K. Focke, and A. von Keudell, "Thin film deposition by means of atmospheric pressure microplasma jet," *Plasma Physics and Controlled Fusion*, **vol. 49**, (no. 12B), pp. B419–B427, 2007. ISSN: 0741-3335. DOI: 10.1088/0741-3335/49/12B/S39

[6] B. L. Sands, R. J. Leiweke, and B. N. Ganguly, "Spatiotemporally resolved Ar ($1s_5$) metastable measurements in a streamer-like He/Ar atmospheric pressure plasma jet," *Journal of Physics D: Applied Physics*, **vol. 43**, (no. 28), p. 282001, 2010. ISSN: 0022-3727. DOI: 10.1088/0022-3727/43/28/282001

[7] S. Hofmann, A. F. H. van Gessel, T. Verreycken, and P. Bruggeman, "Power dissipation, gas temperatures and electron densities of cold atmospheric pressure helium and argon RF plasma jets," *Plasma Sources Science and Technology*, **vol. 20**, (no. 6), p. 065010, 2011. ISSN: 0963-0252. DOI: 10.1088/0963-0252/20/6/065010

[8] H. R. Griem, *Spectral Line Broadening by Plasmas*. London: Academic Press, Inc., 1974. ISBN: 9780123028501

[9] D. J. Griffiths, *Introduction to Quantum Mechanics*, 2nd ed. Pearson Prentice Hall, 2004. ISBN: 9780131911758

[10] W. Demtröder, *Atoms, molecules and photons: An introduction to atomic-, molecular- and quantum-physics*. Springer, 2006. ISBN: 3540206310. ISSN: 1868-4513. DOI: 10.1007/3-540-32346-5

[11] U. Fantz, "Basics of plasma spectroscopy," *Plasma Sources Science and Technology*, **vol. 15**, (no. 4), pp. S137–S147, 2006. ISSN: 09630252. DOI: 10.1088/0963-0252/15/4/S01

[12] F. L. Pedrotti, L. M. Pedrotti, and L. S. Pedrotti, *Introduction to Optics*, 3rd ed. Pearson, 2006. ISBN: 9780131971332

[13] H.-J. Kunze, *Introduction to Plasma Spectroscopy*, ser. Springer Series on Atomic, Optical, and Plasma Physics. Berlin, Heidelberg: Springer Berlin Heidelberg, 2009, **vol. 56**. ISBN: 978-3-642-02232-6. ISSN: 1615-5653. DOI: 10.1007/978-3-642-02233-3

[14] E. Hecht, *Optics*, 4th ed. Pearson, 2014. ISBN: 9781292021577

[15] X. Huang and Y. L. Yung, "A Common Misunderstanding about the Voigt Line Profile," *Journal of the Atmospheric Sciences*, **vol. 61**, (no. 13), pp. 1630–1632, 2004. ISSN: 0022-4928. DOI: 10.1175/1520-0469(2004)061<1630:ACMATV>2.0.CO;2

[16] N. Konjević, "Plasma broadening and shifting of non-hydrogenic spectral lines: Present status and applications," *Physics Report*, **vol. 316**, (no. 6), pp. 339–401, 1999. ISSN: 03701573. DOI: 10.1016/S0370-1573(98)00132-X

[17] D. Gebhard and W. Behmenburg, "Resonance Broadening and Oscillator strength of the Mercury Absorption Line 1850 Å," *Zeitschrift für Naturforschung A*, **vol. 30**, (no. 4), pp. 445–450, 1975. ISSN: 1865-7109. DOI: 10.1515/zna-1975-0410

[18] A. Sobota, O. Guaitella, G. B. Sretenović, I. B. Krstić, V. V. Kovačević, A. Obrusník, Y. N. Nguyen, L. Zajíčková, B. M. Obradović, and M. M. Kuraica, "Electric field measurements in a kHz-driven He jet—the influence of the gas flow speed," *Plasma Sources Science and Technology*, **vol. 25**, (no. 6), p. 065026, 2016. ISSN: 1361-6595. DOI: 10.1088/0963-0252/25/6/065026

[19] R. L. David, *CRC Handbook of Chemistry and Physics*. CRC Press, 2005. ISBN: 9780849332043

[20] S. Djurović and N. Konjević, "On the use of non-hydrogenic spectral lines for low electron density and high pressure plasma diagnostics," *Plasma Sources Science and Technology*, **vol. 18**, (no. 3), p. 035011, 2009. ISSN: 0963-0252. DOI: 10.1088/0963-0252/18/3/035011

[21] M. Dimitrijevic and S. Sahal-Bréchot, "Stark broadening of neutral helium lines," *Journal of Quantitative Spectroscopy and Radiative Transfer*, **vol. 31**, (no. 4), pp. 301–313, 1984. ISSN: 00224073. DOI: 10.1016/0022-4073(84)90092-X

[22] N. Konjevic and W. L. Wiese, "Experimental Stark widths and shifts for non-hydrogenic spectral lines of ionized atoms," *Journal of Physical and Chemical Reference Data*, **vol. 5**, (no. 2), pp. 259–308, 1976. ISSN: 15297845. DOI: 10.1063/1.555533

[23] S. Hübner, J. S. Sousa, V. Puech, G. M. W. Kroesen, and N. Sadeghi, "Electron properties in an atmospheric helium plasma jet determined by Thomson scattering," *Journal of Physics D: Applied Physics*, **vol. 47**, (no. 43), p. 432001, 2014. ISSN: 0022-3727. DOI: 10.1088/0022-3727/47/43/432001

[24] G. B. Sretenović, O. Guaitella, A. Sobota, I. B. Krstić, V. V. Kovačević, B. M. Obradović, and M. M. Kuraica, "Electric field measurement in the dielectric tube of helium atmospheric pressure plasma jet," *Journal of Applied Physics*, **vol. 121**, (no. 12), p. 123304, 2017. ISSN: 0021-8979. DOI: 10.1063/1.4979310

[25] D. W. Ball, *Field Guide to Spectroscopy*. SPIE, 2006. ISBN: 9780819463524. DOI: 10.1117/3.682726

[26] D. Dussault and P. Hoess, "Noise performance comparison of ICCD with CCD and EMCCD cameras," in *SPIE 5563, Infrared Systems and Photoelectronic Technology*. SPIE, 2004, pp. 195–204. ISBN: 5105273516. ISSN: 0277786X. DOI: 10.1117/12.561839

[27] H. W. Ott, *Noise reduction techniques in electronic systems*, 2nd ed. New York: Wiley, 1988. ISBN: 9780471850687

[28] J. J. Goedbloed, *Elektromagnetische compatibiliteit : analyse en onderdrukking van stoorproblemen*, 1st ed. Deventer: Kluwer Technische Boeken, 1990. ISBN: 9789020122206

[29] J. Colotti, "EMC design fundamentals," in *2006 IEEE Long Island Systems, Applications and Technology Conference, LISAT*, 2006. ISBN: 1424403006. DOI: 10.1109/LISAT.2006.4302648

[30] A. Sobota, O. Guaitella, and A. Rousseau, "The influence of the geometry and electrical characteristics on the formation of the atmospheric pressure plasma jet," *Plasma Sources Science and Technology*, **vol. 23**, (no. 2), p. 025016, 2014. ISSN: 0963-0252. DOI: 10.1088/0963-0252/23/2/025016

[31] D. J. Jin, H. S. Uhm, and G. Cho, "Influence of the gas-flow Reynolds number on a plasma column in a glass tube," *Physics of Plasmas*, **vol. 20**, (no. 8), p. 083513, 2013. ISSN: 1070-664X. DOI: 10.1063/1.4819246

[32] B. van Gessel, R. Brandenburg, and P. Bruggeman, "Electron properties and air mixing in radio frequency driven argon plasma jets at atmospheric pressure," *Applied Physics Letters*, **vol. 103**, (no. 6), p. 064103, 2013. ISSN: 0003-6951. DOI: 10.1063/1.4817936

[33] S. Zhang, A. Sobota, E. M. van Veldhuizen, and P. J. Bruggeman, "Gas flow characteristics of a time modulated APPJ: the effect of gas heating on flow dynamics," *Journal of Physics D: Applied Physics*, **vol. 48**, (no. 1), p. 015203, 2015. ISSN: 0022-3727. DOI: 10.1088/0022-3727/48/1/015203

[34] F. Yueh and J. Singh, "LIBS Application to Off-Gas Measurement," in *Laser-Induced Breakdown Spectroscopy*. Elsevier, 2007, ch. 9, pp. 199–221. ISBN: 9780444517340. DOI: 10.1016/B978-044451734-0.50012-0

[35] H. Ku, "Notes on the use of propagation of error formulas," *Journal of Research of the National Bureau of Standards, Section C: Engineering and Instrumentation*, **vol. 70C**, (no. 4), p. 263, 1966. ISSN: 0022-4316. DOI: 10.6028/jres.070C.025

[36] M. Teschke, J. Kedzierski, E. G. Finantu-Dinu, D. Korzec, and J. Engemann, "High-speed photographs of a dielectric barrier atmospheric pressure plasma jet," *IEEE Transactions on Plasma Science*, **vol. 33**, (no. 2 I), pp. 310–311, 2005. ISSN: 00933813. DOI: 10.1109/TPS.2005.845377

[37] A. Kramida, Y. Ralchenko, J. Reader, and NIST ASD, "Atomic Spectra Database (version 5.7)." [Online]. Available: https//physics.nist.gov/asd Accessed: 2019-10-17

[38] J. E. Sansonetti and W. C. Martin, "Handbook of basic atomic spectroscopic data," *Journal of Physical and Chemical Reference Data*, **vol. 34**, (no. 4), pp. 1559–2259, 2005. ISSN: 00472689. DOI: 10.1063/1.1800011

[39] R. W. B. Pearse and A. G. Gaydon, *The Identification of Molecular Spectra*, 3rd ed. London: Chapman & Hall, 1965. ISBN: 978-0412014604

[40] Y. Itikawa and N. Mason, "Cross Sections for Electron Collisions with Water Molecules," *Journal of Physical and Chemical Reference Data*, **vol. 34**, (no. 1), pp. 1–22, 2005. ISSN: 0047-2689. DOI: 10.1063/1.1799251

[41] G. Dilecce, M. Simek, and S. D. Benedictis, "The $N_2(A^3\Sigma_u^+)$ energy transfer to $OH(A^2\Sigma^+)$ in low-pressure pulsed RF discharges," *Journal of Physics D: Applied Physics*, **vol. 34**, (no. 12), pp. 1799–1806, 2001. ISSN: 0022-3727. DOI: 10.1088/0022-3727/34/12/306

[42] E. Karakas, M. Koklu, and M. Laroussi, "Correlation between helium mole fraction and plasma bullet propagation in low temperature plasma jets," *Journal of Physics D: Applied Physics*, **vol. 43**, (no. 15), p. 155202, 2010. ISSN: 00223727. DOI: 10.1088/0022-3727/43/15/155202

[43] Y. Itikawa and Y. Itikawa, "Cross Sections for Electron Collisions with Nitrogen Molecules Cross Sections for Electron Collisions with Nitrogen Molecules," *Journal of Physical and Chemical Reference Data*, **vol. 31**, (no. 1), pp. 30–53, 2006. ISBN: 00472689. ISSN: 00472689. DOI: 10.1063/1.1937426

[44] L. G. Piper, "State-to-state $N_2(A^3\Sigma_u^+)$ energy-pooling reactions. I. The formation of $N_2(C^3\Pi_u^+)$ and the Herman infrared system," *The Journal of Chemical Physics*, **vol. 88**, (no. 1), pp. 231–239, jan 1988. ISSN: 0021-9606. DOI: 10.1063/1.454649

[45] I. A. Kossyi, A. Y. Kostinsky, A. A. Matveyev, and V. P. Silakov, "Kinetic scheme of the non-equilibrium discharge in nitrogen-oxygen mixtures," *Plasma Sources Science and Technology*, **vol. 1**, (no. 3), pp. 207–220, 1992. ISSN: 0963-0252. DOI: 10.1088/0963-0252/1/3/011

[46] A. V. Kosarim, B. M. Smirnov, M. Capitelli, R. Celiberto, G. Petrella, and A. Laricchiuta, "Ionization of excited nitrogen molecules by electron impact," *Chemical Physics Letters*, **vol. 414**, (no. 1-3), pp. 215–221, 2005. ISSN: 00092614. DOI: 10.1016/j.cplett.2005.08.012

[47] O. Nagy, "$X^2\Sigma_g^+(\nu''=0) \rightarrow B^2\Sigma_u^+(\nu'=0)$ excitation cross-sections of N_2^+ molecular ion by electron impact and the vibrational energy levels of the three target states $N_2^+(X^2\Sigma_g^+, A^2\Pi_u$ and $B^2\Sigma_u^+)$," *Chemical Physics*, **vol. 286**, (no. 1), pp. 109–114, 2003. ISSN: 03010104. DOI: 10.1016/S0301-0104(02)00911-4

[48] G. J. Brussaard, E. Aldea, M. C. Van De Sanden, G. Dinescu, and D. C. Schram, "Evidence for charge exchange between N^+ and $N_2(A^3\Sigma_u^+)$ in a low-temperature nitrogen plasma," *Chemical Physics Letters*, **vol. 290**, (no. 4-6), pp. 379–384, 1998. ISSN: 00092614. DOI: 10.1016/S0009-2614(98)00544-2

[49] J. Lalor, L. Scally, P. J. Cullen, and V. Milosavljević, "Impact of plasma jet geometry on residence times of radical species," *Journal of Vacuum Science & Technology A*, **vol. 36**, (no. 3), p. 03E108, 2018. ISSN: 0734-2101. DOI: 10.1116/1.5022294

[50] N. K. Bibinov, A. A. Fateev, and K. Wiesemann, "On the influence of metastable reactions on rotational temperatures in dielectric barrier discharges in $He - N_2$ mixtures," *Journal of Physics D: Applied Physics*, **vol. 34**, (no. 12), pp. 1819–1826, 2001. ISSN: 00223727. DOI: 10.1088/0022-3727/34/12/309

[51] V. Laporta, R. Celiberto, and J. Tennyson, "Dissociative electron attachment and electron-impact resonant dissociation of vibrationally excited O_2 molecules," *Physical Review A*, **vol. 91**, (no. 1), p. 012701, 2015. ISSN: 1050-2947. DOI: 10.1103/PhysRevA.91.012701

[52] M. Šimek and Z. Bonaventura, "Non-equilibrium kinetics of the ground and excited states in $N_2 - O_2$ under nanosecond discharge conditions: extended scheme and comparison with available experimental observations," *Journal of Physics D: Applied Physics*, **vol. 51**, (no. 50), p. 504004, 2018. ISSN: 0022-3727. DOI: 10.1088/1361-6463/aadcd1

[53] Princeton Instruments, "SpectraPro," 2019. [Online]. Available: https://www.princetoninstruments.com/products/SpectraPro Accessed: 2019-11-15

[54] Stanford Computer Optics Inc., "Image intensified ccd high speed cameras," 2019. [Online]. Available: https://stanfordcomputeroptics.com/technology/iccd-system-overview.html Accessed: 2019-10-17

[55] P. Thompson, D. E. Cox, and J. B. Hastings, "Rietveld refinement of Debye–Scherrer synchrotron X-ray data from Al_2O_3," *Journal of Applied Crystallography*, **vol. 20**, (no. 2), pp. 79–83, 1987. ISSN: 0021-8898. DOI: 10.1107/S0021889887087090

[56] F. W. Olver, D. W. Lozier, R. F. Boisvert, and C. W. Clark, *NIST Handbook of Mathematical Functions*. Cambridge University Press, 2010. ISBN: 9780521140638

[57] H. C. van de Hulst and J. J. M. Reesinck, "Line Breadths and Voigt Profiles." *The Astrophysical Journal*, **vol. 106**, pp. 121–127, 1947. ISSN: 0004-637X. DOI: 10.1086/144944

[58] R. Bracewell, *The Fourier Transform and Its Applications*, 3rd ed. New York: McGraw-Hill, 1978. ISBN: 978-0-07303938-1

[59] G. D. Finn and D. Mugglestone, "Tables of the Line Broadening Function $H(a, \upsilon)$," *Monthly Notices of the Royal Astronomical Society*, **vol. 129**, (no. 2), pp. 221–235, 1965. ISSN: 0035-8711. DOI: 10.1093/mnras/129.2.221

[60] J. Végh, "Alternative form for the pseudo-Voigt peak shape," *Review of Scientific Instruments*, **vol. 76**, (no. 5), p. 056107, 2005. ISSN: 0034-6748. DOI: 10.1063/1.1914783

[61] G. K. Wertheim, M. A. Butler, K. W. West, and D. N. E. Buchanan, "Determination of the Gaussian and Lorentzian content of experimental line shapes," *Review of Scientific Instruments*, **vol. 45**, (no. 11), pp. 1369–1371, 1974. ISSN: 0034-6748. DOI: 10.1063/1.1686503

Appendix A

Documentation main components

A.1 Specifications

The **Acton SpectraPro 2560i** with serial number: *25581480* is a Czerny-Turner spectrometer, with a focus length of 500 mm. It has two entrance and two exit ports, the exit focal plane size is 26 mm wide and 14 mm height. One of the entrance slits has motorized control ranging from 10 µm to 1200 µm. The grating turret has a drive step size of 0.0025 nm and consists of three ruled gratings each with different dimensions, grooves per millimeter and blazing wavelength see below. For more specifications see the website of the producer [53].

- 68 mm × 68 mm, 150 grooves/mm, blazing 500 nm.
- 68 mm × 68 mm, 600 grooves/mm, blazing 500 nm.
- 68 mm × 84 mm, 1200 grooves/mm, blazing 300 nm.

The **4Picos-dig** with serial number *P4979* is an intensified CCD camera with a digital usb connection. The camera has an image sensor size of 14.4 mm × 10.8 mm with 780 pixels in width and 580 pixels height, the CCD pixel size is 8.3 µm × 8.3 µm. The micro channel plate is single stage with a gain of $V_{MCP} = 0$ V to 1000 V and a spectral wavelength range of 165 nm to 820 nm. The camera has a minimum shutter time of 200 ps and a maximum integration time of 80 s. The camera originates from the XX RapidFrame system. More information on the 4Picos-dig or ICCD cameras in general can be found on the website of the producer [54].

A.2 Installation Manual 4Picos-dig

Eindhoven University of Technology
Department of Applied Physics

Installation Manual

4Picos-dig Windows 7 64-Bit Build

Software & Drivers

Hardware: 4 Picos-dig iCCD Camera
Software: 4 Spec E - Drivers

Stanford Computer Optics
http://www.stanfordcomputeroptics.com

Marco de Peuter

This document provides a guide to install the 4Picos-dig iCCD camera from Stanford Computer Optics on a 64-Bit Build operating system.

- Install USB hard-lock driver.
- Install camera drivers 4 Picos-dig.
- Install software 4 Spec E.
- !Important! for 64-Bit build, update the correct .dll file.
- Install help file 4 Spec E support (Optional).

Install USB hard-lock driver

To work with the full version of the 4 Spec E software a USB hard-lock is required.

- Go to directory: `\1.USB_Dongle_Driver`.
- Open file: Sentinel System Driver Installer 7.4.0.msi.
- Do the following steps in succession (see figure A.1).
  - Click "Next", Mark "Accept" + Click "Next", Mark "Complete" + Click "Next", Click "Install" ⇒ Finish.

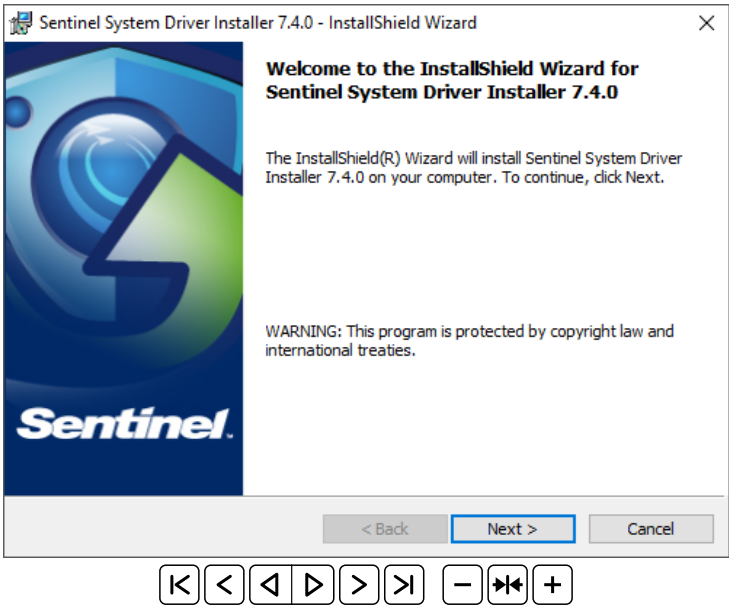

Figure A.1: USB hard-lock driver installation steps[1].

[1] Animation only in digital version.

Install camera drivers 4 Picos-dig

The next step is to install the camera driver.

- Connect the camera to a USB port and turn it on ⇒ "Unknown device" should be detected.

- Do the following steps in succession (see figure A.2).

    1. Go to the device manager, right click on the "Unknown device" and select "Update Driver Software...".
    2. Click "Browse my computer for driver software".
    3. Browse to the directory: `\2.x64bit_USB_Driver`.
    4. Click "Next".
    5. Click "Install the driver software anyway".
    6. Click "Close" ⇒ the camera is now installed as Sample Device → khs-instruments.

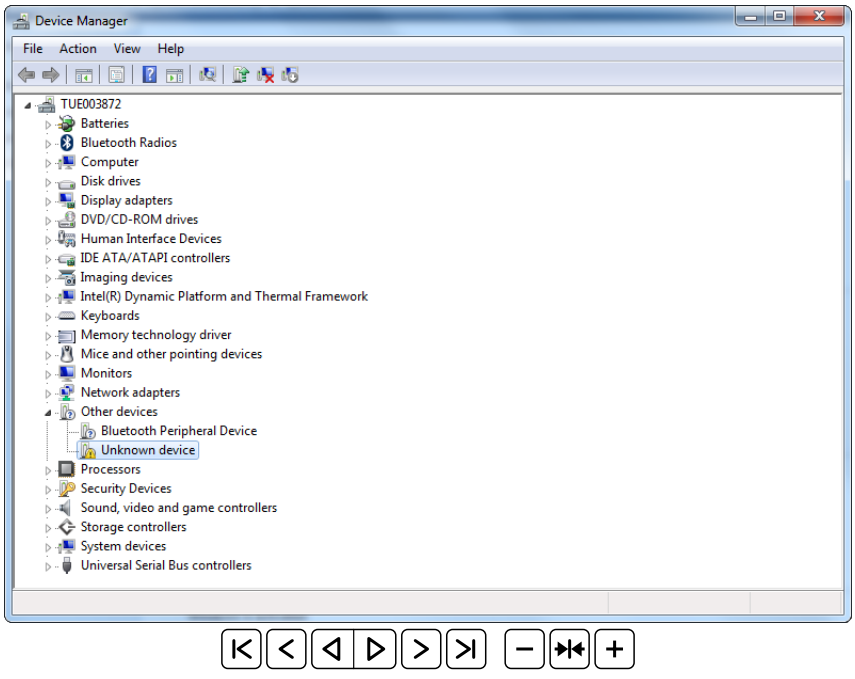

Figure A.2: Camera driver instalation steps[2].

[2]Animation only in digital version.

Install software 4 Spec E

The following step is to install the 4 Spec E software for this camera *i.e.* (4 Picos or 4 Quik E).

- Go to directory: `\3.4Spec_E_USB`.
- Open file: setup.exe.
- Specify destination directory: `C:\4Spec` and click "Start installation".

!Important! - Replace KHSDLL.dll

For the 64-Bit build operating system the KHSDLL.dll file needs to be replaced otherwise no complete signal can be obtained (see figure A.3).

- Copy the KHSDLL.dll file from the driver install directory `\2.x64bit_USB_Driver`.
- Paste and replace in the `C:\Windows\SysWOW64\`[3] directory.

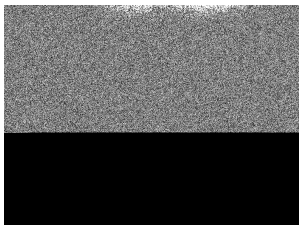

(a) KHSDLL.dll v0.495

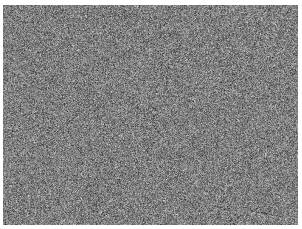

(b) KHSDLL.dll v0.46F

Figure A.3: Output iCCD signal.

(Optional) Install help file 4 Spec E support

To access the 4 Spec E program help menu, Windows needs to access the .hlp-files. From Windows XP this format is by default not supported anymore. To solve this problem, run the following installation program: `\4.Help_File\Windows6.1-KB917607-x64.msu`.

From Windows 10 & Windows Server 2012 or later versions of Windows Server it is not supported at all.

For more information go to:
https://support.microsoft.com/nl-nl/help/917607/error-opening-help-in-windows-based-programs-feature-not-included-or-h

[3]SysWOW64 is an abbreviation for: System Windows 32 Bit on Windows 64 Bit.

Appendix B

Construction setup-parts: Technical drawings

This appendix shows the technical drawings of the components which are mentioned in section 3.1.

B.1 The spacer, adapter- and mounting plate to connect the 4Picos-dig camera with the Acton SP2560i spectrometer.

B.2 The EMC cabinet which encloses the whole spectrograph setup.

B.1 C-mount replacement

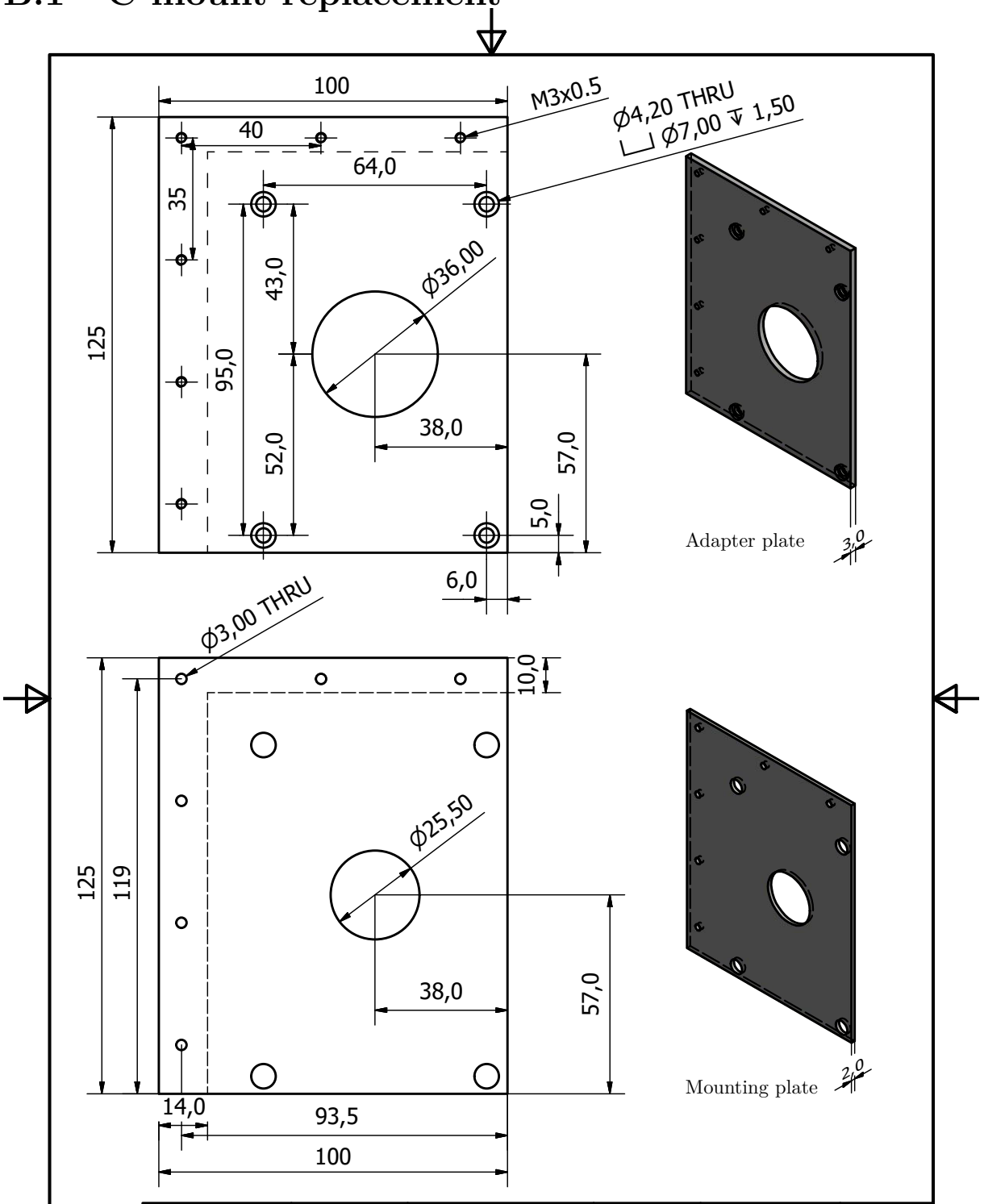

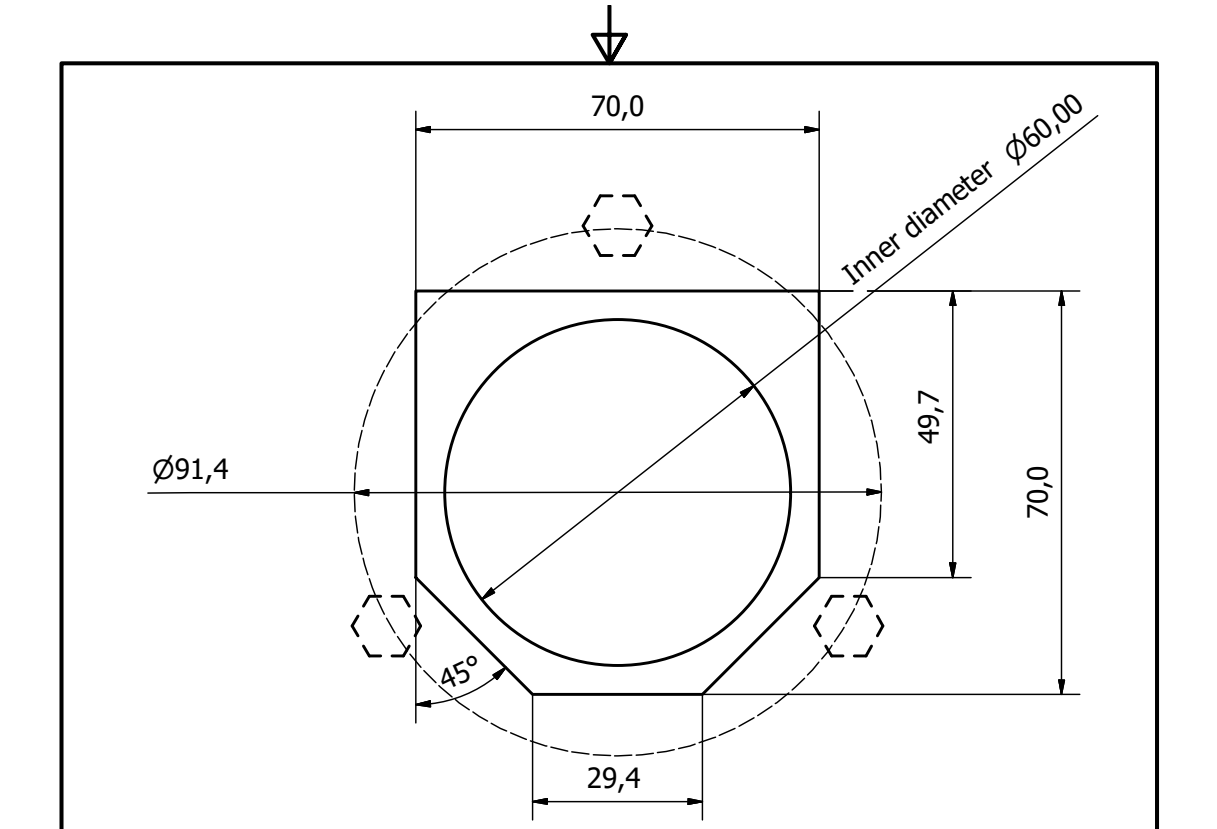

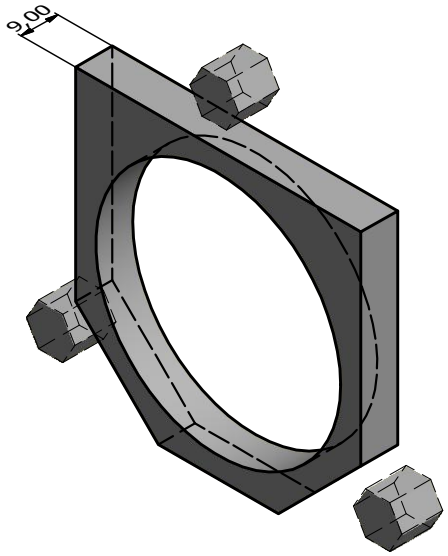

Designed by	Checked by	Approved by	Date		Date	
Marco						

C-mount Spacer	Edition	Sheet
		1 / 1

B.2 EMC cabinet

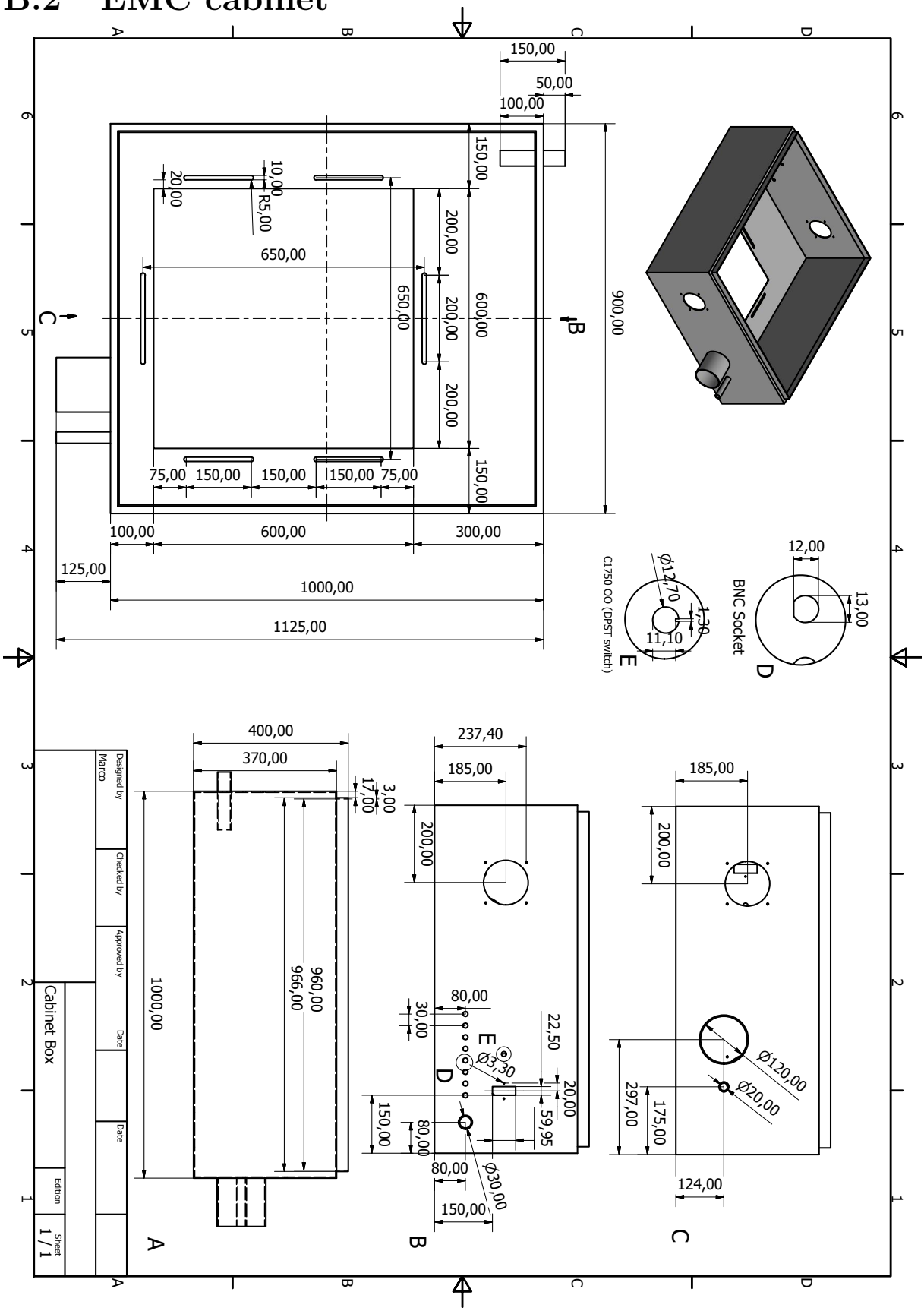

Appendix C

Calibration of the spectrograph setup

Before acquiring images as the raw measurement data, the spectrograph setup needs to be aligned and calibrated on several points. In this chapter the following procedures will be described.

C.1 Positioning the focus plane of the spectrograph.

C.2 Correction of the camera angle orientation.

C.3 Determination of the linear dispersion.

C.4 Determination of the spatial resolution.

C.5 Determination of the instrumental broadening.

C.6 Determination of the spectral response of the spectrograph.

C.1 Focus mirror position of the SP-2560i

To obtain optimum resolution, *i.e.* sharp spectral lines, it is necessary to adjust the focusing mirror of the spectrometer. Due to the connection between the spectrometer and the detector and due to variations in the distance from the mounting flange of the detector to its focal plane, the setup can be out of focus. With the new c-mount adapter plate at the side exit port of the SP-2560i (see B.1) the camera CCD chip of the 4Picos-dig came within the focal plane range. For all three gratings at several wavelengths (0 nm, 404 nm and 585 nm), adjustments to the focusing mirror position were made to obtain the sharpest image (see figure C.1). The following criteria were taken to determine the optimum position.

- The imaged line has the smallest FWHM.
- The imaged line has the highest peak intensity.

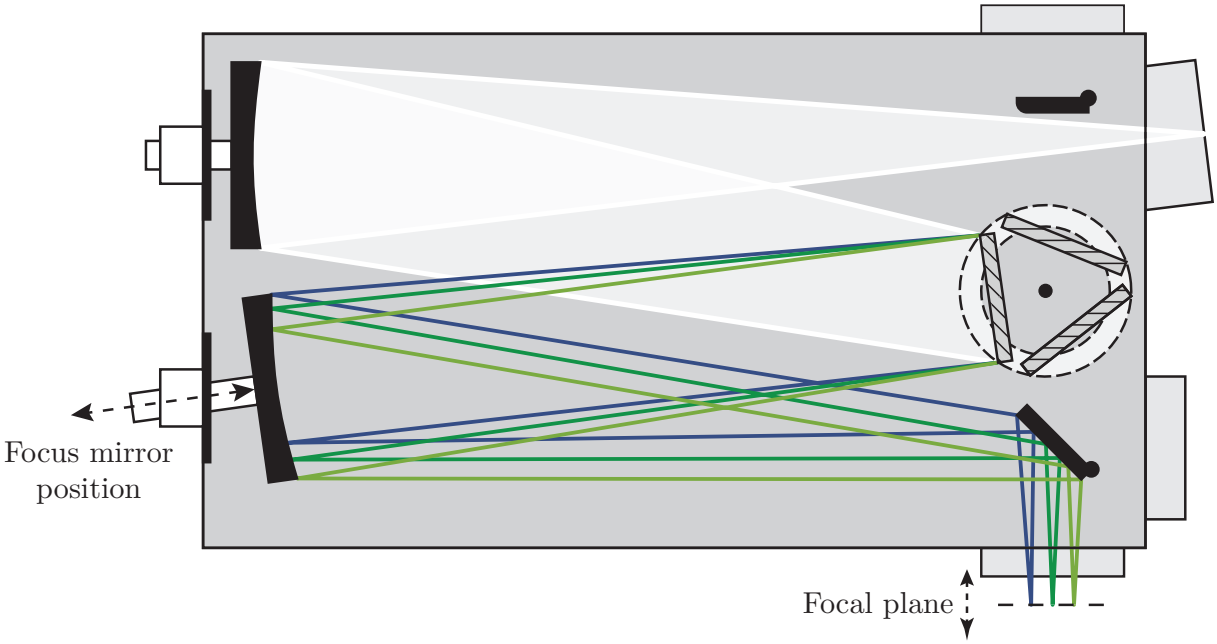

Figure C.1: Schematic drawing of the effect of the focus mirror in the spectrometer on the focal plan.

A calibration lamp was placed directly in front of the spectrograph entrance slit, and the camera settings were set in such a manner that the intensity level was comparable for each case. Thereafter a Gaussian fit was performed on the intensity of the top 200 pixel rows to determine the FWHM and peak intensity value. A selection of the measurements is displayed in figure C.2. As can been seen, for each grating and wavelength there is a slightly different optimum position, probably due to grating position on the turret. However, since the measurements in this work are mainly carried out with the 1200 grooves/mm grating, the focus mirror is placed at the optimum position for this grating at 0.36 µin.

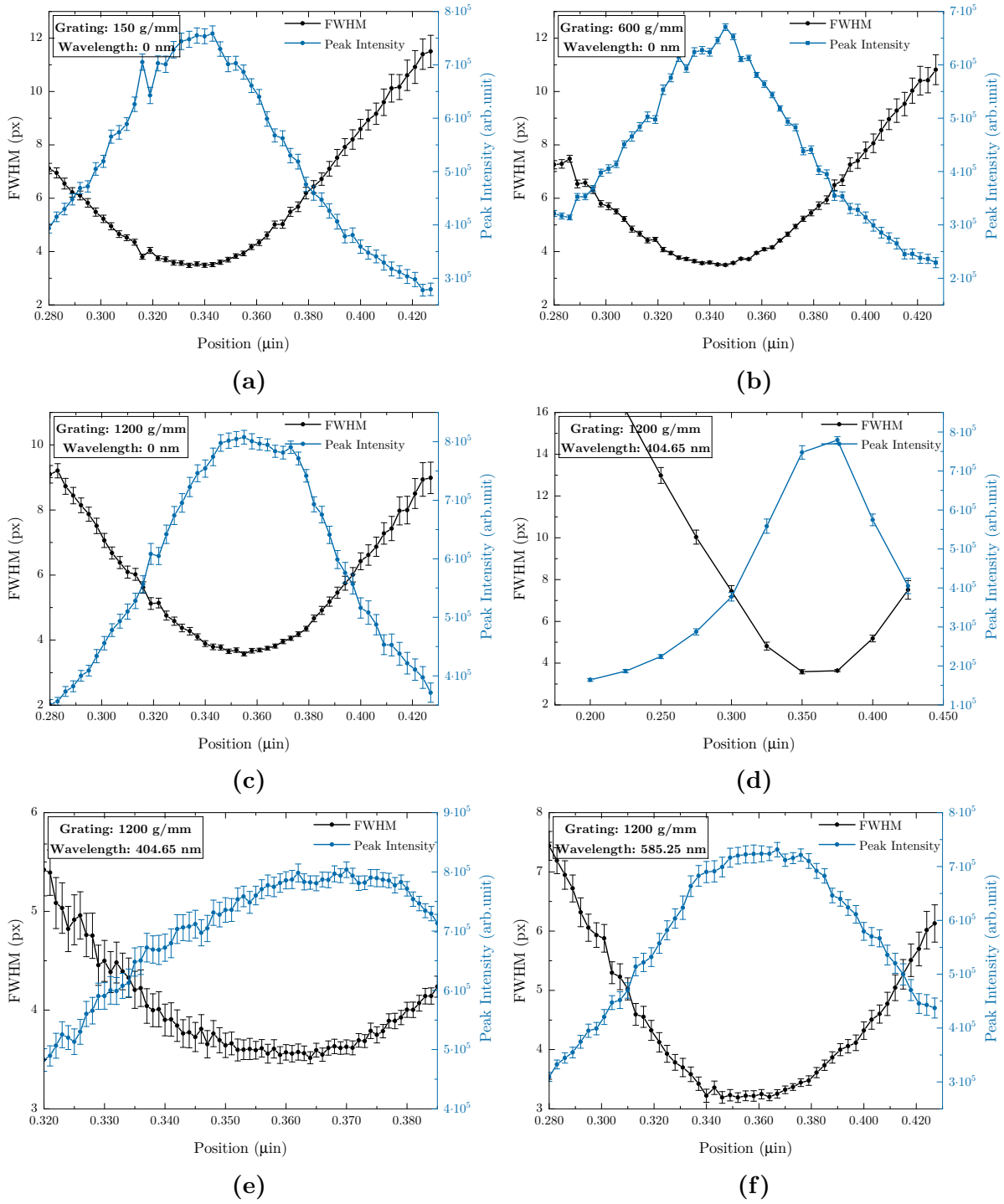

Figure C.2: Change in peak width and intensity due to the change in position of the focussing mirror for various gratings and wavelengths. The values result from a Gaussian fit on binning of the top 200 pixel rows.

C.2 Correction camera orientation

Despite the best effort to mount the camera (this means the CCD) in the same horizontal plane with the spectrograph, a small angle is almost unavoidable. Nonetheless, this rotation needs to be corrected for a correct determination of spectral line positions over the entire vertical direction of the measurement, *i.e.* the spatial direction of the observed object. This is accomplished with a wavelength position shift for each row/binning, see figure C.3.

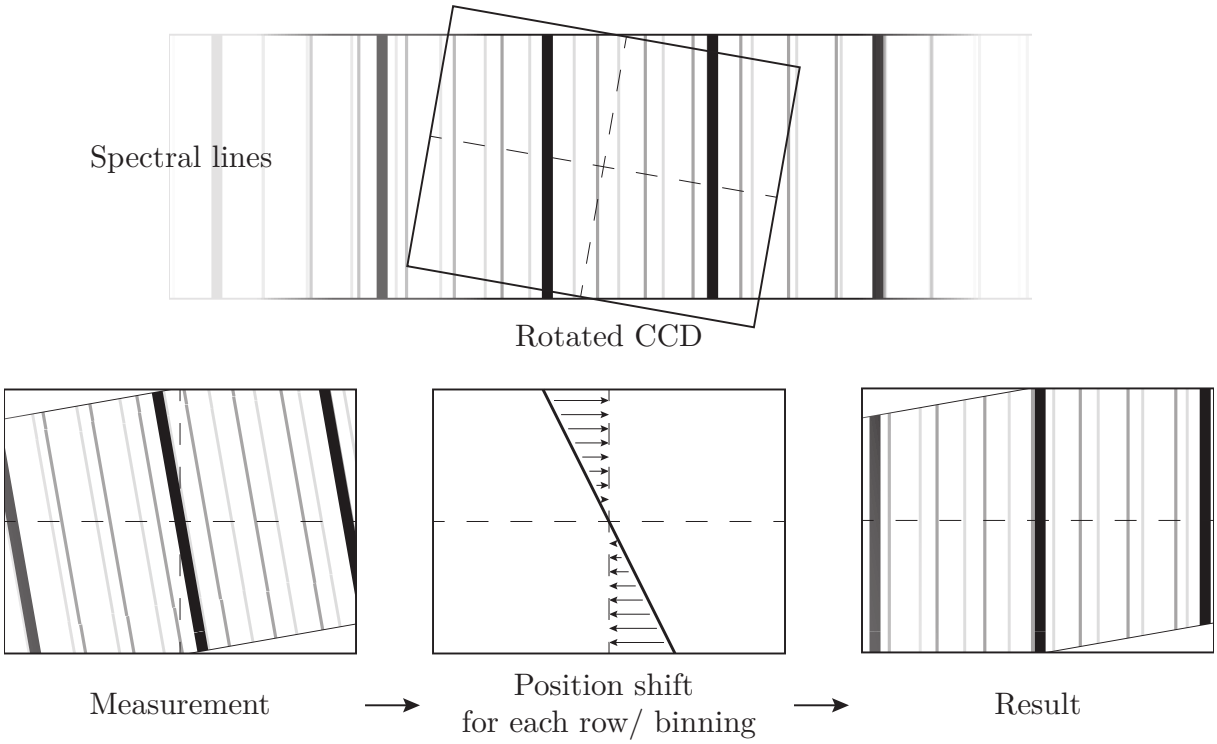

Figure C.3: Visual representations of the correction procedure on the observed spectral lines on the rotated ccd.

To determine the rotation angle of the CCD relative to the spectrograph a mercury calibration lamp was placed at the entrance slit (slit width of 50 µm). The spectrograph was set in such a way that a spectral peak of 435.8 nm was displayed at the center pixel of the CCD. To determine precisely the peak position a Gaussian fit was applied to the measured data which was binned every 10 pixel rows, as long as the intensity in each binning was constant. The rotation angle $-0.21°$ of the CCD was calculated from the change in peak position. Figure C.4 shows the measured peak position and the corrected position in pixel space.

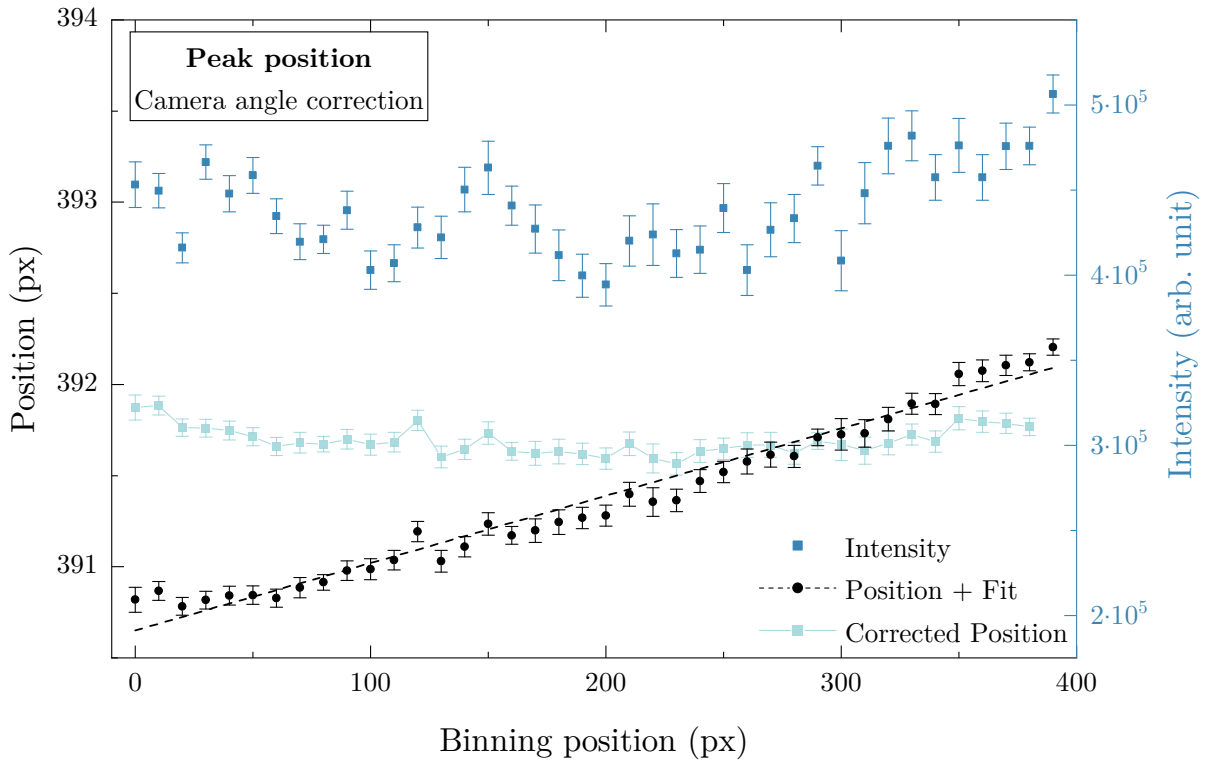

Figure C.4: Evolution of the measured and corrected spectral peak position along the CCD vertical binning position.

For completeness the measurement should also be shifted in the vertical axis, although this results in a position change less than 0.05 mm for angles <0.3° at the edges of the images (calculated from the spatial resolution in C.4), this is negligible for the purpose of this work and is therefore omitted.

C.3 Linear dispersion

One of the most important properties of a spectrograph is dispersion which describes how much a spectral interval is spread, in other words the ability to split the light. Although the angular dispersion is often used in theory to describe this phenomena, most detectors have a flat detection plate. Therefore, it is more useful to describe the separation of light by position instead of angle. This linear dispersion is expressed in nm/mm or when using a camera it is even more convenient to express it in nm/px. To determine the linear dispersion of the spectrograph, the pixel position of known spectral lines were tracked while the spectrometer changed its central wavelength focus position setting. This line displacement is shown in figure C.5, the linear dispersion is the inverse of the slope of this line displacement. Because the linear dispersion changes with the wavelength and for higher orders of the spectrum, this value is only valid around the center wavelength of the

measurement. In table C.1 various linear dispersion values are listed with 95% confidence interval for the first spectral order.

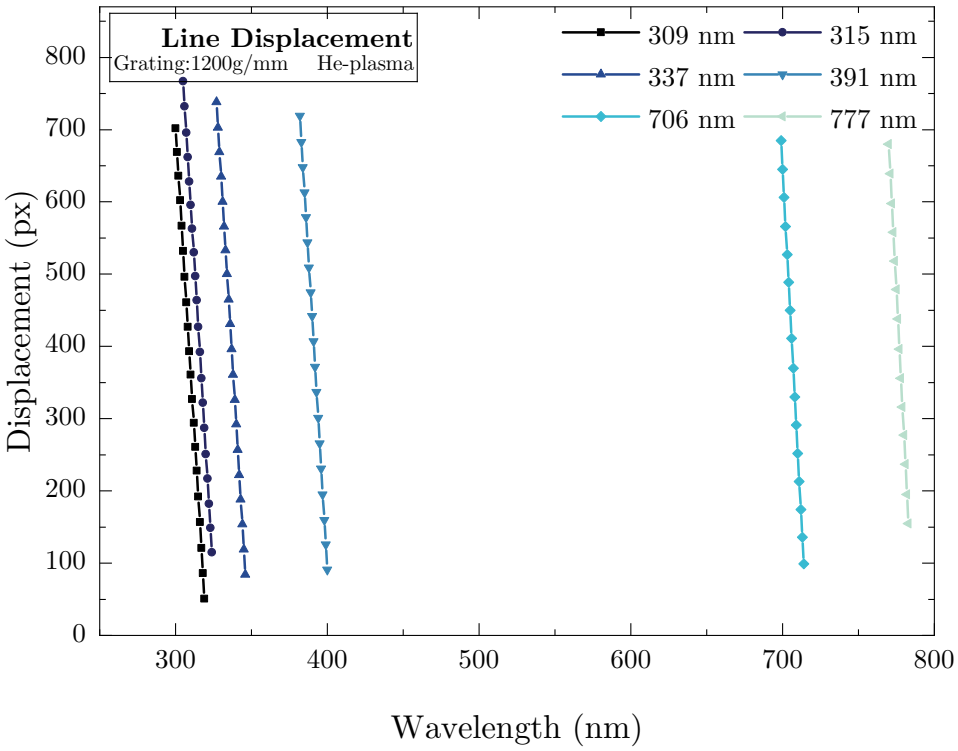

Figure C.5: The displacement of the spectral peak position on the CCD by changing the center focus wavelength.

Table C.1: First order linear dispersion

Wavelength (nm)	**Linear Dispersion (px/nm)**	
	150 (g/mm)	1200 (g/mm)
253.65*	4.11 ± 0.03	33.8 ± 0.1
309		34.18 ± 0.07
315		34.31 ± 0.09
337		34.39 ± 0.04
365.02*		34.5 ± 0.1
391		34.83 ± 0.05
404.66*		34.86 ± 0.06
435.83*	4.11 ± 0.01	35.68 ± 0.07
507.30*	4.09 ± 0.01	36.15 ± 0.06
546.08*		36.85 ± 0.08
576.96*		36.8 ± 0.1
640.23*		37.8 ± 0.1
659.90*		38.16 ± 0.08
692.95*		38.6 ± 0.2
706	4.14 ± 0.02	39.19 ± 0.06
777		40.32 ± 0.05

* Spectral lines from the IntelliCal Hg/Ne-Ar lamp.

C.4 Spatial resolution

To define the spatial position of the observed object in front of the spectrograph, the spatial resolution needs to be determined. This is been carried out with a collimated led lamp, type *M625L3-C1*, with an approximate nominal wavelength of 625 nm and bandwidth (FWHM) of 18 nm. With the 1200 grooves/mm grating, this light source will illuminate the entire CCD. Because of this some clear distinguished features can been seen on the image.

When moving the jet in z-direction, the shadow position from the anode and cathode due to blocking of the light can be well determined, see figure C.6. For this work a spatial resolution of 54.88 ± 0.05 px/mm is calculated from the slope of this shadow edges displacement in the vertical direction on the CCD.

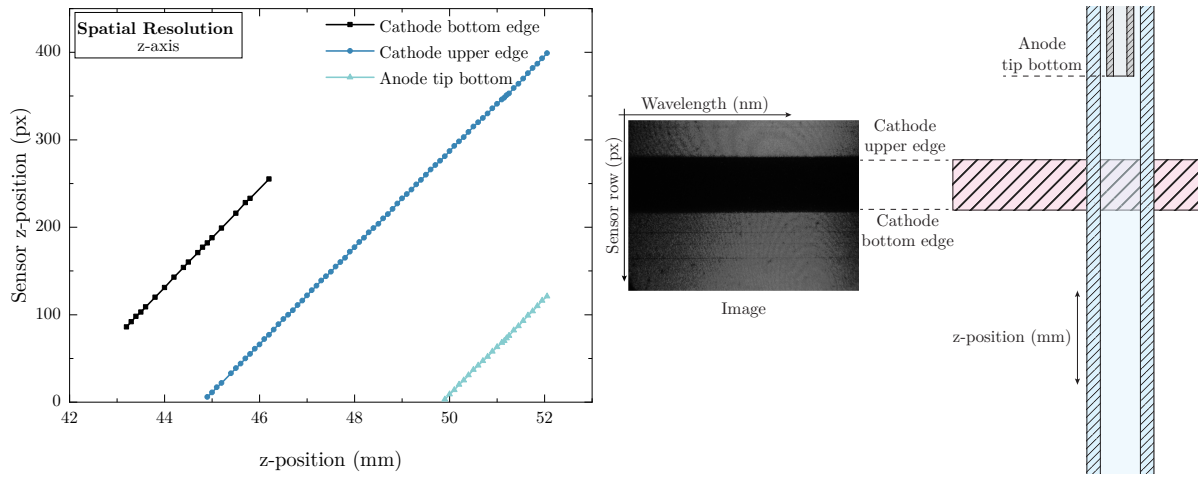

Figure C.6: Visual representation of the procedure to determine the spatial resolution.

C.5 Instrumental broadening

When recording spectra, the resulting spectral lines are broadened by the spectrograph. This so called instrumental broadening has a Gaussian profile line shape and varies with dispersion angle and depends on slit width. A low pressure calibration lamp (Hg/Ne-Ar)is used to determine the instrumental broadening for the spectrograph setup. In this work the measurements are performed with a slit width of 50 µm. In table C.2 the instrumental broadening is listed.

Table C.2: Instrumental Broadening - Grating 1200 [G/mm]

Slit width (µm)	**Broadening (nm)**
	435.83 nm
10	0.081 ± 0.002
20	0.086 ± 0.003
30	0.093 ± 0.002
40	0.097 ± 0.002
50	0.107 ± 0.002
60	0.115 ± 0.002
70	0.128 ± 0.002
80	0.140 ± 0.002
90	0.152 ± 0.002
100	0.166 ± 0.003

C.6 Spectral sensitivity

The spectrograph consist of many components, each with their own transmission, reflection and sensitivity dependency on wavelength. The spectral response of the setup is mainly determined on the blazing of the grating and on the photo cathodes sensitivity in the camera, which are the limiting components.

To get insight in the spectral response of the setup a calibration lamp (LS-1-Cal tungsten halogen light source) is placed in the focus position of the lenses, with entrance slit width 50 µm, trigger on 30 kHz, shutter time of 1 µs, integration time of 8 s, 5 frames per exposure and with MCP gain of 825 V. The direct lighting is done with and without cut-off filter, filters are used to cut out higher spectral orders. When the lamp was connected by optic fiber no filter was used.

From the resulting intensity in figure C.7 it is clear that the spectrograph is the most sensitive around 550 nm, and for measuring in the outer regions the integration time and/or MCP gain needs to be increased. Also the effect of the cut-off filters has its influence on the intensity on the whole spectral range.

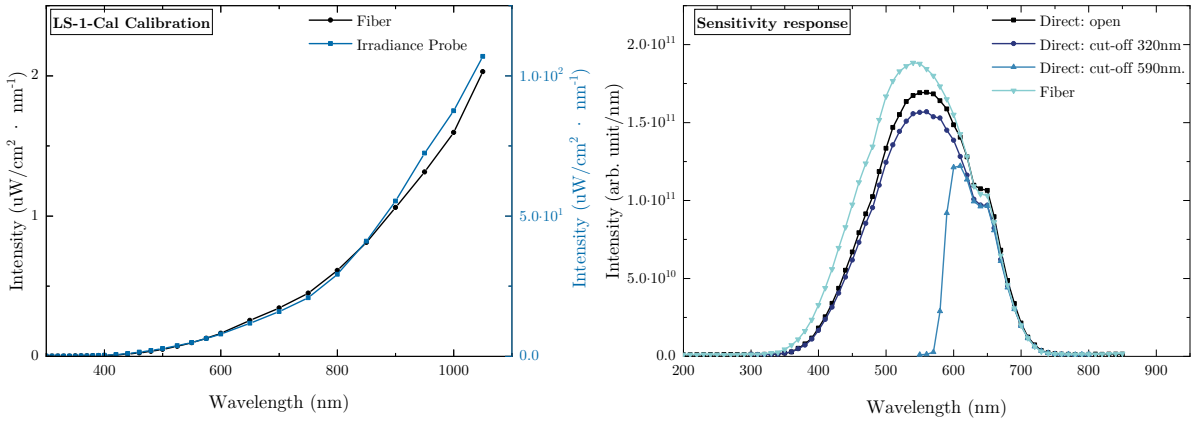

(a) **(b)**

Figure C.7: Spectral sensitivity response of the spectrograph setup.

Appendix D

Implemented software

Two programs are designed during this project, one to semi-automate the setup and the other to process the acquired measurement images. A short description on the GUI and the code structure is given in the following sections for each application.

D.1 Run Experiments

The Run Experiments application is a tool to automate the measurement acquisition, by fully controlling the spectrograph setup. The program can automatically measure in a range of wavelengths and delay times, and when operating in trigger mode it will automatically clear the camera buffer when settings are changed. Furthermore for each measuring series a textual log file as well as a settings file will be created of the experiment settings. This settings file can be used to repeat the same experiment at another time.

D.1.1 GUI documentation

Figure D.1 illustrates the interface of this application. The window is divided in several parts, in which experiment settings can be set to acquire and save a measurement. In the top part, the camera, spectrometer and experiment type is selected and thereafter the the directory location, experiment name and version control can be set. In the bottom right there is a status window which displays the message of the latest action. For longer actions, *i.e.* experiment check or measurement series, a progress bar is displayed on top of the GUI with the possibility to cancel the action prematurely.

The main part consists of the experiment settings; in the camera section the experiment time management (delay time, shutter time and integration), frames per exposure and the MCP gain can be set. In the spectrometer the desired grating and the central wavelength, or wavelength series, can be chosen. Here the choice can be made between light input via the optic fibre or via direct exposure, in the later case the entrance slit width and cut-off filter can be set. In the Plasma Jet Ac section the observed plasma parameters are stored, such as the applied voltage, gas flow and type. The final input is a Comments field, in here observations can be noted which will be

stored in the log files.

At the bottom center of the window you can choose from a few actions. A previous experiment settings file can be loaded. The camera and spectrometer can be prepared with the desired settings without performing a measurement. The current experiment can be checked, to prevent overwriting of earlier acquired measurements with the same settings. Finally a measurement can be acquired by performing a single/background measurement (at each wavelength executed at the start delay time) or performing the whole sequence (at each wavelength every delay time).

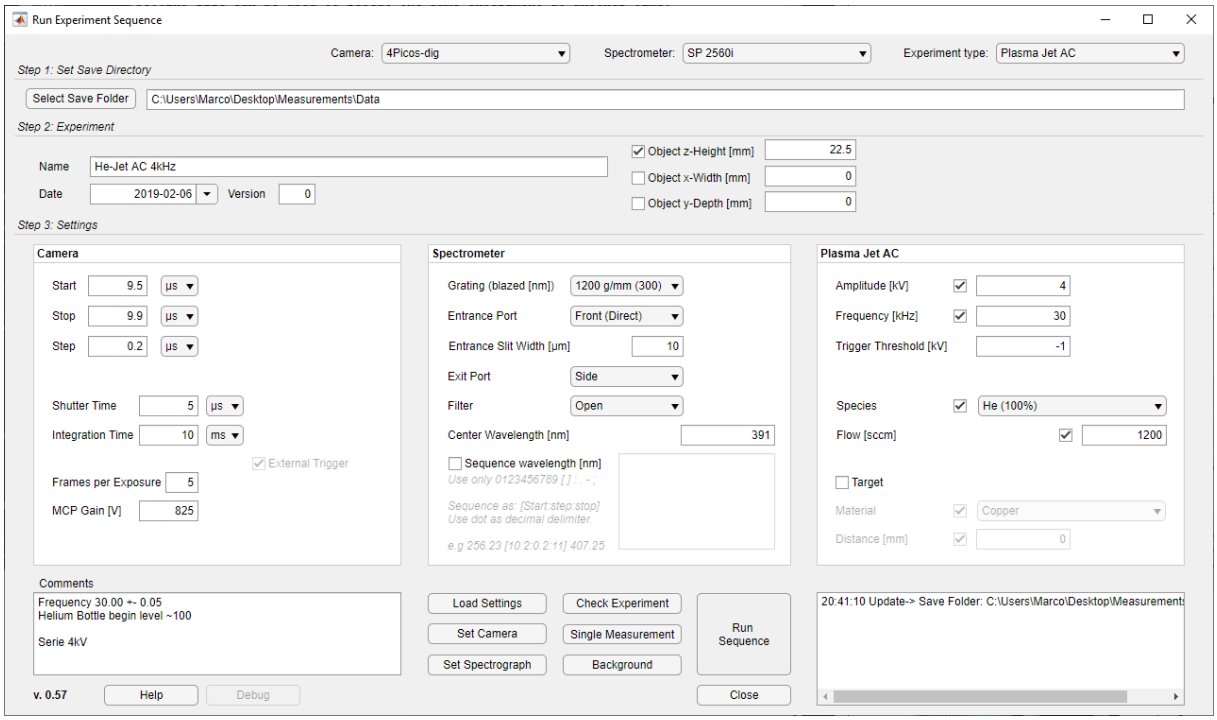

Figure D.1: The graphic user interface of the Run Experiments application.

The saved file names are constructed from a generic body which include settings such as wavelength, position, version and plasma parameters. A part that will be parsed in front of this body, describes the file type, *e.g.* '_Log_' or '_Settings_'. To distinguish each measurement a last part will parse to the name which includes the delay time. You can choose to exclude settings from the file name through the check boxes. An example of a generated file is: `\Measurements\Data\2019-02-06 He-Jet AC 4kHz\391nm_He100_1200sccm_4kV_30kHz_oz22.5mm_v0_T[9.700][us].tif`.

D.1.2 Code implementation

The Run Experiment application is developed in MatLab which operates parallel to the 4Spec and Lightfield software, which are respectively the controlling software of the camera and spectrometer. To facilitate the communication between the application and the hardware controlling software, two "interpreters" are written, SCO_Interpreter.exe

and LightField_Interpreter.exe. These translator files have all the options and settings which can be executed with the camera and spectrometer declared as functions. Which provides the possibility to call these actions in the Run Experiments application, see for an example D.1.

File	RunExperiments.exe
Main source file	Run_Sequence.mlapp
Language	Matlab R2018b
Latest version	v0.57
Last edit	24-04-2019
Lines of code	2503 lines

NOTE: This script sets the shutter time and the gain of the intensifier, always check these values to prevent damage to the camera by overexposure.

- RunExperiments.exe
  - SCO_Interpreter.exe
    - 4Spec software v.2.29.0.5
      - **iCCD Camera: *4Picos-dig***
  - LightField_Interpreter.exe
    - LightField software
      - **Spectrometer: *Acton SP2560i***
        - Slit width front entrance
        - Cut-off filter front entrance

```
% Set camera gain.
Do_Cam(app,['MCPGain ' num2str(app.mcp_GainField.Value)]);
```

Listing D.1: Implementation example in the Run Experiment application to control the MCP gain value by the MCPGain(gain_value) function in SCO_Interpreter.

Interpreter files: SCO_Interpreter & LightField Interpreter

The interpreters are programmed in AutoHotKey language which is a basic-like syntax. For correct working the interpreters' files needs to be located in the application directory. See table D.1 and table D.2 for a list of the functions that are implemented for the LightField and the 4Spec software.

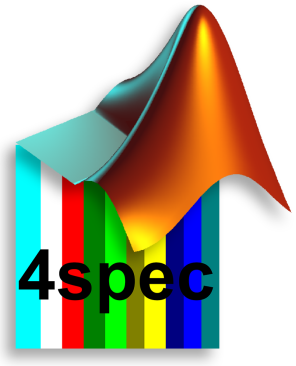

File	SCO_Interpreter.exe
Main source file	SCO_Interpreter.ahk
Language	AutoHotkey
Latest version	v0.9
Last edit	05-09-2018
Lines of code	1054 lines

NOTE: This program only works for a SCO camera which is connected by USB interface.

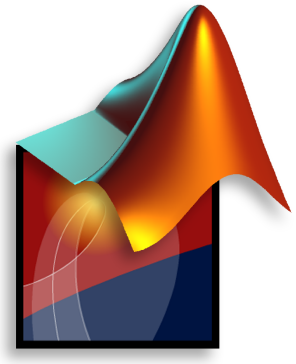

File	LightField_Interpreter.exe
Main source file	LightField_Interpreter.ahk
Language	AutoHotkey
Latest version	v0.7
Last edit	24-04-2019
Lines of code	369 lines

Table D.1: LightField-Interpreter: Command and Function index.

```
RunLightField()
OpenAllExpander()
CloseLightField()
CloseLightFieldExcept(windowName)
```

```
Grating(Option)
CenterWavelength(Wavelength)
EntrancePort(Port)
EntranceSlitWidth(SlitWidth)
ExitPort(Port,Entrance)
FilterWheel(Filter, Entrance)
```

Table D.2: SCO_Interpreter: Command and Function index sorted by menu.

`Run4spec()`
`Close4spec()`

File Menu
`Open()`
`SaveAs32(file_name)`
`SaveAs16(file_name)`
`ExportTiff16(file_name)`
`ExportTiff8(file_name)`
`ExportRaw32(file_name)`
`ExportRaw16(file_name)`
`ExportRaw8(file_name)`
`ExportBMP(file_name)`

Set Menu
`SetBackground()`
`SetFlatField()`

Execute Menu
`RunScanSequence()`
`AcquireOneExposure()`
`AcquireOneBackground()`
`RepeatScanCurves()`
`RepeatScanImage()`
`DisplayActiveImage()`
`DisplayBackgroundImage()`
`DisplayFlatFieldImage()`

Window Menu - Control
`Delay(delay_amount,order_s)`
`ShutterTime(time,order_s)`
`MCPGain(gain_value)`
`SetMode(option)`
`DigitzerMode(bit_value)`
`GateCtrl(option)`
`TriggerMode(option, input_value)`
`TrigSource(option)`
`IntegrationTime(time, order_s)`
`Detector(option)`
`CCDGain(gain_value)`
`StartOption(option)`
`SendIt()`
`ExitCamera()`

Process Menu
`SubtractBackground()`
`FlipImgHorizontal()`
`FlipImgVertical()`

Setup - Scan Sequence
`FramesPerExposure(number_of_frames)`
`ExposuresPerScan(number_of_exposures)`
`NumbersOfScans(number_of_scans)`
`UseInternalTimer(x, y)`
`SnapOnExternalEvent(x)`

D.2 Image Processor

The Image Processor application is a data processor tool, designed to serve two purposes. First to translate the raw measurement images to useful data, *i.e.* wavelength & intensity data at spacial position. For this post processing task, it can apply background measurement subtraction, conversion of the pixel dimensions to wavelength and spatial position and correction for the camera orientation. The binded data at a desired position of the intensity at a certain wavelength can be fitted for different types and multiple peaks. The data and the fits can be exported.

Secondly the possibility to review the processed data including peak profiles quickly without the need to open the original files. The fit confidence band as well as the deconvolution of a multiple peak profile can be inspected after which the fit function values, at desired position, or function coefficients, can be exported to other data analysis and graphing software, *e.g.* Origin Pro.

D.2.1 GUI documentation

The interface of the Image Processer is shown in figure D.2. The GUI is divided in several areas, in the bottom right corner there is a status window and some basic tasks are in the top menu. Here the images which you want to process can be selected, data can be exported and extra tools can be accessed such as the Data Export Processor. The working process is as follows; in the bottom left a measurement can be selected and the corresponding diagnostic settings such as the linear dispersion, center wavelength and position of the object need to be set. Above these settings you can zoom into specific parts of the experiment images, with the range and position sliders, which can be locked such as to apply for all images. A selection in the spatial direction is also applied here by adjusting the pixel binning. The displayed image is then plotted on the right, according to the plot settings. Here you can choose to scatter all the data points or to sum over the binning range and to apply the wavelength position correction (depending on the camera angle).

This corrected and position binned wavelength & intensity data can already be exported to a .txt or matlab file. The next step is to fit peak profiles on the data. There are several profiles to choose from. The profiles can differ in overall shape, such as a Gaussian, Lorentzian, Voigt and PseudoVoigt profiles, or in the fit parameters as peak area or amplitude. The maximum number of peaks to be fit on the data can be set, as well as the Gaussian and Lorentzian width coefficients contributions to the peak can be kept the same for each peak. If coefficients limits are bounded and one or more of the estimates are at their bounds, those estimates are regarded as fixed and do not have confidence bounds. Once a fit is executed you can go to the next binning position and repeat the fit for this spatial position or select a new measurement.

Each set of binned data and fit will be stored in the export memory, from here it can be exported to a file or directly loaded for reviewing in the Export Data Processor tool. This tool can be loaded from the menu (`\Tools\ExportData Processor`). Figure D.3 shows the interface of this application. In the bottom left you can load previously

processed data or load the current export memory. The data and associated fit object for each binning position will be displayed in the left top table. From here the data points, fit profile, confidence band and deconvolution can be set to be visualized in the graph. Using the check-boxes in the table settings, you can select which values, fit coefficients and confidence intervals you want to add to the export table. Also the confidence level and the table order can be adjusted here. Finally by pressing "Add Data" in the bottom right, all the values of interest will be added to a table which can be extended with the next processed data file or directly copied to clipboard.

In both the Image Processor window and in the Export Data Processor window are control buttons to hold or clear parts of tables and graphs for comparison.

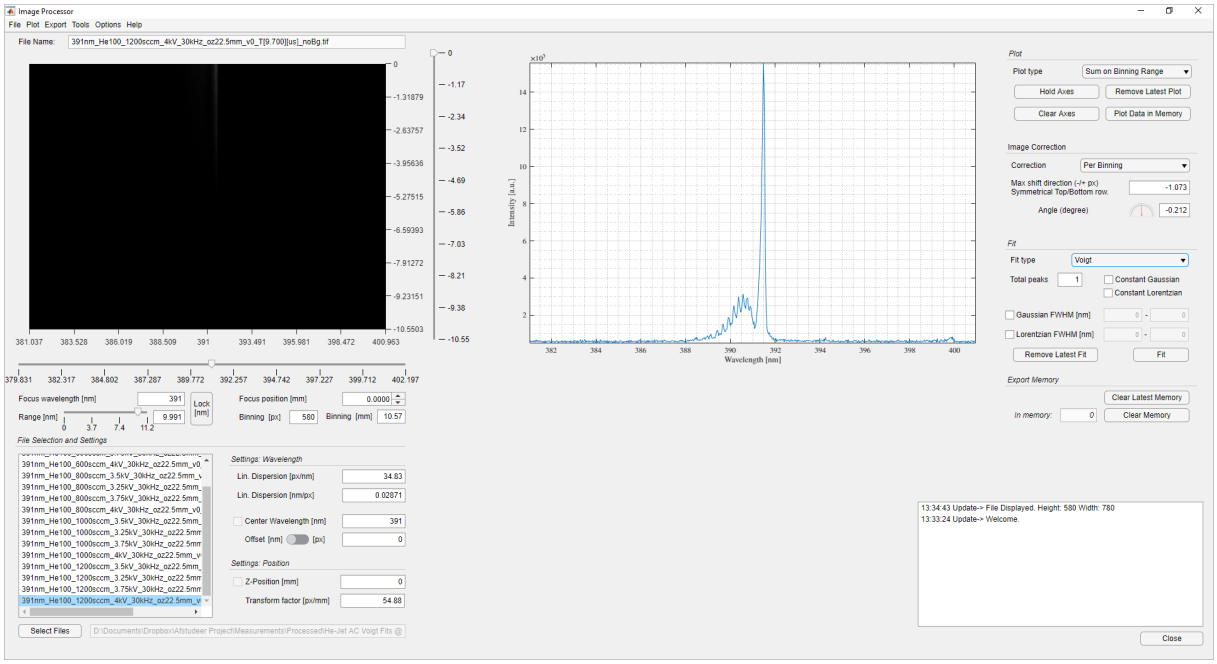

Figure D.2: The main interface of the Image Processor application.

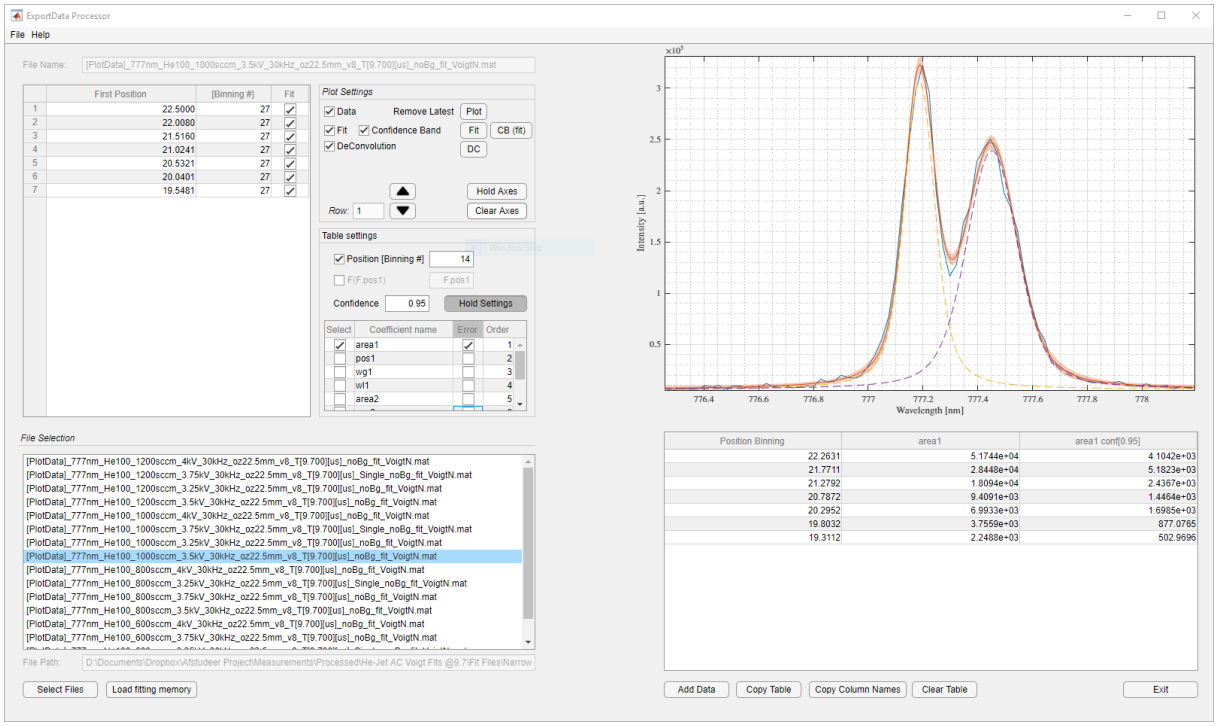

Figure D.3: Interface of Export Data Processor, which is part of the Image processor.

D.2.2 Code implementation

The Image Processor is written in MatLab, and is structured in two main source files and the individual curve fitting profiles. The Image Processor can perform the main task; converting and fitting of the raw measurement images for which it uses the programmed curve profiles. While the Export Data Processor is written to review the processed fits.

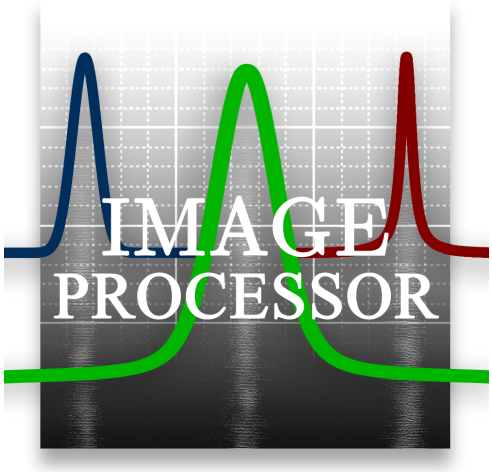

File	ImageProcessor.exe
Main source file 1	ImageProcessor.mlapp
Language	Matlab R2018b
Latest version	v1.41
Last edit	17-10-2019
Lines of code	2204 lines
Main source file 2	ExportDataProcessor.mlapp
Language	Matlab R2018b
Latest version	v0.09
Last edit	20-10-2019
Lines of code	1357 lines

ImageProcessor
- Export Data Processor
- Curve fitting
  - Basic profiles: Gaussian, Lorentzian, Voigt, Pseudo-Voigt
- Subtract background
- Export: Plot, Wavelength & Intensity, Memory Data

There are various fit types programmed for the Image processor to analyse the data. These fit types prepare and analyse the data to guess the fitting coefficients and set the fitting options such as the tolerance and iteration steps. The most important fit types are listed here and the derivation for each peak profile function can be found in the next chapter. For a multiple peak fit on the data, a linear combination of the fit profile type is generated.

- Gaussian Area (E.3)
- Lorentzian Area (E.6)
- Voigt (E.8)
- PseudoVoigt (E.9)

In the fit types the following fit coefficients are used: $area$ = area under the curve, pos = center peak position, wg = Gaussian FWHM and wl = Lorentzian FWHM. The following code snippets are examples of the basic fit profile functions.

```
function G = Gaussian1_noOffset_v1(x,area,pos,wg)
%% Gaussian1_v1 is a Gaussian profile with 1 peak.

    G = area/(wg*sqrt(pi/(4*log(2)))) * exp(-4*log(2)*(x-pos).^2./wg
        .^2);
end
```

Listing D.2: Fit type: Gaussian peak function.

```
function L = Lorentzian1_noOffset_v1(x,area,pos,wl)
%% Lorentzian1_v1 is a lorentzian profile with 1 peak.

    L = 2*area/pi * wl./(4*(x-pos).^2+wl.^2);
end
```

Listing D.3: Fit type: Lorentzian peak function.

```
function Vp = Voigt1_noOffset_v1(x,area,pos,wg,wl)
%% Voigt1_v1 is a voigt profile with 1 peak.

% The Voigt profile is a convolution of a Gaussian function and a
    Lorentzian function, expressed in the line broadening integral.

    f=(area.*2.*log(2).*wl)./(pi.^1.5.*wg.^2);
    int= @(t) exp(-t.^2)./((sqrt(log(2)).*wl./wg).^2+(sqrt(4*log(2))
        .*(x-pos)./wg-t).^2);

    Vp=f.*integral(int,-Inf,Inf,'ArrayValued',1);
end
```

Listing D.4: Fit type function: Voigt peak function, convolution of a Gaussian and a Lorentzian peak function.

```
function Vp = PseudoVoigtTCH1_noOffset_v1(x,area,pos,wg,wl)
%% PseudoVoigtTCH1_v1 is a profile with 1 peak.

% The Pseudo-Voigt function is an approximation for the Voigt
    function, which is a convolution of Gaussian and Lorentzian
    function.
% Instead of convoluting those two functions, the Pseudo-Voigt
    function is defined as the sum of a Gaussian peak G(x) and a
    Lorentzian peak L(x), weighted by a fourth parameter \eta (with
    values between 0 and 1).

% P. Thompson, D.E. Cox, J.B. Hastings, J. Appl. Cryst. 1987, 20,
    79.)

% Total FWHM composed from FWHM_wg and FWHM_wl.
    TotFWHM = (wg.^5 + 2.69269*(wg.^4.*wl) + 2.42843*(wg.^3.*wl.^2) +
        4.47163*(wg.^2*wl.^3) + 0.07842*(wg.*wl.^4) + wl.^5)^(1/5);
% Eta: Lorentzian fraction i.e. mixing parameter.
    eta = 1.36603*(wl/TotFWHM) - 0.47719*(wl/TotFWHM).^2 + 0.11116*(
        wl/TotFWHM).^3;

% Gaussian and lorentzian expressed in TotFWHM.
    G = (sqrt(4*log(2))/(sqrt(pi).*TotFWHM)).*exp(-(4*log(2)./TotFWHM
        .^2)*(x-pos).^2);
    L =(2/pi).*(TotFWHM./((4*(x-pos).^2)+TotFWHM.^2));

    Vp = area*(eta*L + (1-eta)*G);
end
```

Listing D.5: Fit type function: pseudo-Voigt defined by [55].

Appendix E

Derivation of the fit functions

In this chapter the basic fit functions for peak profiles are defined. Due to some confusing use of the scaling parameter of the functions in literature, varying from *Full Width Half Maximum*, *Half Width Half Maximum*, *Half-Width*, *Width*, *standard deviation* etc., the following expressions for the fit functions are derived from the standard-form in [56] with the scale parameter expressed in FWHM.

Gaussian peak function

Start from the following standard form of the Gaussian function, with x_c as location parameter and c as scale parameter.

$$f(x) = a \cdot \mathrm{e}^{-\frac{(x-x_c)^2}{2c^2}} \tag{E.1}$$

To get this function expressed in the FWHM scale parameter $w_G = \left(x_G^+ - x_G^-\right)$, we need to solve for c in terms of w_G:

$$\begin{aligned} f(x_G) &= f(x_c)/2 \\ a \cdot \mathrm{e}^{-(x_G-x_c)^2/(2c^2)} &= \frac{1}{2} a \cdot \mathrm{e}^{-((x_c-x_c)^2)/(2c^2)} \\ \mathrm{e}^{-(x_G-x_c)^2/(2c^2)} &= 2^{-1} \\ (x_G - x_c)^2/(2c^2) &= \ln 2 \\ (x_G - x_c) &= \pm\sqrt{2\ln 2}\, c \end{aligned}$$

$$\left.\begin{aligned} x_G^+ &= \sqrt{2\ln 2}\, c + x_c \\ x_G^- &= -\sqrt{2\ln 2}\, c + x_c \end{aligned}\right\} \quad w_G = x_G^+ - x_G^- = 2\sqrt{2\ln 2}\, c$$

$$\Rightarrow c = \frac{w_G}{2\sqrt{2\ln 2}}.$$

Insert this expression for the scaling parameter in (E.1).

$$f(x) = a \cdot \mathrm{e}^{-4\ln 2(x-x_c)^2/(w_G^2)} \tag{E.2}$$

To determine a we normalize (E.2). With substitution of $q = 4\ln 2/w_G^2$ and solving the integral (by polar coordinates[1]).

$$\int_{-\infty}^{\infty} a \cdot \mathrm{e}^{-4\ln 2(x-x_c)^2/(w_G^2)}\,\mathrm{d}x = 1$$

follows

$$a = \frac{1}{w_G\sqrt{\frac{\pi}{4\ln 2}}}$$

Inserting a in (E.2) and multiply with the A_{rea} under the curve results in:

$$G(x) = \frac{A_{rea}}{w_G\sqrt{\frac{\pi}{4\ln 2}}} e^{-\frac{4\ln(2)(x-x_c)^2}{w_G^2}} \tag{E.3}$$

Lorentzian

Start from the following standard form of the Gauchy-Lorentz distribution function, with x_c as location parameter and s as scale parameter.

$$f(x) = \frac{a}{s\pi\left(1+\left(\frac{x-x_c}{s}\right)^2\right)} = \frac{a}{\pi}\frac{s}{(x-x_c)^2+s^2} \tag{E.4}$$

To get this function expressed in the FWHM scale parameter $w_L = \left(x_L^+ - x_L^-\right)$, we need to solve for s in terms of w_L:

$$\begin{aligned}
f(x_L) &= f(x_c)/2 \\
\frac{s}{\pi}\frac{1}{(x_L-x_c)^2+s^2} &= \frac{s}{2\pi}\frac{1}{(x_c-x_c)^2+s^2} \\
\frac{1}{(x_L-x_c)^2+s^2} &= \frac{1}{2s^2} \\
(x_L-x_c)^2 &= s^2 \\
(x_L-x_c) &= \pm s
\end{aligned}$$

$$\left.\begin{aligned} x_L^+ &= s + x_c \\ x_L^- &= -s + x_c \end{aligned}\right\} \quad w_L = x_L^+ - x_L^- = 2s$$
$$\Rightarrow s = \frac{w_L}{2}.$$

[1] $\left(\int_{-\infty}^{\infty}\mathrm{e}^{-qx^2}\,\mathrm{d}x\right)^2 = \int_{-\infty}^{\infty}\int_{-\infty}^{\infty}\mathrm{e}^{-q(x^2+y^2)}\,\mathrm{d}x\,\mathrm{d}y = \int_0^{2\pi}\int_0^{\infty}\mathrm{e}^{-qr^2}\,r\,\mathrm{d}r\,\mathrm{d}\theta = \frac{\pi}{q}$

Insert this expression for the scaling parameter in (E.4).

$$f(x) = \frac{a}{\pi} \frac{\left(\frac{w_L}{2}\right)}{(x - x_c)^2 + \left(\frac{w_L}{2}\right)^2} = \frac{2a}{\pi} \frac{w_L}{4(x - x_c)^2 + w_L^2} \tag{E.5}$$

To determine a we normalize (E.5).

$$\int_{-\infty}^{\infty} \frac{2a}{\pi} \frac{w_L}{4(x - x_c)^2 + w_L^2} \, \mathrm{d}x = 1$$

For convenience we set $x_c = 0$ and substitute $x = w_L/(2u)$.

$$\frac{2a}{\pi} \int_{-\infty}^{\infty} \frac{w_L}{w_L^2 u^2 + w_L^2} \frac{w_L}{2} \, \mathrm{d}u = 1$$

$$\frac{a}{\pi} \int_{-\infty}^{\infty} \frac{1}{u^2 + 1} \, \mathrm{d}u = 1$$

$$\frac{a}{\pi} \arctan u \Big|_{-\infty}^{\infty} = \frac{a}{\pi} \left[\frac{\pi}{2} - \left(-\frac{\pi}{2} \right) \right] = a = 1$$

Inserting a in (E.5) and multiply with the A_{rea} under the curve results in:

$$L(x) = \frac{2 \cdot A_{rea}}{\pi} \frac{w_L}{4(x - x_c)^2 + w_L^2} \tag{E.6}$$

Voigt

An intensity distribution broadened by two independent effects is given by a so called Voigt function [57], defined as the convolution of two broadening function.

$$h(x) = (f_1 * f_2)(x) = \int_{-\infty}^{\infty} f_1(\delta) f_2(x - \delta) \, \mathrm{d}\delta$$

With the contribution from a Lorentzian shape, *e.g.* natural line broadening and from a Gaussian profile, *e.g.* Doppler effect the resulting line shape function is (E.7). The order of convolution has no influence [58], and the total area under the curve is defined as A.

$$V(x) = \int_{-\infty}^{\infty} G(\delta) L(x - \delta) \, \mathrm{d}\delta \tag{E.7}$$

$$\text{where} \quad G(\delta) = \sqrt{\frac{4 \ln 2}{\pi}} \frac{1}{w_G} \mathrm{e}^{-\frac{4 \ln 2}{w_G^2} \delta^2}, \quad L(x - \delta) = \frac{2A}{\pi} \frac{w_L}{4(x - x_c - \delta)^2 + w_L^2}$$

Next we write this Voigt function in an appropriate form, expressed in the line broadening function integral [59].

$$
\begin{aligned}
V(x) &= \int_{-\infty}^{\infty} \sqrt{\frac{4\ln 2}{\pi}} \frac{1}{w_G} \mathrm{e}^{-\frac{4\ln 2}{w_G^2}\delta^2} \cdot \frac{2A}{\pi} \frac{w_L}{4(x-x_c-\delta)^2 + w_L^2} \,\mathrm{d}\delta \\
&= A \cdot \frac{4\sqrt{\ln 2}}{\pi^{3/2}} \frac{w_L}{w_G} \int_{-\infty}^{\infty} \frac{\mathrm{e}^{-\frac{4\ln 2}{w_G^2}\delta^2}}{4(x-x_c-\delta)^2 + w_L^2} \,\mathrm{d}\delta \\
&= A \cdot \frac{4\sqrt{\ln 2}}{\pi^{3/2}} \frac{w_L}{w_G} \int_{-\infty}^{\infty} \frac{\mathrm{e}^{-\left(\frac{2\sqrt{\ln 2}\,\delta}{w_G}\right)^2}}{4(x-x_c-\delta)^2 + w_L^2} \,\mathrm{d}\delta
\end{aligned}
$$

Now we substitute $\xi = \frac{2\sqrt{ln2}}{w_G}\delta$ into the equation.

$$
\begin{aligned}
V(x) &= A \cdot \frac{4\sqrt{\ln 2}}{\pi^{3/2}} \frac{w_L}{w_G} \int_{-\infty}^{\infty} \frac{\mathrm{e}^{-\xi^2}}{4\left(x - x_c - \frac{\xi w_G}{2\sqrt{ln2}}\right)^2 + w_L^2} \frac{w_G}{2\sqrt{\ln 2}} \,\mathrm{d}\xi \\
&= \frac{2A}{\pi_{3/2}} w_L \int_{-\infty}^{\infty} \frac{\mathrm{e}^{-\xi^2}}{4\left(\frac{(x-x_c)2\sqrt{\ln 2} - \xi w_G}{2\sqrt{ln2}}\right)^2 + w_L^2} \,\mathrm{d}\xi \\
&= \frac{2A\ln 2}{\pi_{3/2}} w_L \int_{-\infty}^{\infty} \frac{\mathrm{e}^{-\xi^2}}{\left((x-x_c)\sqrt{4\ln 2} - \xi w_G\right)^2 + \left(\sqrt{\ln 2}\, w_L\right)^2} \,\mathrm{d}\xi \\
&= \frac{2A\ln 2}{\pi_{3/2}} w_L \int_{-\infty}^{\infty} \frac{\mathrm{e}^{-\xi^2}}{w_G^2\left(\left(\frac{x-x_c}{w_G}\sqrt{4\ln 2} - \xi\right)^2 + \left(\sqrt{\ln 2}\frac{w_L}{w_G}\right)^2\right)} \,\mathrm{d}\xi
\end{aligned}
$$

$$
V(x) = A\frac{2\ln 2}{\pi^{3/2}} \frac{w_L}{w_G^2} \int_{-\infty}^{\infty} \frac{e^{-\xi^2}}{\left(\sqrt{\ln 2}\frac{w_L}{w_G}\right)^2 + \left(\sqrt{4\ln 2}\frac{(x-x_c)}{w_G} - \xi\right)^2} \,\mathrm{d}\xi \tag{E.8}
$$

PseudoVoigt

A less computer capacity demanding approximation of the Voigt shape is the PseudoVoigt. There are a variety of Voigt approximations constructed as the sum or product of Gaussian and Lorentzian shapes. The following PseudoVoigtTCH from [55] is implemented. Note that total combined width w_{tot} is used in the Lorentzian and Gaussian contribution, not the separate Gaussian and Lorentzian widths.

$$
V_p(x) = \eta \cdot L(x, w_{tot}) + (1-\eta)G(x, w_{tot})
$$

with the mixing ratio parameter η and total width w_{tot} defined as:

$$
\eta = 1.36603(w_L/w_{tot}) - 0.47719(w_L/w_{tot})^2 + 0.11116(w_L/w_{tot})^3
$$

$$
w_{tot} = \left(w_G^5 + 2.69269 w_G^4 w_L + 2.42843 w_G^3 w_L^2 + 4.47163 w_G^2 w_L^3 + 0.07842 w_G w_L^4 + w_L^5\right)^{(1/5)}
$$

$$V_p(x) = A\left(\eta\frac{2}{\pi}\frac{w_{tot}}{4(x-x_c)^2+w_{tot}^2} + (1-\eta)\frac{\sqrt{4\ln 2}}{\sqrt{\pi}w_{tot}}\,\mathrm{e}^{-\frac{4\ln 2}{w_{tot}^2}(x-x_c)^2}\right) \tag{E.9}$$

An advantage of the pseudo-Voigt is that it quickly calculates a good estimation of the Voigt profile and the area under the curve (with an accuracy of 10^{-3}); however, the separate broadening contributions are less easily to determined from it [60, 61].